

PhD Thesis

Ultrafast laser sources and frequency conversion at high repetition rates

Presented by

Marin Hamrouni

A dissertation submitted to:

University of Neuchâtel
Faculty of science

PhD jury:

Prof. Thomas Südmeyer
Dr. Valentin Wittwer
Prof. Martin M. Fejer
Prof. Philippe Grelu

Director
Examiner
Examiner
Examiner

Neuchâtel, February 19, 2024

IMPRIMATUR POUR THESE DE DOCTORAT

La Faculté des sciences de l'Université de Neuchâtel autorise
l'impression de la présente thèse soutenue par

Monsieur Marin HAMROUNI

Titre :

**“Ultrafast laser sources and frequency
conversion at high repetition rates”**

sur le rapport des membres du jury composé comme suit :

- Prof. Thomas Südmeyer, directeur de thèse, Université de Neuchâtel, Suisse
- Dr Valentin Wittwer, Université de Neuchâtel, Suisse
- Prof. Martin M. Fejer, Stanford University, USA
- Prof. Philippe Grelu, Université de Bourgogne, France

Neuchâtel, le 8 avril 2024

Le Doyen, Prof. R. Bshary



Keywords - Mots clés

Keywords

Mode-locked laser, Optical frequency comb, Ultrafast optics, Nonlinear optics, Thin-film lithium niobate, Mid-infrared generation, Terahertz generation, Supercontinuum generation

Mots clés

Laser à verrouillage de mode, Peigne de fréquence optique, Optique ultra-rapide, Optique non linéaire, Niobate de lithium en couche mince, Génération de lumière infrarouge, Rayonnement térahertz, Génération de supercontinuum

Abstract

Mode-locked laser sources have become a cornerstone technology for numerous applications and led to the development of groundbreaking optical tools and systems. In the optical frequency domain, mode-locked lasers feature spectra composed of a set of discrete lines that are equally spaced. This spectral structure gave the name to a new tool called optical frequency comb (OFC), spanning applications such as spectroscopy, astronomy, attoscience, telecommunications, and atomic clocks. The main important features of OFCs are the average power and spectral bandwidth, in addition to the repetition rate and the location of the comb-lines within the electromagnetic spectrum. While nearly all applications benefit from high average power and large spectral bandwidths, the most suitable repetition rates and spectral regions are truly application dependent. Mode-locked lasers generating near-infrared pulses with repetition rates spanning from megahertz to hundreds of megahertz are now mature. Nowadays, driven by application needs in spectroscopy and astronomy, many research projects focus on generating OFCs in the mid-infrared spectral region as well as increasing the repetition rates. Due to the lack of commercially available laser crystals featuring resonant transitions in the mid-infrared region, direct generation of OFCs above $3\ \mu\text{m}$ is technologically challenging. While the emergence of quantum cascade lasers paved a promising way for direct mid-infrared generation, the main approach for realizing broadband mid-infrared OFC sources remains nonlinear frequency conversion of near-infrared pulses delivered by mature mode-locked lasers. There, an important challenge is to deliver sufficient power to achieve efficient nonlinear conversion, especially at high repetition rates since the pulse energy and repetition frequency tend to play against each other. As a result, mid-infrared OFC sources based on gigahertz mode-locked lasers are rare and mostly limited to photonic laboratories.

Pursuing the objective of developing compact and cost-efficient OFC sources suitable for real-world applications, this thesis is structured into two main parts. The first chapter presents the development of powerful and broadband mode-locked laser oscillators based on Ytterbium (Yb) gain materials. It begins with the description of a Kerr-lens mode-locked Yb:CALGO oscillator operating at 1 GHz repetition frequency. The laser demonstrates the shortest pulse duration and highest average and peak power with respect to previous gigahertz-class oscillators based on Yb gain media. In a subsequent experiment, we perform the full stabilization of the laser, turning the source into a functional broadband OFC. Besides achieving low-noise performance, the stabilized source delivers peak power levels suitable for many applications, including nonlinear frequency

conversion. We close the first chapter by addressing the challenge of generating few-cycle pulses at high average power using Yb gain media. Here, we introduce a novel pumping scheme that overcomes the limitations due to the small frequency difference between the pump and laser photons. In particular, our technique enables efficient generation and broad spectral bandwidth at the same time. By implementing this approach in a soft-aperture Kerr-lens mode-locked laser oscillator, we obtain record-high optical-to-optical efficiency and high average power compared to previous Ytterbium-based sources operating in the few-cycle regime.

In the second part of this thesis, we investigate novel approaches for efficient frequency conversion of ultrafast lasers into the terahertz and mid-infrared spectral ranges. This part consists of three main sections. In the first section, we discuss the development of a compact and cost-efficient terahertz source based on driving the nonlinear process directly inside the cavity of a simple ultrafast bulk mode-locked laser. This way, the terahertz emitter benefits from leveraged power levels available inside the cavity, which reduces the requirement on the overall driving source compared to traditional approaches.

In the subsequent section, we demonstrate efficient and broadband mid-infrared generation based on parametric down-conversion inside thin-film lithium niobate waveguides. By exploiting the large nonlinearities and dispersion engineering offered by those nanophotonic devices, we revisit an approach to nonlinear down-conversion, namely gain-trapped optical parametric amplification. This technique relies on the interplay between nonlinear gain and group velocity mismatches, which under specific conditions results in the trapping of the down-converted pulses under the driving near-infrared pump. In the unsaturated regime, this approach enables exponential amplification of the mid-infrared pulses over distances exceeding conventional methods, which allows to reach saturation with a few picojoules of in-coupled pulse energy. After saturation, up to 50% of near-infrared pump photons are converted into the 3-4 μm band using only a few picojoules of pulse energy coupled inside the waveguide. Given the low energy requirements, this approach is promising for realizing efficient frequency conversion at multi-gigahertz repetition rates.

Lastly, we utilize dispersion-engineered thin-film lithium niobate devices to demonstrate broadband supercontinuum generation and carrier-envelope offset frequency detection at low input power. The approach uses dispersion engineering to match the group velocity of fundamental and second harmonic pulses centered around 2 and 1 μm respectively. In this case, an interplay between saturation and small phase-mismatch occurs over long interaction length, which leads to strong spectral broadenings. As a result, we generate a supercontinuum

ranging from the ultraviolet to mid-infrared ranges with only tens of picojoules of in-coupled fundamental energy. The resulting octave-spanning spectrum produces carrier-envelope offset frequency beatnotes that we directly detect at the waveguide output.

We believe that the combination of the laser sources presented in the first part with the frequency conversion techniques showcased in the second section will enable the realization of compact mid-infrared OFCs operating at high repetition rates. This leaves exciting prospects for follow up studies.

Résumé

Les sources laser à verrouillage de mode sont devenues une technologie clé pour de nombreuses applications et ont conduit au développement d'outils et systèmes optiques révolutionnaires. Les lasers à verrouillage de mode se caractérisent par un spectre optique composé d'un ensemble de lignes discrètes équidistantes en fréquence. Cette structure spectrale a donné son nom à un nouvel outil appelé peigne de fréquence optique, dont les applications sont nombreuses dans des domaines tels que la spectroscopie, l'astronomie, l'attoscience, les télécommunications et les horloges atomiques. Les principales caractéristiques de ces peignes sont la puissance moyenne, la largeur de bande spectrale, le taux de répétition ainsi que la position du peigne dans le spectre électromagnétique. De manière générale, la grande majorité des applications requièrent des puissances moyennes élevées ainsi que de larges bandes spectrales. Le taux de répétition propice et la région spectrale appropriée varient quant à eux en fonction de chaque application. Les lasers à verrouillage de mode générant des impulsions dans le proche infrarouge avec des taux de répétition allant de quelques mégahertz à des centaines de mégahertz sont désormais matures. Aujourd'hui, de nombreuses études se concentrent sur la génération de peigne optique dans le moyen infrarouge ainsi que sur l'accroissement du taux de répétition, répondant alors aux besoins de nombreuses applications en spectroscopie. En raison de la rareté de cristaux laser présentant des transitions résonnantes dans la région du moyen-infrarouge, la génération directe de peigne optique au-dessus de $3\ \mu\text{m}$ reste technologiquement difficile. Bien que les lasers à cascade quantique soient prometteurs à cet égard, l'une des principales approches utilisées pour développer des peignes optiques large bande dans le moyen-infrarouge consiste à transférer des impulsions courtes du proche-infrarouge via une conversion de fréquence non linéaire. La difficulté est alors de disposer de suffisamment de puissance de pompe dans le proche-infrarouge pour effectuer la conversion linéaire efficacement. En outre, puisque l'énergie de l'impulsion diminue lorsque le taux de répétition augmente, toute chose égale par ailleurs, la difficulté d'atteindre suffisamment de pic de puissance est d'autant plus élevée à haut taux de répétitions. En conséquence, les sources optiques gigahertz à large bande dans le moyen-infrarouge sont rares et leurs applications ne dépassent souvent pas le cadre du laboratoire.

Cette thèse est constituée en deux parties principales et s'intéresse au développement de sources à peigne de fréquence optique compactes et économiques, dans l'intérêt de rendre la technologie viable et disponible au-delà du cadre du laboratoire. Le premier chapitre se consacre au développement d'oscillateurs lasers délivrant des impulsions femtosecondes de puissance élevée dans le proche in-

frarouge. L'ensemble des sources lasers présentées dans ce chapitre repose sur l'utilisation de milieu à gain Yb:CALGO, dont les caractéristiques sont détaillées ultérieurement. La première section de ce chapitre détaille la conception d'un oscillateur laser à verrouillage de mode par lentille de Kerr opérant à une fréquence de répétition de 1 GHz. Le laser ainsi développé montre des performances remarquables. Entre autre, il produit la durée d'impulsion la plus courte ainsi que la puissance moyenne la plus élevée parmi les oscillateurs lasers Ytterbium opérant à des taux de répétition au-dessus du gigahertz. Dans un second temps, la stabilisation complète de ce laser est effectuée. La source stabilisée émet ainsi des peignes de fréquence optique bas bruit dont la puissance de crête élevée est particulièrement propice à la conversion de fréquence non-linéaire.

La dernière partie de ce chapitre présente une méthode permettant de générer efficacement des impulsions ultrabrèves à l'aide de lasers basés sur des milieux à gain à faible défaut quantique tels que les matériaux dopés à l'Ytterbium. Cette technique est basée sur une architecture de pompage laser colinéaire permettant la génération d'impulsions ultrabrèves dont le spectre s'étend au-delà de la longueur d'onde de pompe. Cette technique est appliquée sur un laser femtoseconde basé sur le milieu à gain Yb:CALGO. Le laser ainsi créé permet une efficacité optique et puissance moyenne record comparée aux sources Ytterbium opérant dans le régime de quelques cycles optiques.

La deuxième partie de cette thèse présente de nouvelles approches permettant la conversion de fréquence non-linéaire d'impulsions ultrabrèves vers les gammes spectrales du térahertz et du moyen infrarouge. Cette partie se décompose en trois sections principales. La première section présente le développement d'une source laser térahertz à large bande, compacte et économique, basée sur la conversion non-linéaire d'impulsions situées dans le proche infrarouge. La conversion est effectuée par rectification optique dans un cristal non-linéaire placé à l'intérieur de la cavité d'un laser femtoseconde Yb:CALGO. Cette configuration permet d'atteindre des niveaux d'efficacité et de puissance générée largement supérieurs à ce qui serait possible en plaçant le cristal non-linéaire à l'extérieur de la cavité. Le principal avantage de cette technique est donc de réduire fortement les exigences et donc la complexité du laser de pompe.

La section suivante décrit la génération d'impulsions ultracourtes dans le moyen-infrarouge basée sur le processus non-linéaire d'amplification paramétrique optique. La conversion est effectuée dans un guide-onde non-linéaire composé de niobate de lithium en couche mince sur substrat de saphire. En confinant la lumière dans de très petits volumes, ces guides-ondes sub-micrométriques permettent d'atteindre de hautes intensités optiques et offrent la possibilité de contrôler ses propriétés de dispersion. L'approche présentée dans cette section

exploite ces deux avantages pour effectuer l'amplification paramétrique dans une configuration où la longueur d'interaction non-linéaire n'est pas limitée par les vitesses de groupe des trois impulsions. Sous certaines conditions, les impulsions générées, à savoir le signal et son complémentaire, sont piégées proche de l'impulsion de pompe par l'interaction du gain non-linéaire et du déplacement temporel relatif des trois ondes. Dans le régime non saturé, ce piégeage permet l'amplification exponentielles des impulsions générées sur la totalité du guide-onde, quelque soit sa longueur, permettant ainsi une conversion non-linéaire très efficace. Dans cette étude, on observe que seulement quelques picojoules d'énergie incidente couplée à l'intérieur du guide d'onde suffisent pour atteindre le régime saturé. Une fois le régime saturé atteint, le transfert des photons de pompes dans la bande spectrale entre 3-4 μm se poursuit et atteint un maximum de 50% de conversion avec seulement une dizaine de picojoule d'énergie incidente. Étant donné l'efficacité du processus et les faibles besoins en puissance de pompe, cette approche est prometteuse pour la conversion de fréquence à des taux de répétition dépassant le gigahertz.

Dans la dernière section, les guides-ondes nanophotoniques de niobate de lithium sont utilisés pour la génération de supercontinuum et, consécutivement, la détection du décalage en fréquence entre l'enveloppe et la porteuse de l'onde incidente. Dans cette expérience, le supercontinuum est obtenu via le processus non-linéaire de génération d'harmoniques en cascade. En outre, les guide-ondes sont conçus de sorte à ce qu'une impulsion ultrabrève située autour de 2 μm se propage avec la même vitesse de groupe que sa deuxième harmonique à 1 μm . Dans ce cas, lorsque le processus est suffisamment saturé, l'élargissement spectral des deux harmoniques se produit via un processus d'interaction en cascade entre le désaccord de phase et la déplétion de la pompe. Dans cette étude, on observe la formation du supercontinuum avec seulement quelques dizaines de picojoule d'énergie incidente couplée dans le guide-onde. Le recouvrement spectral entre l'impulsion fondamentale et sa seconde harmonique permet la détection de la fréquence de décalage enveloppe-porteuse sans étape supplémentaire. Celle-ci est détectée simplement en focalisant la sortie du guide-onde sur une photodiode.

Enfin, il est intéressant de souligner la connection entre les deux parties de cette thèse. La première partie se consacre au développement de sources laser femtosecondes compactes et bas bruit émettant dans le proche infrarouge. La seconde partie étudie notamment la génération d'impulsions dans le moyen infrarouge basée sur la conversion en fréquence d'impulsions incidentes située dans le proche infrarouge. Ainsi, les sources laser développées dans la première partie, combinées avec ces techniques de conversion non-linéaires offrent la possibilité de réaliser des peignes de fréquences à hauts taux de répétition dans le moyen

infrarouge, possédant ainsi un intérêt certain pour de nombreuses applications en spectroscopie.

Contents

Keywords - Mots clés	v
Abstract	vii
Résumé	xi
Contents	xv
List of acronyms	xix
Publication list	xx
1 Introduction	1
2 Powerful and broadband optical frequency combs	11
2.1 Efficient high-power sub-50-fs gigahertz repetition rate diode-pumped solid-state laser	12
2.1.1 Article outline	12
Context	12
Key results	12
Conclusion	13
2.1.2 Further discussion	13
Spectral bandwidth limitations	13
Performance degradation in long-term operation	13
2.1.3 Appendix: Published article	15
Introduction	15
Experimental setup	17
Experimental results	19
Conclusion	20
2.2 Powerful 1- μm 1-GHz optical frequency comb	23
2.2.1 Article outline	23
Context	23

	Key results	23
	Comparison to state-of-the-art optical frequency combs	24
	Conclusion	24
2.2.2	Further discussion	25
	Comment about noise comparison between systems . .	25
	All-glued version of the GHz laser oscillator	25
2.2.3	Acknowledgment	27
2.2.4	Appendix: Published article	28
	Introduction	28
	Setup	29
	Experimental results	30
	Comparison to state-of-the-art optical frequency combs	33
	Conclusion	34
2.3	Efficient few-cycle Yb-doped laser oscillator with Watt-level average power	37
2.3.1	Article outlines	37
	Context	37
	Results	38
	Conclusion	39
2.3.2	Towards a cost-efficient version: multimode diode pumping	39
	Experimental setup	39
	Experimental results	40
	Comparison to state-of-the-art mode-locked lasers . . .	41
	Outlook	42
2.3.3	Acknowledgment	43
2.3.4	Appendix: Published article	44
	Introduction	44
	Experimental setup	47
	Experimental results for the shortest pulse duration . .	49
	Experimental results for the highest average output power	50
	Limiting impact of a standard dichroic mirror	51
	Conclusion	52
2.4	Chapter conclusion	55
3	Towards low-power efficient nonlinear frequency conversion	59
3.1	Intra-oscillator broadband THz generation in a compact ultrafast diode-pumped solid-state laser	60
3.1.1	Article outline	61
	Context	61
	Results	62

	Conclusion	62
3.1.2	Further discussion	63
	Comparisons with previous intra-oscillator approaches	63
	Comparison with our thin-disk result	64
	Limitations and prospects	65
3.1.3	Acknowledgment	65
3.1.4	Appendix: Published article	66
	Introduction	66
	Experimental setup	67
	Experimental results	68
	Conclusion	70
3.2	Efficient parametric downconversion by gain-trapped solitons	73
3.2.1	Article outline	73
	Context	73
	Results	74
	Conclusion	75
3.2.2	Further discussion: eigenmode decomposition	76
3.2.3	Acknowledgment	78
3.2.4	Appendix: Published article	79
	Introduction	79
	Theory and design	80
	Experimental results	84
	Conclusion	88
3.3	Picojoule-level supercontinuum generation in thin-film lithium niobate on sapphire	90
3.3.1	Article outline	90
	Context	90
	Results	91
	Conclusion	91
3.3.2	Further discussion	92
	Group velocity mismatch of the fabricated waveguides	92
	Estimation of the coupled power	93
3.3.3	Acknowledgment	95
3.3.4	Appendix: Published article	96
	Introduction	96
	Design of the waveguides	97
	Experimental setup	98
	Supercontinuum generation	99
	Carrier-envelope offset frequency detection	101
	Conclusion	102

3.4 Chapter conclusion	104
4 Conclusion	111
4.1 Summary of this dissertation	111
4.2 Outlook	113
Acknowledgments - Remerciements	119
Curriculum Vitae	121
Déclaration sur l'honneur	123

List of acronyms

CWE	Coupled-wave equation
DFG	Difference frequency generation
DPSSL	Diode pumped solid-state laser
FWHM	Full width at half-maximum
GDD	Group delay dispersion
GVM	Group velocity mismatch
GVD	Group velocity dispersion
IP-DFG	Intra-pulse difference frequency generation
f_{CEO}	Carrier-envelope offset frequency
KLM	Kerr-lens mode-locked, Kerr-lens mode-locking
MIR	Mid-infrared
NIR	Near-infrared
OFC	Optical frequency comb
OPA	Optical parametric amplification, Optical parametric amplifier
OR	Optical rectification
PCF	Photonic crystal fiber
PSD	Power spectral density
PPLN	Periodically poled lithium niobate
QCL	Quantum cascade laser
RF	Radio-frequency
SCG	Supercontinuum generation
SESAM	Semiconductor saturable absorber mirror
SHG	Second harmonic generation
SNR	Signal-to-noise ratio
SPM	Self-phase modulation
TFLN	Thin-film lithium niobate
THz	Terahertz
Ti	Titanium
Tm	Thulium
VBG	Volume Bragg grating
Yb	Ytterbium

Publication list

Journal papers

- [1] M. Hamrouni, J. Drs, N. Modsching, V. J. Wittwer, F. Labaye, and T. Südmeyer, “Intra-oscillator broadband THz generation in a compact ultrafast diode-pumped solid-state laser”, *Optics Express* **29**, 23729 (2021).
- [2] F. Labaye, V. J. Wittwer, M. Hamrouni, N. Modsching, E. Cormier, and T. Südmeyer, “Efficient few-cycle Yb-doped laser oscillator with Watt-level average power”, *Optics Express* **30**, 2528 (2022).
- [3] M. Hamrouni, F. Labaye, N. Modsching, V. J. Wittwer, and T. Südmeyer, “Efficient high-power sub-50-fs gigahertz repetition rate diode-pumped solid-state laser”, *Optics Express* **30**, 30012 (2022).
- [4] M. Müller, M. Hamrouni, K. N. Komagata, A. Parriaux, V. J. Wittwer, and T. Südmeyer, “Powerful 1- μ m 1-GHz optical frequency comb”, *Optics Express* **31**, 44823 (2023).
- [5] M. Hamrouni, M. Jankowski, A. Y. Hwang, N. Jornod, J. Mishra, S. S. Stokowski, T. P. McKenna, C. Langrock, T. Südmeyer, A. Safavi-Naeini, and M. M. Fejer, “Efficient parametric downconversion by gain-trapped solitons”, Accepted in *Optica*, (2024).
- [6] M. Hamrouni, M. Jankowski, A. Y. Hwang, N. Flemens, J. Mishra, C. Langrock, A. Safavi-Naeini, M. M. Fejer, and T. Südmeyer, “Picojoule-level supercontinuum generation in thin-film lithium niobate on sapphire”, Submitted to *Optics Express*, (2024).

Conference papers

- [1] M. Hamrouni, J. Drs, J. Fischer, N. Modsching, V. J. Wittwer, L. François, and T. Südmeyer, “Powerful broadband intracavity THz generation in a compact ultrafast diode-pumped laser oscillator”, in 9th EPS-QEOD Europhoton Conference (2020), Tu–A1.7.
- [2] M. Hamrouni, J. Drs, J. Fischer, K. Komagata, N. Modsching, V. J. Wittwer, F. Labaye, and T. Südmeyer, “Intra-Cavity Broadband THz Generation Inside a Diode-Pumped Solid-State Laser Oscillator”, in Conference on Lasers and Electro-Optics (2021), SW3K.5.

- [3] M. Hamrouni, J. Drs, J. Fischer, K. Komagata, N. Modsching, V. J. Wittwer, F. Labaye, and T. Südmeyer, “Powerful Broadband Intra-Oscillator THz Generation Inside a Kerr-Lens Mode-Locked Diode-Pumped Laser Cavity”, in 2021 Conference on Lasers and Electro-Optics Europe and European Quantum Electronics Conference (2021), cc_3_5.
- [4] M. Hamrouni, F. Labaye, N. Modsching, V. J. Wittwer, and T. Südmeyer, “Powerful Sub-100-fs Diode-Pumped Solid-State Laser Oscillator Operating at Gigahertz Repetition Rate”, in Conference on Lasers and Electro-Optics (2022), SF4E.3.
- [5] M. Hamrouni, A. Hwang, M. Jankowski, J. Mishra, H. S. Stokowski, T. P. McKenna, N. Jornod, C. Langrock, T. Südmeyer, A. H. Safavi-Naeini, and M. M. Fejer, “Efficient and Broadband Generation of Mid-Infrared Pulses by Optical Parametric Amplification in Dispersion-Engineered Thin Film Lithium Niobate”, in Solid-State, Fibre, And Waveguide Coherent Light Sources, Vol. 267 (2022), TUE–FWD–1.4.
- [6] M. Hamrouni, A. Hwang, M. Jankowski, N. Jornod, J. Mishra, H. S. Stokowski, T. P. McKenna, C. Langrock, T. Südmeyer, A. H. Safavi-Naeini, and M. M. Fejer, “Efficient and broadband mid-infrared source based on optical parametric amplification in dispersion-engineered thin film Lithium Niobate”, in Ultrafast Optics 2023 - UFOXIII (2023), Tu3.2.
- [7] M. Hamrouni, M. Jankowski, A. Hwang, N. Jornod, J. Mishra, H. S. Stokowski, T. P. McKenna, C. Langrock, T. Südmeyer, A. H. Safavi-Naeini, and M. M. Fejer, “Efficient Broadband Mid-Infrared Optical Parametric Amplification in Nanophotonic Waveguides”, in CLEO 2023 (2023), SW4G.4.

Chapter 1

Introduction

The aim of this introduction is to provide a general context for the work realized during my Ph.D research. Careful attention has been paid to highlighting the interconnections between the different topics. For the sake of readability, more detailed contexts and state-of-the-art reviews specific to each topic are presented in the relevant sections, rather than in this introductory chapter.

The emergence of lasers

The laser revolution started in 1960 with the first experimental demonstration achieved by Theodore Maiman [1]. Shortly after, in 1961, the ruby laser was used to destroy a retinal tumor, proving the great potential of the technology for real-world applications. Over the decades, research in laser development and applications has grown exponentially, leading to disruptive impacts in numerous areas such as telecommunications, geolocation, medical diagnostics and nuclear energy. In other words, lasers are ubiquitous in our everyday lives and their impact on society is only expected to grow for the next decades.

Origins of femtosecond mode-locked lasers

Since the first demonstration of mode-locked lasers in 1966 by De Maria *et al.* [2], ultrafast optical sources have been developing rapidly. Before the late 80s, ultrafast optics was dominated by dye lasers. These mode-locked lasers were the first to generate sub-picosecond pulses [3], and also the first to allow post-compression down to few-cycles [4]. The discovery of the Ti:sapphire gain material in the 80s led to a paradigm shift in the generation of ultrashort pulses. By having the necessary spectral bandwidth to support femtosecond

pulses, this gain material emerged as a promising solution to develop compact ultrafast sources at lower cost and reduced complexity. The progress in Ti:sapphire technologies, in parallel to the development of dispersion management techniques [5], led to the first laser directly producing pulses in the sub-100-fs regime [6]. Following this breakthrough, numerous studies focused on pushing the pulse duration toward the single-cycle limit. In ten years, the pulse duration was decreased from 60 fs in 1991 to 8 fs in 1995 [7], and further compressed to the single-cycle regime in 2001 [8]. These milestones did more than setting scientific records; they revolutionized many domains, including high-field physics, attosecond science, and spectroscopy. Among the different advances, these femtosecond mode-locked lasers have enabled the development and sophistication of optical frequency combs (OFCs), representing one of the main advances in optics.

Optical frequency combs

OFCs are characterized by an optical spectrum consisting of a set of frequency lines that are equally spaced. In this manner, they function as exceptionally precise rulers, enabling rapid and highly accurate measurements of optical frequencies and their related quantities [9]. Pioneering studies were awarded the 2005 Nobel prize [10, 11]. Traditionally, OFCs are obtained by detecting the output of a mode-locked laser oscillator with a photodiode that is slow compared to the pulse duration. In this case, the periodic structure of the pulse train reaching the detector translates to a Dirac comb in the frequency domain. The resulting spectral comb structure is easily formalized as follows,

$$f_n = f_0 + n f_r \quad (1.1)$$

where f_n is the frequency of the index- n comb teeth, f_r is the equidistant spacing between each line, and f_0 is a global offset [12]. When produced by a mode-locked laser, the repetition frequency f_r typically lies in the radio frequency domain from a few megahertz to a few gigahertz. Hence, the integer n makes the link between the radio frequency to the optical domain. f_0 refers to the carrier-envelope offset frequency (f_{CEO}), which represents the modulo difference between the pulse-train repetition rate and the optical modes of the cavity. This offset comes from the pulse-to-pulse shift of the position of the carrier with respect to the envelope. Since this definition is valid for any mode-locked laser, we may legitimately wonder about the difference between a mode-locked laser and an optical frequency comb. In free-running operation, mode-locked lasers are prone to excessive noise, causing all comb lines to shift unpredictably. In contrast, OFC sources feature stabilized and controlled frequency parameters.

If the difference seems subtle, it is actually what makes OFCs such a powerful tool. In practice, OFCs are realized by stabilizing both the f_r and f_{CEO} of the mode-locked source. Originally, only the repetition rate could be stabilized and controlled, and the first spectroscopic applications operated with free running f_{CEO} [13]. It was only in the early 2000 that direct measurement of f_{CEO} , namely self-referencing, became possible [14–16]. The detection and control of the f_{CEO} enabled the emergence of fully-stabilized comb sources, characterized by unprecedented noise performances that allow for highly accurate frequency measurements. Since the two last decades, many studies have been focusing on improving the performance of mode-locked laser and OFC sources [17], in addition to broadening their scope of applications [18]. Nevertheless, despite major advances, applications of OFCs outside research laboratories remain limited, and their potential for disruptive real-world applications still largely untapped. The insufficient maturity of the technology and the prohibitive cost and size of such sources stand out as key reasons for their limited widespread adoption. A significant part of this thesis is dedicated to the development of state-of-the-art OFCs, characterized by simple, compact and cost-effective implementations.

Towards cost-efficient and high-power optical frequency combs

Since the past two decades, alternative methods for generating OFCs have been developed, such as microresonators [19], quantum cascade lasers [20] or electro-optic modulators [21]. However, mode-locked lasers remain the most mature technology. One major advantage is that mode-locked lasers can readily deliver ultrashort pulses with broad spectral bandwidths. Since the amplitude of the comb lines is modulated by the envelope of the pulses, large spectral bandwidths provide a greater number of comb lines, which is desirable for many applications. In this view, laser materials with broad gain bandwidths directly supporting femtosecond pulses, such as Ti:sapphire, are ideal candidates. In addition to the spectral bandwidth of the comb, one can intuit that the power per comb line is another key parameter. Thus, ideal gain material must not only allow the generation of ultrashort pulses but also support high power levels. Historically, Ti:sapphire lasers were the leading OFC platform due to their ability to produce broad spectra. However, they feature technical limitations hindering high-power operation. Because of the large frequency difference between the pump and laser photons, namely the quantum-defect, the energy that is not consumed by the stimulated emission is dissipated through heat, which leads to detrimental thermal effects at high-power operation. To mitigate this limitation, powerful Ti:sapphire lasers typically require complex cooling that may preclude their use beyond laboratory settings. Another limiting argument

is the cost of the pumping system. Although pump diodes compatible with Ti:sapphire are now available, this solution did not supplant the conventional pumping approach based on an expensive high-performance green laser. Together, these limitations obstruct further scaling of the power performance, and often restrict its use to research applications. After dominating the field of ultrafast science for many years, more than a decade ago Ti:sapphire slowly started to yield ground to a novel class of gain materials based on Ytterbium (Yb). Compared to Ti:sapphire, Yb-based gain materials have narrower gain bandwidths but feature a much smaller quantum defect, which is favorable for high power operations. Also, the massive development of commercially available pump diodes compatible with Yb-doped crystals has enabled to decrease the cost of the pump power in dollars per watt by more than an order of magnitude. This naturally stimulated the development of powerful and ultrafast Yb-based laser oscillators utilizing cost-efficient pump diodes. As a result, years of research in this direction have made Yb-based lasers the standard technology for the generation of femtosecond pulses at high power levels. Nevertheless, the pulse duration and maximum power are not the only important parameters for realizing functional OFCs, which foremost require low-noise operation. As discussed in more details in the next chapter, achieving high-power levels and low-noise operation simultaneously is challenging since higher average power is often a source of additional noise. Due to this technical constraint, most commercially available low-noise comb sources still operate below hundreds of milliwatts of average power, whereas numerous applications would benefit from at least a 10-fold increase of the power levels. Driven by applications' need, the first part of this thesis is dedicated to leveraging the potential of Yb-based materials to develop compact low-noise OFC sources that combine high-power levels and broad spectral bandwidths.

Frequency conversion into spectroscopic-relevant regions

Mode-locked lasers are the most mature technology to realize broadband OFCs, but their spectral versatility is constrained by the characteristics of the gain material. Commercially-available ultrafast lasers, which form the basis of many OFC sources, typically operate within three wavelength regimes: around 800 nm when utilizing Ti:sapphire, 1050 nm with Yb-doped crystals, and 1500 nm in the case of Er-based systems. Although novel gain materials such as Tm, Ho or Cr-based crystals generate light slightly above 2 μm [22], extension to longer wavelengths is challenging. This limitation represents a severe disadvantage in spectroscopy where operation in the mid-infrared or terahertz frequency ranges is much more pertinent [23, 24]. A solution to overcome this limitation is to

frequency convert the laser wavelength via nonlinear approaches. In principle, nonlinear frequency conversion can be used to generate wavelengths almost everywhere from the XUV [25, 26] to the terahertz range [27]. However, in practice achieving efficient and broadband frequency conversion faces two main challenges. First, when using ultrashort driving pulses, it is not straightforward to achieve the frequency conversion across the entire spectral bandwidth. Astute approaches are often required to circumvent this limitation. Secondly, efficient nonlinear conversions inherently demand high field intensities, which imposes stringent power requirements on the driving sources and presents technical challenges. Over the decades, many efforts have been dedicated to achieving efficient and broadband nonlinear optics at low power requirements, and this remains an ongoing challenge in the field.

Over the decades, numerous research projects have been focusing on decreasing the power and energy requirements to realize nonlinear optical sources with continually smaller footprints and reduced complexities. Reducing the power requirement can be addressed by driving the process in more efficient configurations or employing more efficient nonlinear media. In this perspective, many efforts have been made to develop nonlinear materials and platforms with ever-increasing efficiencies. Among them, lithium niobate (LN) has been a pivotal material for nonlinear optics and frequency conversion. Since its first synthesis in 1949, LN has been developed upon three main platforms, namely bulk crystals, weakly confining waveguides, and tightly confining waveguides [28]. Originally based on bulk crystals, the first LN platform was severely limited by the trade-off between large intensities and long interaction lengths. Years of research led to major advances such as quasi-phases matching [29] and the development of waveguiding structures [30, 31], which enables mitigation of this limitation. Hence, the power requirement radically decreased by two to three orders of magnitude compared to previous bulk devices. One of the latest breakthroughs has been the development of nanophotonic waveguide structures that confine the light inside subwavelength mode volumes. Besides featuring large nonlinear coupling, this new class of integrated devices offers additional degrees of freedom to engineer the optical properties, for example, through dispersion engineering. These unique features have enabled to further decrease the power required for frequency conversion by several orders of magnitude compared to previous nonlinear platforms. Today, thin film lithium niobate (TFLN) is among the leading nanophotonic platforms for frequency conversion at low power requirements [28, 32]. In the final sections of the thesis, we leverage these advantages for revisiting nonlinear processes at reduced power requirements.

Overview of the dissertation

The primary goal of this thesis was to develop novel methods for generating, stabilizing, and frequency converting short pulses of light. The document is organized as follows. Chapter 2 reports on the development of a powerful Kerr-lens mode-locked Yb:CALGO laser oscillator operating at 1 GHz repetition rate. The full stabilization of the laser is presented in a subsequent section. The stabilized source demonstrates low-noise operation with sub-50-fs pulses and several Watts of average power available for applications. Additionally, this chapter introduces a novel approach to overcome the limitations imposed by the low-quantum defect in Yb-based lasers, a significant obstacle to the efficient generation of few-cycle pulses. Our technique is based on a novel pumping scheme that readily enables the generation of spectral bandwidths extending beyond the pump wavelength. Our approach significantly enhances the optical-to-optical efficiency compared to other Yb-doped sources operating in the few-cycle regime.

In chapter 3, we revisit established techniques and explore new avenues for efficient nonlinear frequency conversion at reduced power requirements. In the first section, we demonstrate a simple and efficient approach to broadband terahertz generation. In contrast to conventional methods where the nonlinear conversion is driven by the output of a laser, we achieve the nonlinear conversion directly inside the cavity of an ultrafast Yb:CALGO bulk oscillator. By exploiting the power levels available inside the cavity, we demonstrate a 10-fold increase of the efficiency with respect to pump power compared to similar technologies.

In the second and third sections, we harness recent advances in thin-film lithium niobate (TFLN) technologies for picojoule-level nonlinear optics. In the second section, we demonstrate an approach to optical parametric amplification (OPA) that efficiently down-converts near-infrared femtosecond picojoule-level pulses in the 3-4 μm band where many relevant molecules display strong absorption lines. This technique relies on the dispersion engineering available in TFLN-on-sapphire to operate in a nonlinear regime optimized for efficient nonlinear interactions. In the article, we present a theoretical study of this nonlinear regime as well as its first experimental demonstration inside integrated devices.

In the final section, we present an approach to supercontinuum generation (SCG) and f_{CEO} detection performed inside dispersion-engineered TFLN on sapphire nanowaveguides. With tens of picojoules of input pulse energies, we generate a broad supercontinuum spanning from the ultraviolet to the mid-infrared spectral regions. The generated supercontinuum directly produces f-to-2f beatnotes that we detect at the waveguide output. This work establishes TFLN-on-sapphire as a viable platform for broadband and efficient nonlinear

conversion and offers a simple solution for self-referencing 2- μm lasers.

All the sections of this thesis are based on articles that have been published or submitted to peer-reviewed journals. To enhance readability and clarity, I have prefaced each article with a summary that contextualizes the work and underscores the main results. While these summaries provide an essential understanding of the study, they do not encapsulate the full spectrum of challenges, methodologies, accomplishments, and implications inherent in the work. Therefore, a study of the articles is recommended for a greater insight. Additionally, these works are sometimes supplemented with further discussions or results that do not appear in the published manuscript, offering expanded perspectives and additional commentary on the conducted research.

References

- [1] T. H. Maiman et al., “Stimulated Optical Radiation in Ruby”, (1960).
- [2] A. DeMaria, D. Stetser, and H. Heynau, “Self mode-locking of lasers with saturable absorbers”, *Applied Physics Letters* **8**, 174 (1966).
- [3] C. Shank and E. Ippen, “Subpicosecond kilowatt pulses from a mode-locked cw dye laser”, *Applied Physics Letters* **24**, 373 (1974).
- [4] R. L. Fork, C. B. Cruz, P. Becker, and C. V. Shank, “Compression of optical pulses to six femtoseconds by using cubic phase compensation”, *Optics letters* **12**, 483 (1987).
- [5] R. Fork, O. Martinez, and J. Gordon, “Negative dispersion using pairs of prisms”, *Optics letters* **9**, 150 (1984).
- [6] D. E. Spence, P. N. Kean, and W. Sibbett, “60-fsec pulse generation from a self-mode-locked Ti: sapphire laser”, *Optics letters* **16**, 42 (1991).
- [7] A. Stingl, M. Lenzner, C. Spielmann, F. Krausz, and R. Szipöcs, “Sub-10-fs mirror-dispersion-controlled Ti: sapphire laser”, *Optics letters* **20**, 602 (1995).
- [8] R. Ell, U. Morgner, F. X. Kärtner, J. G. Fujimoto, E. P. Ippen, V. Scheuer, G. Angelow, T. Tschudi, M. J. Lederer, A. Boiko, et al., “Generation of 5-fs pulses and octave-spanning spectra directly from a Ti: sapphire laser”, *Optics letters* **26**, 373 (2001).
- [9] S. A. Diddams, K. Vahala, and T. Udem, “Optical frequency combs: Coherently uniting the electromagnetic spectrum”, *Science* **369**, eaay3676 (2020).

- [10] T. W. Hänsch, “Nobel Lecture: Passion for Precision”, *Rev. Mod. Phys.* **78**, 1297 (2006).
- [11] J. L. Hall, “Nobel Lecture: Defining and Measuring Optical Frequencies”, *Rev. Mod. Phys.* **78**, 1279 (2006).
- [12] T. Udem, R. Holzwarth, and T. W. Hänsch, “Optical frequency metrology”, *Nature* **416**, 233 (2002).
- [13] T. Udem, J. Reichert, R. Holzwarth, and T. Hänsch, “Absolute optical frequency measurement of the cesium D 1 line with a mode-locked laser”, *Physical review letters* **82**, 3568 (1999).
- [14] H. R. Telle, G. Steinmeyer, A. E. Dunlop, J. Stenger, D. H. Sutter, and U. Keller, “Carrier-envelope offset phase control: A novel concept for absolute optical frequency measurement and ultrashort pulse generation”, *Applied Physics B* **69**, 327 (1999).
- [15] A. Apolonski, A. Poppe, G. Tempea, C. Spielmann, T. Udem, R. Holzwarth, T. W. Hänsch, and F. Krausz, “Controlling the phase evolution of few-cycle light pulses”, *Physical Review Letters* **85**, 740 (2000).
- [16] D. J. Jones, S. A. Diddams, J. K. Ranka, A. Stentz, R. S. Windeler, J. L. Hall, and S. T. Cundiff, “Carrier-envelope phase control of femtosecond mode-locked lasers and direct optical frequency synthesis”, *Science* **288**, 635 (2000).
- [17] U. Keller, “Recent developments in compact ultrafast lasers”, *nature* **424**, 831 (2003).
- [18] T. Fortier and E. Baumann, “20 years of developments in optical frequency comb technology and applications”, *Communications Physics* **2**, 153 (2019).
- [19] T. J. Kippenberg, A. L. Gaeta, M. Lipson, and M. L. Gorodetsky, “Dissipative Kerr solitons in optical microresonators”, *Science* **361**, eaan8083 (2018).
- [20] A. Hugi, G. Villares, S. Blaser, H. Liu, and J. Faist, “Mid-infrared frequency comb based on a quantum cascade laser”, *Nature* **492**, 229 (2012).
- [21] A. Parriaux, K. Hammani, and G. Millot, “Electro-optic frequency combs”, *Advances in Optics and Photonics* **12**, 223 (2020).
- [22] S. Vasilyev, I. Moskalev, V. Smolski, J. Peppers, M. Mirov, Y. Barnakov, V. Fedorov, D. Martyshkin, S. Mirov, and V. Gapontsev, “Kerr-lens mode-locked Cr: ZnS oscillator reaches the spectral span of an optical octave”, *Optics Express* **29**, 2458 (2021).

-
- [23] A. Schliesser, N. Picqué, and T. W. Hänsch, “Mid-infrared frequency combs”, *Nature photonics* **6**, 440 (2012).
- [24] M. C. Beard, G. M. Turner, and C. A. Schmuttenmaer, “Terahertz spectroscopy”, *The Journal of Physical Chemistry B* **106**, 7146 (2002).
- [25] M. Ferray, A. L’Huillier, X. Li, L. Lompre, G. Mainfray, and C. Manus, “Multiple-harmonic conversion of 1064 nm radiation in rare gases”, *Journal of Physics B: Atomic, Molecular and Optical Physics* **21**, L31 (1988).
- [26] A. L’Huillier, K. J. Schafer, and K. C. Kulander, “Theoretical aspects of intense field harmonic generation”, *Journal of Physics B: Atomic, Molecular and Optical Physics* **24**, 3315 (1991).
- [27] P. H. Siegel, “Terahertz technology”, *IEEE Transactions on microwave theory and techniques* **50**, 910 (2002).
- [28] A. Boes, L. Chang, C. Langrock, M. Yu, M. Zhang, Q. Lin, M. Lončar, M. Fejer, J. Bowers, and A. Mitchell, “Lithium niobate photonics: Unlocking the electromagnetic spectrum”, *Science* **379**, eabj4396 (2023).
- [29] M. M. Fejer, G. Magel, D. H. Jundt, and R. L. Byer, “Quasi-phase-matched second harmonic generation: tuning and tolerances”, *IEEE Journal of quantum electronics* **28**, 2631 (1992).
- [30] I. Kaminow and J. Carruthers, “Optical waveguiding layers in LiNbO₃ and LiTaO₃”, *Applied Physics Letters* **22**, 326 (1973).
- [31] J. L. Jackel, C. Rice, and J. Veselka, “Proton exchange for high-index waveguides in LiNbO₃”, *Applied Physics Letters* **41**, 607 (1982).
- [32] D. Zhu, L. Shao, M. Yu, R. Cheng, B. Desiatov, C. Xin, Y. Hu, J. Holzgrafe, S. Ghosh, A. Shams-Ansari, et al., “Integrated photonics on thin-film lithium niobate”, *Advances in Optics and Photonics* **13**, 242 (2021).

Chapter 2

Powerful and broadband optical frequency combs

Over the decades, OFCs have become an indispensable tool with a wide array of applications in fields like spectroscopy, metrology and microwave generation to name just a few [1, 2]. The ever-growing interest in pushing the boundaries of OFC technology has led to the development of novel ultrafast laser oscillators and the improvement of existing sources. One significant area of focus has been pushing the technology towards larger comb-line spacing. Most commercially available ultrafast lasers used as OFC source typically operate with repetition rates below a few hundreds of megahertz. However, in applications such as spectroscopy and metrology, where extremely high resolution is not always necessary, it can be advantageous to operate at higher repetition rates [1, 3]. For instance, lasers operating at gigahertz repetition rates offer comb-line densities that are often sufficient to resolve molecular absorption features, and enables both faster measurement and higher power per comb line than their 100-MHz counterparts. To address this need, there is a current trend to push the repetition rates of mode-locked lasers toward multi-gigahertz. Nevertheless, achieving large spectral bandwidths at high repetition rate is often challenging. Among various available platforms (bulk, fiber, semiconductor), laser oscillators based on Yb-doped bulk gain materials have demonstrated their suitability for both high-power and ultrafast operations at the gigahertz level of repetition rate [4–7]. Following the path of advancing this class of laser sources, this chapter starts with the development of a powerful and broadband Yb:CALGO laser oscillator operating at 1 GHz repetition rate. In the subsequent section we perform the full stabilization of the laser, turning the initial free-running source into a

powerful and broadband low-noise OFC.

Increasing the spectral bandwidth is also of high interest. However, while Yb-doped gain materials are favorable for high-power operation, they are inherently less suited than Ti:sapphire for the generation of few-cycle pulses. In the final section of this chapter, we discuss this limitation and introduce a new technique designed to address the challenge.

2.1 Efficient high-power sub-50-fs gigahertz repetition rate diode-pumped solid-state laser

2.1.1 Article outline

Context

This article introduces a diode-pumped Kerr-lens mode-locked Yb:CALGO laser oscillator operating at 1-GHz of repetition rate. The article starts with an overview of laser oscillators that operate above 1-GHz of repetition rate and achieve state-of-the-art average and peak power levels (Fig. 1 from the article). This overview reveals that although Ti:sapphire currently maintains the record for the highest peak power [8], Yb-based sources are rapidly advancing towards surpassing this record and have already outperformed it in terms of average power. Thanks to their excellent thermal properties, combined with the availability of multi-watt pump diodes that allow for cost-efficient and compact systems, Yb-based crystals have attracted high interest for more than a decade. Within this category, lasers utilizing semiconductor saturable absorber mirror (SESAM) mode-locking have been particularly successful [4, 5, 9–11].

Kerr-lens mode-locking, commonly used in Ti:sapphire lasers for producing few-cycle pulses, is known for enabling shorter pulse durations compared to SESAM. Prior to this article, only a single Yb-based laser oscillator based on KLM achieved watt-levels of average power [12]. In this work, we further harness the potential of KLM to push the technology towards shorter pulse durations. To achieve this, we employ Yb:CALGO gain crystals, known for their broad gain bandwidth [13, 14], in addition to good thermal properties [15, 16] facilitating high-power operations.

Key results

In the article we present a diode-pumped Yb:CALGO laser oscillator operating at 1-GHz of repetition rate. We present two laser configurations. In a first configuration optimized for high average power, when pumped with 18.5 W the oscillator generates 93-fs pulses at 6.9 W of average power. Remarkably, despite

the multimode pumping and presence of the hard-aperture that increases the cavity losses, this configuration achieves up to 37% optical-to-optical efficiency. In a second configuration we optimize the laser for short pulse durations and achieve sub-50-fs pulses at 74 kW of peak power using 19.5 W of pump power.

Conclusion

As illustrated by the overview, this system demonstrates the shortest pulse duration, highest average power and peak power with respect to previous GHz-class Yb-based laser oscillators. Given the short pulse durations and high peak power levels that readily enable f-to-2f self-referencing, this laser represents a promising source for the generation of broadband OFC.

2.1.2 Further discussion

Spectral bandwidth limitations

In the configuration optimized for short pulse duration, the measured spectrum shows the presence of a dispersive wave centered around 1114 nm as well as a small pedestal below 1000 nm (Fig. 3a of the article). These spectral features are due to the strong variations of the group delay dispersion in the tails of the generated spectrum. In this regime, the bandwidth of the group delay dispersion becomes comparable to that of the spectrum, indicating that achieving broader spectra and shorter pulse durations will be challenging with the current setup. One immediate solution to mitigate this issue is the use of dispersive mirrors with a broader bandwidth. Unfortunately, such mirrors were not available in our lab at the time of submission. Furthermore, while this is a first step toward reducing the pulse duration, further scaling will ultimately be limited by the low quantum defect of the Yb:CALGO crystal. Due to the collinear-pumping configuration, the absorption peak of the crystal around 980 nm severely hinders the expansion of the spectrum toward shorter wavelengths. We further discuss this point in section 2.3, where we provide an alternative pump scheme that overcomes this limitation.

Performance degradation in long-term operation

The laser was operated for several hours continuously in the mode-locked regime without interruption. However, we observed a gradual drift in output and peak power, eventually accompanied by the onset of continuous wave content in the spectrum. These degradations are mainly due to thermal effects and mechanical instabilities of the cavity components. It is clear that these effects preclude the use of the source for applications beyond the laboratory. However, since they become noticeable only after hours of operation and the initial performance can

be retrieved simply realigning the laser cavity, this system is still a viable solution for many in-lab applications. Furthermore, we circumvent these limitations by designing a more robust version of this laser, as detailed in section 2.2.2.



Efficient high-power sub-50-fs gigahertz repetition rate diode-pumped solid-state laser

MARIN HAMROUNI,^{*}  FRANÇOIS LABAYE, 
NORBERT MODSCHING,  VALENTIN J. WITTEW, 
AND THOMAS SÜDMEYER 

Laboratoire Temps-Fréquence (LTF), Institut de Physique, Université de Neuchâtel, Avenue de Bellevaux 51, 2000 Neuchâtel, Switzerland

*marin.hamrouni@unine.ch

Abstract: In this article we present a directly diode-pumped high-power Kerr-lens mode-locked Yb:CALGO bulk laser oscillator operating at 1-GHz repetition rate. We report on two laser configurations optimized for either highest average power or shortest pulse duration. In the first configuration optimized for high average power, the oscillator delivers up to 6.9 W of average power, which is the highest average power of any ultrafast laser oscillator operating at gigahertz repetition rate. The 93-fs pulses have a peak power of 64 kW, and the optical-to-optical efficiency amounts to 37%. In the second configuration optimized for short pulse duration, we demonstrate 48-fs pulses at 4.1 W of average power corresponding to a higher peak power of 74 kW with 21% optical-to-optical efficiency. This is the shortest pulse duration and the highest peak power demonstrated by any GHz-class Yb-based laser oscillator. The compact laser setup is directly pumped by a low-cost multimode fiber-coupled laser diode and has a high potential as an economical yet powerful source for various applications.

© 2022 Optica Publishing Group under the terms of the [Optica Open Access Publishing Agreement](#)

1. Introduction

Ultrafast laser sources have become a cornerstone technology for numerous industrial applications and fundamental research systems. Low-cost ultrafast laser oscillators operating at repetition rates in the gigahertz range are highly attractive for many areas such as spectroscopy [1,2], medical imaging [3–5], and quantum optics [6–8]. For instance, in frequency-comb-based spectroscopy, higher repetition rates result in a larger comb-mode spacing and a higher power per comb mode, which facilitates the use of individual lines. Repetition rates in the gigahertz range are also beneficial in quantum applications relying on entangled photons. As the generation rate must remain smaller than one pair of entangled photons per driving pulse, gigahertz repetition rates enable higher entangled-photon flux, offering the potential for an improved signal-to-noise ratio [9].

These different applications typically rely on nonlinear processes such as supercontinuum or second harmonic generation which strongly benefit from higher peak power and higher pulse energy. Although tens of kilowatts of peak power are routinely available from MHz-class bulk laser oscillators (see e.g., [10–16]), such performance is more challenging to achieve at gigahertz-level repetition rates as it requires more than a ten-fold increase in the average power or decrease in the pulse duration. As a result, only a few GHz-class laser oscillators, capable of delivering a high peak power combined with high average power, have been demonstrated so far [Fig. 1].

A first technology capable of delivering GHz-repetition-rate pulses are fiber-laser systems [17–20]. They provide compactness, high efficiency, and excellent reliability, but typically need an amplification process to achieve several watts of average power, increasing the cost

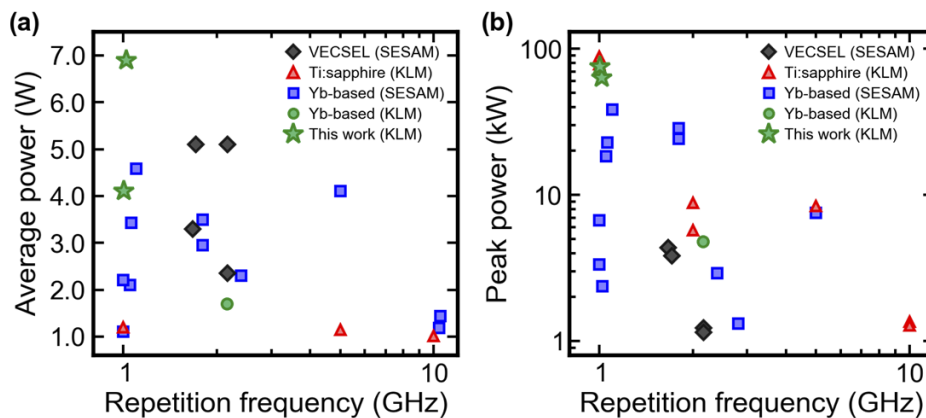


Fig. 1. Overview about state-of-the-art GHz-class laser oscillators operating at ≥ 1 GHz of repetition rate and demonstrating (a) > 1 W of average power and (b) directly generating pulses with > 1 kW of peak power. The different laser technologies are distinguished by Kerr-lens mode-locking (KLM) and mode-locking using a saturable absorber mirror (SESAM). Presented results of this work are highlighted as green stars.

and complexity of the system [21–23]. Additionally, the amplified pulses usually exhibit strong spectral features and a low temporal contrast which ultimately limits the achievable peak power.

Laser oscillators based on a semiconductor gain medium have already provided watts of average power at gigahertz repetition rates directly at the output of the laser cavity. In 2013, a vertical-external-cavity surface-emitting laser (VECSEL) reached up to 3.3 W of average power at 1.7 GHz repetition rate [24]. However, the comparably long pulse duration of 400 fs led to a peak power of only 4.3 kW. Although this technology has the advantage to be spectrally flexible by band-gap engineering, further scaling of the peak power is challenging due to a strong trade-off between shorter pulse duration and higher average power and efficiency [25].

Solid-state laser oscillators have also already demonstrated high average power and ultrashort pulse durations at gigahertz repetition rate. Here, the broad gain bandwidth of Ti:sapphire is beneficial for the generation of extremely short pulses and allows for high peak power. For instance, an octave-spanning optical spectrum supporting sub-6-fs pulses at 1 GHz repetition rate was reported from a Kerr lens mode-locked (KLM) Ti:sapphire laser oscillator in [26]. Up to date, the shortest pulse duration at GHz repetition rate of 12 fs at an average output power of 1.2 W was reported in [27], which results in 88 kW of peak power assuming transform-limited soliton pulses [Fig. 1(b)]. However, although cost-effective and efficient diode-pumping has started to be developed [28–30], standard Ti:sapphire lasers still typically rely on more complex and expensive green pump lasers. Additionally, Ti:sapphire features a high quantum defect which can lead to significant thermal effects and limits the average power. So far, a maximum average power of 1.2 W was achieved at GHz repetition rates [Fig. 1(a)].

The development of ultrafast Yb-based diode-pumped solid-state lasers (Yb-DPSSLs) overcame these limitations. In the last decade, semiconductor saturable absorber mirror (SESAM) mode-locked Yb-DPSSL oscillators achieved both high average and peak power at gigahertz repetition rate [31–36]. One remarkable result has been the development of a SESAM mode-locked Yb:CALGO laser oscillator delivering 4.6 W of average output power in 96-fs pulses at 1.1 GHz repetition rate, leading to a peak power of 38 kW [37].

In comparison, KLM Yb-DPSSL oscillators offer the potential for even higher peak powers at GHz repetition rates. Although KLM laser oscillators usually require a more astute cavity design than SESAM mode-locked ones, they typically achieve shorter pulse durations and do not require

special solutions to overcome Q-switched mode-locking instabilities [36]. Very recently, 145-fs pulses with 1.7 W of average power and 4.8 kW of peak power at 2.16 GHz repetition rate and 17% optical-to-optical efficiency were demonstrated by a KLM Yb:KGW laser oscillator [38]. This is the first KLM Yb-based laser oscillator capable of exceeding the watt-level of average power and the kilowatt-level of peak power at a gigahertz repetition rate. However, this source applied soft-aperture Kerr-lens mode-locking and relied on a complex and expensive single-mode fiber-laser pump system.

In this article, we present two configurations of a directly diode-pumped KLM bulk laser oscillator based on the Yb:CALGO gain material delivering high average output power combined with short pulse duration at ~ 1 GHz repetition rate. Careful optimization of the cavity components and the mode-locking parameters enabled us to generate 93-fs pulses at 6.9 W of average power and 64 kW of peak power in a first configuration (config. 1) and sub-50-fs pulses at 4.1 W of average power with 74 kW of peak power in a second configuration (config. 2).

2. Experimental setup

The experimental setup is shown in Fig. 2. The laser oscillator is based on a 3-mm-long *a*-cut anti-reflection (AR) coated Yb(3 at.%):CALGO crystal. Yb:CALGO is a gain material that combines a flat and broadband emission cross-section [39] with low quantum defect allowing for the generation of sub-100-fs pulses at high efficiency and high average power [11,12,14,40]. Additionally, its nonlinear refractive index of $\sim 9 \times 10^{-20}$ m²/W is high enough for direct use as Kerr medium. The crystal is wrapped in indium foil and mounted in a water-cooled copper holder. It is optically pumped at a wavelength of 980 nm by a commercially available 20-W multimode fiber-coupled laser diode (0.15 NA and 105 μ m core diameter resulting in a beam quality factor $M^2 \approx 25$) from BWT Beijing Ltd. The crystal is placed such that its *c*-axis, which features the highest absorption cross-section [39], is aligned with the p-polarization of the pump.

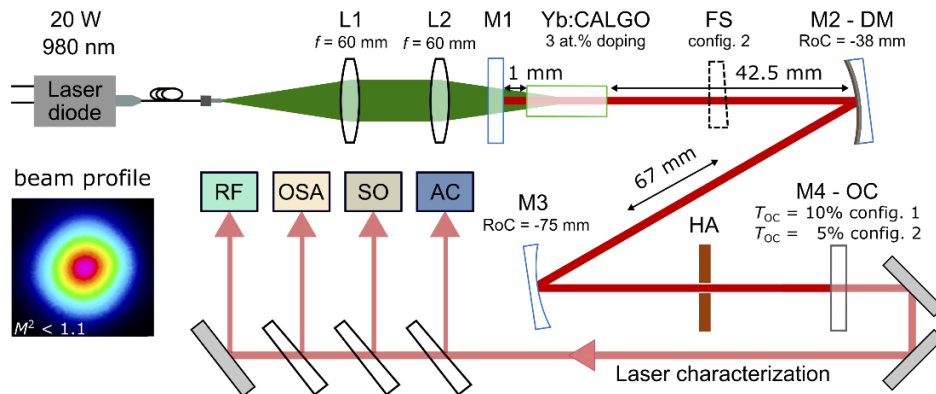


Fig. 2. Experimental setup of the laser oscillator for both configurations (config. 1 and config. 2). The inset shows the beam profile of the laser output in mode-locked operation for config. 2. L1, L2: lenses; M1-M4: cavity mirrors, HA: 1-mm diameter hard aperture; FS: AR-coated 3-mm thick fused-silica plate used in config. 2; DM: dispersive mirror; OC: output coupler with the transmission (T_{OC}) for each configuration; AC: autocorrelator; SO: sampling oscilloscope; OSA: optical spectrum analyser; RF: radio-frequency analyser. Cavity lengths for config. 1 are indicated by the black arrows and labelled respectively. In config. 2, the length Yb:CALGO-M2 was adjusted accordingly to compensate for the added fused silica plate. The repetition rate is adjusted to ~ 1 GHz by freely tuning the distance M3-M4.

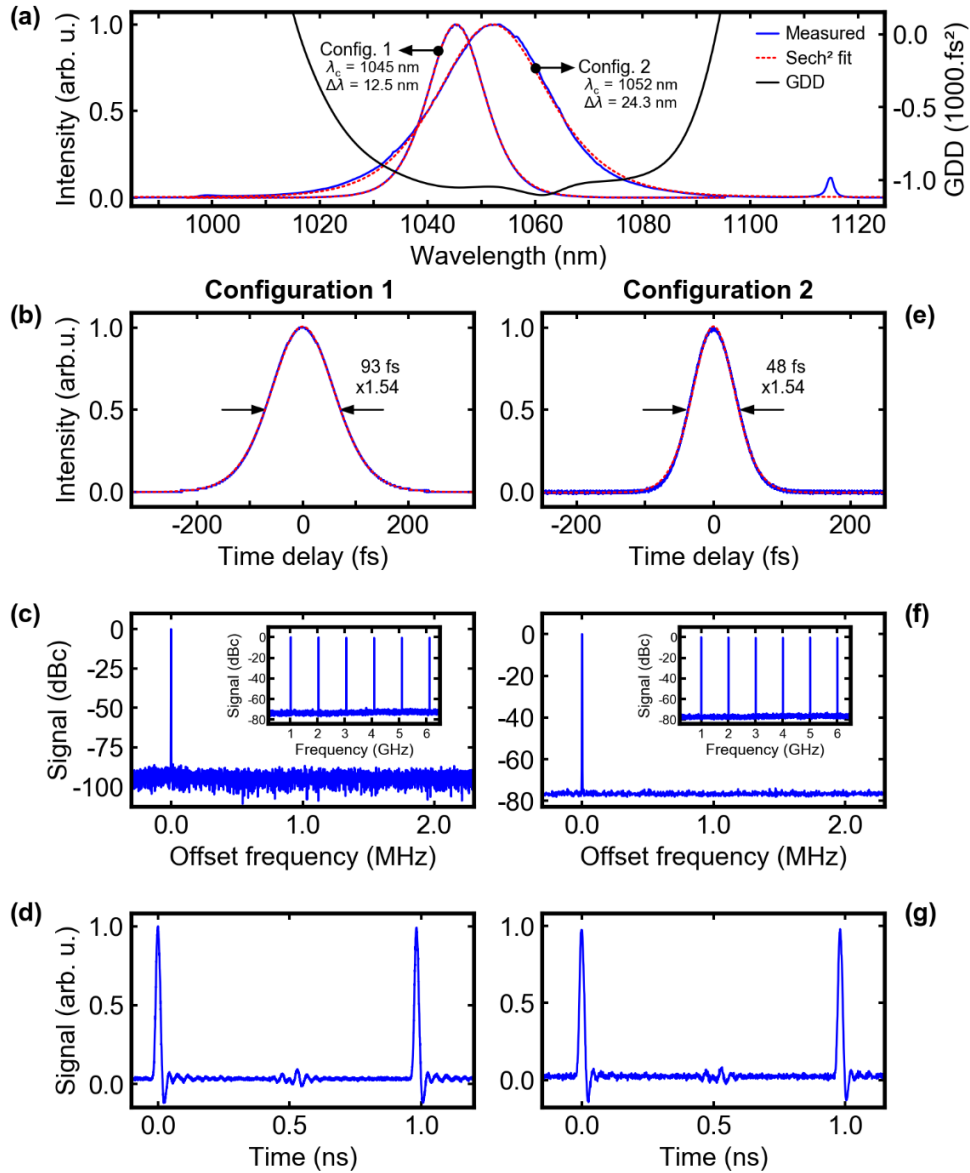


Fig. 3. (a) Measured optical spectrum (blue) with sech^2 fit (red) for soliton pulses and round-trip group delay dispersion (GDD) introduced by the mirrors M1, M2 and M3 (black) for both configurations. (b), (e) Intensity autocorrelation trace (blue) of the pulse and its sech^2 fit (red). (c), (f) Radio-frequency (RF) spectrum of the laser fundamental repetition rate $f_{\text{rep}} \approx 1$ GHz measured with 300-Hz resolution bandwidth (RBW). Inset: RF spectrum of the higher repetition rate harmonics measured with 10-kHz RBW. (d), (g) Sampling oscilloscope trace (the ringing in the signal trace at 0.5 ns is attributed to the electronics of the detection setup). λ_c : central laser wavelength; $\Delta\lambda$: full width at half maximum spectral bandwidth.

Accordingly, one maximizes the portion of pump power in the p-polarization by bending the pump delivery fiber, which results in a ratio of 80%/20% of p-polarization/s-polarization. The total output power is used to pump the crystal. The central pump wavelength is adjusted to the 980-nm absorption peak of the Yb:CALGO by maintaining the diode at a temperature of 38 °C using a Peltier element. The pump beam is collimated by a 60-mm focal length aspherical lens and subsequently focused into the crystal with another identical lens. In this configuration, the pump beam radius of the focus at the position of the gain crystal was measured to be 65 μm ($1/e^2$) which was experimentally optimized for achieving stable KLM operation at highest power levels and highest optical-to-optical efficiency. We estimate the laser beam radius in the crystal to be around 70 μm in CW and up to 75 μm in KLM operation ($1/e^2$) based on a formalism of ray transfer matrices for Gaussian beams. The laser oscillator is based on a ~ 150 -mm-long standing-wave cavity composed of 4 mirrors resulting in ~ 1 GHz repetition rate. As shown in Fig. 2, the gain medium is pumped through a flat dichroic mirror M1, which is highly reflective (HR) for the laser wavelengths above 1000 nm and highly transmissive for the pump wavelength around 980 nm. The second (M2) and third (M3) mirror are concave with a radius of curvature of -38 mm and -75 mm, respectively. The last mirror is a plane output coupler (OC) with a transmission $T_{\text{OC}} = 10\%$ for config. 1 and $T_{\text{OC}} = 5\%$ for config. 2. For achieving a stable KLM operation and a high beam quality, a hard aperture constituted of an uncooled copper plate with a 1.0-mm diameter hole is inserted between M3 and OC where the laser beam is collimated. The phase shift arising from self-phase modulation and the positive group delay dispersion (GDD) in the gain crystal is balanced by the dispersive mirror (DM) M2 which provides -500 fs^2 per bounce between 1020 nm and 1080 nm. In config. 2 optimized for shortest pulse duration, an AR-coated 3-mm-thick wedged fused-silica plate introducing a round-trip GDD of $\sim 100 \text{ fs}^2$ is inserted inside the cavity. The dispersive coating on M2 and the AR coating on both faces of the fused-silica plate were designed and grown in our own ion beam sputtering coating facility. The total round-trip GDD introduced by the gain medium, the DM and the fused-silica plate (for config. 2) at the wavelength of 1050 nm is estimated to be -400 fs^2 for config. 1 and -300 fs^2 for config. 2. The introduced GDD of M1, M2, and M3 per cavity round-trip is shown in Fig. 3(a). Both cavity configurations differ only in the out-coupling rate, the round-trip GDD, and the adjusted pump power.

3. Experimental results

The system is operated in two configurations optimized for either highest average power or shortest pulse duration. Operation in the KLM regime is initiated by gently pushing the output coupler which is mounted on a translation stage. The experimental results for each configuration are discussed below and summarized in Table 1.

Table 1. Laser parameters of the KLM Yb:CALGO laser oscillator generating pulses at 1 GHz repetition rate for config. 1 (highest average power) and config. 2 (shortest pulse duration).^a

Config.	T_{OC} (%)	GDD_{tot} (fs^2)	f_{rep} (GHz)	P_{pump} (W)	P_{ave} (W)	τ (fs)	λ_c (nm)	$\Delta\lambda$ (nm)	E_p (nJ)	P_{peak} (kW)	η_{eff} (%)
1	10	-400	1.02	18.5	6.9	93	1045	12.5	6.8	64	37
2	5	-300	1.00	19.5	4.1	48	1052	24.3	4.1	74	21

^a T_{OC} : output coupling rate; GDD_{tot} : estimated total round-trip group delay dispersion; f_{rep} : repetition rate; P_{pump} : diode pump power; P_{ave} : average output power; τ : full width at half maximum (FWHM) pulse duration; λ_c : laser central wavelength; $\Delta\lambda$: FWHM spectral bandwidth; E_p : pulse energy; P_{peak} : peak power; η_{eff} : optical-to-optical efficiency.

In config. 1 optimized for the highest average power, the oscillator is operated with a 10% output coupling rate and the total round-trip GDD is approximately -400 fs^2 . Using 18.5 W of pump power, the oscillator generates 93-fs pulses [Fig. 3(b)] at 6.9 W of average output power and

1.0 GHz repetition rate. This results in an optical-to-optical efficiency of 37% with respect to the pump power, a peak power of 64 kW, and 6.8 nJ of pulse energy. The optical spectrum is centered at 1045 nm and has a full width at half maximum (FWHM) bandwidth of 12.5 nm [Fig. 3(a)]. The least-square-based fit for sech^2 -pulses drawn on top of the optical spectrum (sech^2 in frequency domain) and the autocorrelation trace show a very good agreement with the expected soliton regime. Additionally, the resulting time-bandwidth product of 0.320 indicates the generation of transform-limited soliton pulses. The short-term stability of the mode-locked regime is proven by the radio-frequency spectrum [Fig. 3(c)]. The single pulse regime is confirmed by observing the pulse train using a 40 GHz sampling oscilloscope with an 18.5-ps rise time photodetector [Fig. 3(d)].

In config. 2 optimized for shortest pulse duration and highest peak power, the output coupling rate was reduced to 5% and the cavity GDD adjusted to approximately -300 fs^2 per cavity round-trip by inserting an AR-coated 3-mm-thick fused-silica plate (dashed component in Fig. 2). Using 19.5 W of pump power, the oscillator generates pulses as short as 48 fs at 4.1 W of average output power. The laser beam profile is a clean TEM_{00} Gaussian mode [inset of Fig. 2] with a beam quality factor $M^2 < 1.1$. Although the pulse energy decreased to 4.1 nJ, the peak power increased to 74 kW due to the shorter pulse duration, which is the highest peak power so far demonstrated by an Yb-based GHz-class laser oscillator. Similar to config. 1, we measured the optical spectrum, intensity autocorrelation trace, radio-frequency spectrum and confirmed single pulse operation [Fig. 3(a,e-g)]. The FWHM spectral bandwidth increased to 24.3 nm while the central wavelength at 1052 nm shifted by 7 nm towards the longer wavelength side which is expected for an Yb:CALGO laser operating at a lower resonator loss [40]. The sech^2 -fit of the optical spectrum and the autocorrelation trace indicate a clean soliton mode-locking regime. However, it is worth noting the presence of a slight pedestal and dispersive wave on the blue and red side of the optical spectrum, respectively. In this configuration, the spectral bandwidth expands much larger and the observed features can be attributed to a strong variation of the introduced GDD below 1010 nm and above 1100 nm [Fig. 3(a)]. It is expected that these features will limit a further spectral expansion for the efficient generation of even shorter pulses and, respectively, reaching higher peak powers. We expect that shorter pulses and corresponding higher peak powers are within reach by further improving the intracavity GDD for a broader flat spectral coverage and applying for instance the broadband cross-polarized pumping scheme developed in our group [40]. In both configurations, once mode-locking was initiated it remained stable over several hours.

4. Conclusion

We demonstrated a directly diode-pumped KLM Yb:CALGO bulk laser oscillator allowing for high average power (config. 1) and short pulses (config. 2) at GHz repetition rates. Using 18.5 W of diode pump power, we demonstrated 6.9 W of average power in a first configuration. By decreasing the net GDD of the cavity and the output coupler transmission, the oscillator generated pulses as short as 48 fs at 4.1 W in a second configuration. This system demonstrates the shortest pulse duration, highest average power and peak power with respect to previous GHz-class Yb-based laser oscillators.

We believe shorter pulse durations are within reach of the technology as sub-30-fs pulse durations at high average power have already been demonstrated for Yb:CALGO at MHz repetition rates [40]. Improving the dispersion management in the cavity will resolve the current limitation regarding the pulse duration and should allow for a further increase in peak power. The system shows a good long-term stability by operating for several hours without neither interruption of the mode-locking nor considerable degradation of the output performance.

This simple, compact and low-cost Yb-DPSSL oscillator competes with current cutting-edge GHz-class laser sources and is attractive for industrial applications benefitting clean soliton pulses with high peak powers at GHz repetition rates.

Funding. Schweizerischer Nationalfonds zur Förderung der Wissenschaftlichen Forschung (200020_179146, 200021_188456, 200021_200774); Spark (CRSK-2_190593); R'Equip (206021_144970, 206021_198176).

Disclosures. The authors declare no conflicts of interest.

Data availability. Data underlying the results presented in this paper are available in Ref. [41]

References

1. S. A. Diddams, "The evolving optical frequency comb [Invited]," *J. Opt. Soc. Am. B* **27**(11), B51–B62 (2010).
2. M. Maiuri, M. Garavelli, and G. Cerullo, "Ultrafast Spectroscopy: State of the Art and Open Challenges," *J. Am. Chem. Soc.* **142**(1), 3–15 (2020).
3. S.-W. Chu, T.-M. Liu, C.-K. Sun, C.-Y. Lin, and H.-J. Tsai, "Real-time second-harmonic-generation microscopy based on a 2-GHz repetition rate Ti:sapphire laser," *Opt. Express* **11**(8), 933–938 (2003).
4. F. F. Voigt, F. Emaury, P. Bethge, D. Waldburger, S. M. Link, S. Carta, A. van der Bourg, F. Helmchen, and U. Keller, "Multiphoton in vivo imaging with a femtosecond semiconductor disk laser," *Biomed. Opt. Express* **8**(7), 3213–3231 (2017).
5. K. J. Mohler, B. J. Bohn, M. Yan, G. Mélen, T. W. Hänsch, and N. Picqué, "Dual-comb coherent Raman spectroscopy with lasers of 1-GHz pulse repetition frequency," *Opt. Lett.* **42**(2), 318–321 (2017).
6. P. J. Mosley, J. S. Lundeen, B. J. Smith, P. Wasylczyk, A. B. U'Ren, C. Silberhorn, and I. A. Walmsley, "Heralded Generation of Ultrafast Single Photons in Pure Quantum States," *Phys. Rev. Lett.* **100**(13), 133601 (2008).
7. T. Kroker, M. Großmann, K. Sengstock, M. Drescher, P. Wessels-Staarmann, and J. Simonet, "Ultrafast electron cooling in an expanding ultracold plasma," *Nat. Commun.* **12**(1), 596 (2021).
8. A. Anwar, C. Perumangatt, F. Steinlechner, T. Jennewein, and A. Ling, "Entangled photon-pair sources based on three-wave mixing in bulk crystals," *Rev. Sci. Instrum.* **92**(4), 041101 (2021).
9. R.-B. Jin, R. Shimizu, I. Morohashi, K. Wakui, M. Takeoka, S. Izumi, T. Sakamoto, M. Fujiwara, T. Yamashita, S. Miki, H. Terai, Z. Wang, and M. Sasaki, "Efficient generation of twin photons at telecom wavelengths with 2.5 GHz repetition-rate-tunable comb laser," *Sci. Rep.* **4**(1), 7468 (2015).
10. A. M. Kowalevich Jr., A. T. Zare, F. X. Kärtner, J. G. Fujimoto, S. Dewald, U. Morgner, V. Scheuer, and G. Angelow, "Generation of 150-nJ pulses from a multiple-pass cavity Kerr-lens mode-locked Ti:Al₂O₃ oscillator," *Opt. Lett.* **28**(17), 1597–1599 (2003).
11. A. Greborio, A. Guandalini, and J. Aus der Au, "Sub-100 fs pulses with 12.5-W from Yb:CALGO based oscillators," *Proc. SPIE* **8235**, 823511 (2012).
12. P. Sévillano, P. Georges, F. Druon, D. Descamps, and E. Cormier, "32-fs Kerr-lens mode-locked Yb:CaGdAlO₄ oscillator optically pumped by a bright fiber laser," *Opt. Lett.* **39**(20), 6001–6004 (2014).
13. R. Akbari and A. Major, "High-power diode-pumped Kerr-lens mode-locked bulk Yb:KGW laser," *Appl. Opt.* **56**(31), 8838–8844 (2017).
14. S. Manjooran and A. Major, "Diode-pumped 45 fs Yb:CALGO laser oscillator with 1.7 MW of peak power," *Opt. Lett.* **43**(10), 2324–2327 (2018).
15. R. Akbari and A. Major, "Kerr-lens mode locking of a diode-pumped Yb:KGW laser using an additional intracavity Kerr medium," *Laser Phys. Lett.* **15**(8), 085001 (2018).
16. W. Tian, R. Xu, L. Zheng, X. Tian, D. Zhang, X. Xu, J. Zhu, J. Xu, and Z. Wei, "10-W-scale Kerr-lens mode-locked Yb:CALYO laser with sub-100-fs pulses," *Opt. Lett.* **46**(6), 1297–1300 (2021).
17. J. J. McFerran, L. Nenadović, W. C. Swann, J. B. Schlager, and N. R. Newbury, "A passively mode-locked fiber laser at 1.54 μm with a fundamental repetition frequency reaching 2 GHz," *Opt. Express* **15**(20), 13155–13166 (2007).
18. H.-W. Chen, G. Chang, S. Xu, Z. Yang, and F. X. Kärtner, "3 GHz, fundamentally mode-locked, femtosecond Yb-fiber laser," *Opt. Lett.* **37**(17), 3522–3524 (2012).
19. A. Martinez and S. Yamashita, "10 GHz fundamental mode fiber laser using a graphene saturable absorber," *Appl. Phys. Lett.* **101**(4), 041118 (2012).
20. C. Li, Y. Ma, X. Gao, F. Niu, T. Jiang, A. Wang, and Z. Zhang, "1 GHz repetition rate femtosecond Yb: fiber laser for direct generation of carrier-envelope offset frequency," *Appl. Opt.* **54**(28), 8350–8353 (2015).
21. D. Chao, M. Y. Sander, G. Chang, J. L. Morse, J. A. Cox, G. S. Petrich, L. A. Kolodziejcki, F. X. Kärtner, and E. P. Ippen, "Self-referenced Erbium Fiber Laser Frequency Comb at a GHz Repetition Rate," in *Optical Fiber Communication Conference* (Optical Society of America, 2012), paper OW1C.2.
22. X. Chen, W. Lin, W. Wang, X. Guan, X. Wen, T. Qiao, X. Wei, and Z. Yang, "High-power femtosecond all-fiber laser system at 1.5 μm with a fundamental repetition rate of 4.9 GHz," *Opt. Lett.* **46**(8), 1872–1875 (2021).
23. Y. Wang, Y. Liu, Z. Zhang, and F. Kaertner, "Amplification of 1.08 GHz repetition rate femtosecond laser pulses to 97 W average power by a fiber amplifier," *OSA Continuum* **4**(5), 1571–1576 (2021).
24. K. G. Wilcox, A. C. Tropper, H. E. Beere, D. A. Ritchie, B. Kunert, B. Heinen, and W. Stolz, "4.35 kW peak power femtosecond pulse mode-locked VECSEL for supercontinuum generation," *Opt. Express* **21**(2), 1599–1605 (2013).

25. C. G. E. Alfieri, D. Waldburger, S. M. Link, E. Gini, M. Golling, G. Eisenstein, and U. Keller, "Optical efficiency and gain dynamics of modelocked semiconductor disk lasers," *Opt. Express* **25**(6), 6402–6420 (2017).
26. T. M. Fortier, A. Bartels, and S. A. Diddams, "Octave-spanning Ti:sapphire laser with a repetition rate >1 GHz for optical frequency measurements and comparisons," *Opt. Lett.* **31**(7), 1011–1013 (2006).
27. A. Bartels and H. Kurz, "Generation of a broadband continuum by a Ti: sapphire femtosecond oscillator with a 1-GHz repetition rate," *Opt. Lett.* **27**(20), 1839–1841 (2002).
28. P. W. Roth, A. J. Maclean, D. Burns, and A. J. Kemp, "Directly diode-laser-pumped Ti:sapphire laser," *Opt. Lett.* **34**(21), 3334–3336 (2009).
29. K. Gürel, V. J. Wittwer, M. Hoffmann, C. J. Saraceno, S. Hakobyan, B. Resan, A. Rohrbacher, K. Weingarten, S. Schilt, and T. Südmeyer, "Green-diode-pumped femtosecond Ti:Sapphire laser with up to 450 mW average power," *Opt. Express* **23**(23), 30043–30048 (2015).
30. S. Backus, M. Kirchner, C. Durfee, M. Murnane, and H. Kapteyn, "Direct diode-pumped Kerr Lens 13 fs Ti:sapphire ultrafast oscillator using a single blue laser diode," *Opt. Express* **25**(11), 12469–12477 (2017).
31. S. Pekarek, C. Fiebig, M. C. Stumpf, A. E. H. Oehler, K. Paschke, G. Erbert, T. Südmeyer, and U. Keller, "Diode-pumped gigahertz femtosecond Yb:KGW laser with a peak power of 3.9 kW," *Opt. Express* **18**(16), 16320–16326 (2010).
32. S. Pekarek, T. Südmeyer, S. Lecomte, S. Kundermann, J. M. Dudley, and U. Keller, "Self-referenceable frequency comb from a gigahertz diode-pumped solid-state laser," *Opt. Express* **19**(17), 16491–16497 (2011).
33. A. Klenner, M. Golling, and U. Keller, "A gigahertz multimode-diode-pumped Yb:KGW enables a strong frequency comb offset beat signal," *Opt. Express* **21**(8), 10351–10357 (2013).
34. A. Klenner, M. Golling, and U. Keller, "High peak power gigahertz Yb:CALGO laser," *Opt. Express* **22**(10), 11884–11891 (2014).
35. A. Klenner and U. Keller, "All-optical Q-switching limiter for high-power gigahertz modelocked diode-pumped solid-state lasers," *Opt. Express* **23**(7), 8532–8544 (2015).
36. L. M. Krüger, A. S. Mayer, Y. Okawachi, X. Ji, A. Klenner, A. R. Johnson, C. Langrock, M. M. Fejer, M. Lipson, A. L. Gaeta, V. J. Wittwer, T. Südmeyer, C. R. Phillips, and U. Keller, "Performance scaling of a 10-GHz solid-state laser enabling self-referenced CEO frequency detection without amplification," *Opt. Express* **28**(9), 12755–12770 (2020).
37. A. Klenner, M. Golling, and U. Keller, "Compact gigahertz frequency combs," in *Advanced Solid-State Lasers Congress* (Optical Society of America, 2013), paper ATH3A.1.
38. L. Zheng, W. Tian, H. Liu, G. Wang, C. Bai, R. Xu, D. Zhang, H. Han, J. Zhu, and Z. Wei, "2-GHz watt-level Kerr-lens mode-locked Yb:KGW laser," *Opt. Express* **29**(9), 12950–12957 (2021).
39. K. Hasse, T. Calmano, B. Deppe, C. Liebald, and C. Kränkel, "Efficient Yb³⁺:CaGdAlO₄ bulk and femtosecond-laser-written waveguide lasers," *Opt. Lett.* **40**(15), 3552–3555 (2015).
40. F. Labaye, V. J. Wittwer, M. Hamrouni, N. Modsching, E. Cormier, E. Cormier, and T. Südmeyer, "Efficient few-cycle Yb-doped laser oscillator with Watt-level average power," *Opt. Express* **30**(2), 2528–2538 (2022).
41. M. Hamrouni, F. Labaye, N. Modsching, V. J. Wittwer, and T. Südmeyer, Data for "Efficient high-power sub-50-fs gigahertz repetition rate diode-pumped solid-state laser," EUDAT B2SHARE repository (2022), <https://b2share.eudat.eu/records/664840fae08240978cef3bc9833f5fc7>.

2.2 Powerful 1- μm 1-GHz optical frequency comb

As previously explained, OFCs with GHz comb spacing are of high interest for many applications, notably in spectroscopy, metrology and telecommunication. In the last section, we discussed the development of a powerful and broadband laser oscillator operating at 1-GHz repetition rate. Nearly all OFC-based applications require high stability levels that are not achieved in free-running operation. As a preliminary step toward realizing a low-noise OFC source, we engineered a more robust and stable version of the initial laser. In this new design, the cavity components are glued into a thick aluminum housing, allowing better cooling and enhanced mechanical stability with similar pulse duration and power levels (see section 2.2.2). In the following article, we describe the full stabilization of the all-glued version of the laser.

2.2.1 Article outline

Context

This work is the continuation of the previous article. Among the Yb-based lasers presented in the literature review of the last article [17], only few of them achieved the stabilization of the oscillator [6, 18]. Moreover, these stabilized sources were based on SESAM mode-locking. Thus, prior to this work, full stabilization of a self-referenced Yb-based KLM laser oscillator operating at the gigahertz level had never been reported. Although there is no inherent limitation for stabilizing such sources, the combination of multi-mode diode pumping and Kerr-lens mode-locking is considered unsuitable for low-noise operation. Single-mode pumping is generally favored over multi-mode pumping for low-noise operation to avoid the fluctuations induced by the mode competition occurring in multi-mode fibers. Furthermore, KLM lasers often require operating close to the edge of the cavity stability zone, which is more sensitive to fluctuations. In this work, however, we achieve the first stabilization of a multi-mode-pumped Kerr-lens mode-locked laser oscillator and demonstrate noise performance comparable to state-of-the-art sources.

Key results

We first characterize the long-term stability of the laser in the free-running regime. We show that the average power and repetition rate feature only minor fluctuations over a long measurement time of 16 hours. Second, we address the impact of temperature variations on the laser performance. The mode-locking regime is maintained across a broad temperature range of 30°C, which is remarkable for KLM laser oscillators that are often deemed highly sensitive

to environmental changes.

We subsequently stabilize and characterize the repetition rate and carrier-envelope offset frequency. The f_{CEO} detection was achieved by conventional f-to-2f interferometry. The supercontinuum used for self-referencing is generated inside a photonic crystal fiber with only 20% of the available output power, leaving a high average power of 2.7 W for applications. The timing jitter, which derives from the noise of the repetition rate, reduces from 140 ps in the free-running state to <150 fs post-stabilization, across a measurement range of 1Hz–10MHz. We subsequently assess the f_{CEO} noise. After stabilization, the overall f_{CEO} phase noise integrated between 1Hz–10MHz amounts to 107 mrad, limited by the servo loop and the detection noise floor. Remarkably, the residual noise lies well below the beta separation line at all frequencies, indicating negligible influence of the f_{CEO} on the comb tooth linewidth [19].

Comparison to state-of-the-art optical frequency combs

To put our results in perspective, we compare the noise performance of the stabilized source against a selection of leading low-noise OFCs based on bulk gain materials. Considering the large number of reported results, our discussion focuses on a selection of state-of-the-art OFC sources, including SESAM mode-locked oscillators (i), single-mode-pumped KLM lasers (ii), and erbium-ytterbium-glass laser sources (iii). Comparisons (i) and (ii) are motivated by the fact that multi-mode pumping and Kerr-lens mode-locking are generally considered as not appropriate for low-noise operation. We also compare to (iii) since the erbium-ytterbium-glass gain material is commonly used to realize low-noise OFCs. Its material structure leads to a low-pass filtering effect that dampens the pump fluctuations, reducing the impact of the pump on the laser noise [20]. The results of this study are summarized in Table 1 in the article. Overall, our laser demonstrates superior noise performance compared to most of the sources we evaluated. It is noteworthy that only the sources utilizing Er:Yb:glass gain materials reported better f_{rep} noise, which is likely due to the fact they achieve the locking in the optical domain.

Conclusion

In summary, we demonstrate an OFC delivering 2.7 W of average power with sub-50-fs pulses at 1-GHz of repetition rate. The combination of low-noise operation with high-power levels and long-term stability is particularly remarkable. Furthermore, considering the simplicity and cost-effectiveness of the overall system, these achievements mark significant advancements in the development of powerful OFC sources. We underline two main avenues for further improving the system. First, shorter pulse durations can be obtained by better manage-

ment of the dispersion inside the cavity. On the other side, higher stability will be achieved by improving the cavity housing and cooling, and by upgrading the stabilization setup. For example, using an optical reference rather than a radio-frequency one for stabilizing the repetition frequency should allow much lower noise levels.

2.2.2 Further discussion

Comment about noise comparison between systems

In the article, we compared the noise properties of our stabilized laser oscillator with other state-of-the-art low-noise OFC sources. This comparison specifically focused on the timing jitter and integrated f_{CEO} phase noise, which are common metrics to assess the noise performance. However, since these parameters do not provide sufficient insights about the dynamics of the noise within the systems, it is difficult to definitively ascertain why one source may perform better or worse than another. For instance, in the article we show that our stabilized laser has better noise performances than many other state-of-the-art OFCs that are typically regarded, element-wise, as better suited for low-noise operation. In many cases, optimizing the noise performance largely resides on meticulous engineering of both the laser and its stabilization system.

Looking ahead, it would be interesting to experimentally investigate how design parameters such as the mode-locking technique (KLM or SESAM) or type of the pump (single-mode versus multi-mode) impact the noise level. However, performing comprehensive analysis about the noise dynamics is complex due to the multitude of influencing factors and their interdependencies [21], which requires careful engineering of the laser.

All-glued version of the GHz laser oscillator

To improve the robustness and stability of the laser described in Section 2.1, we developed two upgraded versions of the cavity. In the second version, the cavity components were bonded onto an aluminum base plate (Fig. 2.1). To allow enough degrees of freedom in the cavity alignment, the mirrors are first preliminarily attached from the top on rigid poles that hold the components a few millimeters above the base plate. Once the alignment is finished, the mirrors are connected to the aluminum plate via tiny pieces of glass that are both glued to the plate and the mirrors. In the second version, all the laser assembly, except the pump diode and its delivery fiber, is glued to the aluminum plate. In the third version, the design is further extended by fully bonding the laser assembly into a monolithic aluminum box (Fig. 2.1). This way, the laser is fully isolated from air fluctuations and dust particles. As a result, this design significantly

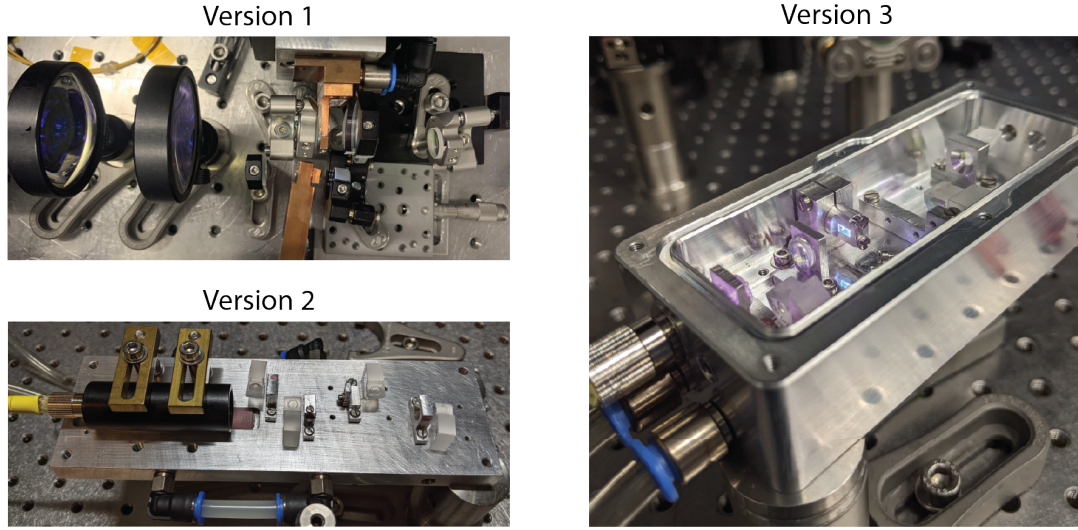


Figure 2.1: Pictures of the three versions of the laser setup. Version 1: The laser cavity is constructed with regular optomechanics clamped on the optical table. Version 2: The components of the cavity are glued onto an aluminum plate. Version 3: All the laser assembly is bonded inside a monolithic aluminum box, sealed to reduce external perturbations.

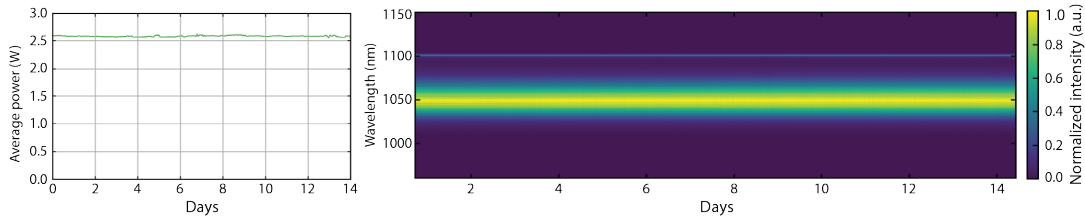


Figure 2.2: Average power (a) and spectrum (b) of the laser logged for 14 days.

improves the mechanical stability and greatly facilitates heat extraction, which is crucial for high-power operation.

To characterize the long-term stability of the all-glued version, we monitored the average power and output spectrum during 14 days without interruption. Unlike the version discussed in the article that showed performance degradation after several hours, this pseudo-monolithic laser maintained its performances for 14 consecutive days (Fig. 2.2). The presence of small fluctuations in the average power are likely due to variations of the room temperature.

To characterize the advantage of the all-glued design with respect to noise performance, we compare the phase noise of the repetition frequency before and after the cavity components are glued into the aluminum housing. The results are shown figure 2.3. Between 0-10 Hz, the power spectral densities feature similar levels for the two configurations. Between 10 Hz-2.5 kHz, the noise level

2.2. Powerful 1- μm 1-GHz optical frequency comb

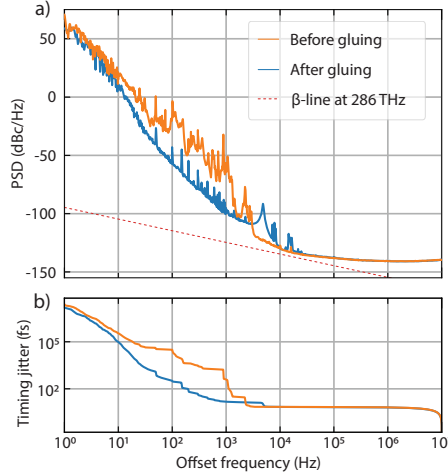


Figure 2.3: Phase noise power spectral density of the repetition frequency (a) and the corresponding integrated jitter (b) for the configuration before gluing (orange curve) and after gluing (blue curve).

of the all-glued version lies significantly below the one obtained before gluing. In this region, the corresponding integrated timing jitter is up to two orders of magnitude lower. As expected, gluing the components into a thick aluminum housing reduces the mechanical vibrations. The peaks that remain after gluing coincide with the harmonics of the electrical power grid frequency (50 Hz) that couple into the system via the driving electronics. We note the presence of a bump around 5 kHz in the after-gluing power spectral density. It may be due to a mechanical resonance of the overall aluminum housing that is transmitted to the mirrors, and can be suppressed by better isolating the housing from the optical table. For frequencies higher than 100 kHz, the detection is limited by the shot noise.

To summarize, the pseudo-monolithic version not only features better long-term stability but also achieves, for nearly all frequencies, much lower noise levels than the first prototype version. In general, starting with lower noise levels is beneficial for subsequent stabilization since the requirements on the stabilization system reduce accordingly.

2.2.3 Acknowledgment

I would like to acknowledge Michael Müller, whose major contributions have been instrumental in achieving the excellent results showcased in this section.



Powerful 1- μm 1-GHz optical frequency comb

MICHAEL MÜLLER,^{*}  MARIN HAMROUNI, 
KENICHI N. KOMAGATA,  ALEXANDRE PARRIAUX, 
VALENTIN J. WITTEW,  AND THOMAS SÜDMEYER 

Laboratoire Temps-Fréquence, Institut de Physique, Université de Neuchâtel, Avenue de Bellevaux 51, 2000 Neuchâtel, Switzerland

^{*}michael.mueller@unine.ch

Abstract: A self-referenced optical frequency comb is presented based on Kerr-lens mode-locking of ytterbium-doped CALGO. The robust source delivers 3.5 W average power in 44 fs-long pulses at 1 GHz repetition rate. The residual root-mean-square timing jitter of the emitted pulse-train is 146 fs and the residual integrated phase noise of the carrier-envelope offset frequency is 107 mrad, both in a span from 1 Hz to 10 MHz. After stabilization, 2.7 W average power remains for direct application. This work represents the first multi-mode pumped Kerr-lens mode-locked optical frequency comb at gigahertz-level repetition rate.

© 2023 Optica Publishing Group under the terms of the [Optica Open Access Publishing Agreement](#)

1. Introduction

Optical frequency combs (OFC) are spectra of equally spaced optical lines that provide a coherent link between optical and radio frequency domain. They are powerful tools for spectroscopy and metrology and find application for example in optical atomic clocks, quantum computers, astrophysics, navigation, and ranging. OFCs have been realized in many platforms, e.g. mode-locked fiber, solid-state, and quantum-cascade lasers, and even starting from continuous wave lasers by using electro-optical modulation or micro-resonators. [1–4]

The ideal comb line spacing ranges from several tens of megahertz up to hundreds of gigahertz depending on the application. A repetition rate (or line spacing) around 1 GHz is particularly versatile. It permits high-speed acquisition in three-dimensional imaging [5] and in dual-comb spectroscopy [6,7] while allowing simple interfacing with electronics. Further, the power per comb line is larger compared to lower repetition rate sources, which improves the signal-to-noise ratio for locking to optical transitions.

Gigahertz-repetition-rate OFCs have been built in fiber or free-space geometry based on titanium [8,9], ytterbium [10], erbium [11] and chromium [12] gain media with their emission bands at around 800 nm, 1 μm , 1.5 μm and 2.4 μm . Spectral gaps are closed by nonlinear frequency conversion [13–16] or spectral broadening [17]. Multi-mode pumped ytterbium-doped bulk solid-state laser oscillators offer sufficient power to directly drive conversion processes, reducing cost and complexity compared to master-oscillator power amplifiers, while allowing control of the OFC with low-noise near-infrared detectors.

Among others, ytterbium-doped CALGO is an established gain medium for bulk solid-state lasers featuring a wide emission band and favorable thermal properties [18]. CALGO-based OFCs have been demonstrated already using semiconductor saturable absorber mirrors (SESAM) in both multi-mode [19,20] and single-mode pumping [21]. An alternative is Kerr-lens mode-locking (KLM). It facilitates the generation of shorter pulses and higher peak power [22], which is beneficial for subsequent conversion steps and for self-referencing via supercontinuum generation [23]. In turn, the typically required operation close to the cavity stability edge results in tighter alignment tolerances. Hence, a high mechanical stability is key for long-term stable operation of Kerr-lens mode-locked lasers [24].

In total, the combination of multi-mode pumped bulk solid-state lasers and the short-pulse generation potential of Kerr lens mode-locking appears a promising route to procure cheap yet powerful OFCs. This avenue is explored in the following by building a robust 1 GHz-repetition-rate ytterbium-doped Kerr-lens mode-locked CALGO laser. Transformation into an OFC is achieved by stabilizing the repetition rate and the carrier-envelope offset frequency to radio-frequency references. The results are compared to state-of-the-art sources.

2. Setup

A schematic of the setup is shown in Fig. 1 and consists of three major parts: A mode-locked laser similar to Ref. [22] and each one stabilization loop for the repetition rate and for the carrier-envelope offset frequency.

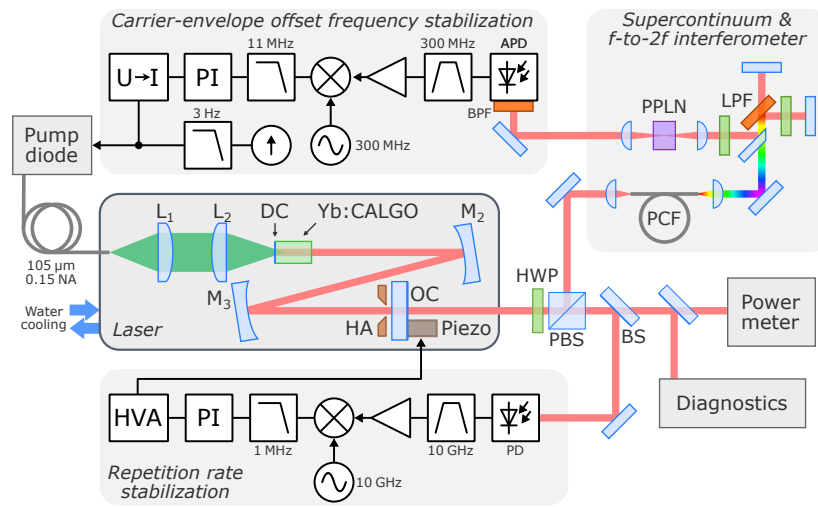


Fig. 1. Schematic of the full optical and electronic setup with a detailed description in the text. Abbreviations: L: lens, DC: dichroic, M: mirror, HA: hard aperture, OC: output coupler, HWP: half-wave plate, (P)BS: (polarizing) beam splitter, PCF: photonic crystal fiber, LPF: long-pass filter, BPF: band-pass filter, PPLN: periodically poled lithium niobate, (A)PD: (avalanche) photo diode, PI: proportional-integral controller, HVA: high-voltage amplifier.

The hard-aperture Kerr-lens mode-locked oscillator is based on a 4 mm-long Ytterbium-doped CALGO crystal with 2.5 at. % doping concentration. The crystal is end-pumped by a wavelength-stabilized diode laser emitting up to 20 W average power at 981 nm, whose light is delivered in a fiber with a core diameter of 105 μm and 0.15 numerical aperture. The fiber tip is reimaged into the gain medium using two spherical lenses of 15 mm focal length (L_1 , L_2). A standing-wave cavity is formed between the outer facet of the crystal, two concave mirrors (M_2 , M_3), and a flat output coupler (OC). The crystal facet is dichroically coated (DC) as short pass filter transmissive for the pump and reflective for the signal. The group delay dispersion (GDD) of the reflection has a value of $+200 \text{ fs}^2$ at 1050 nm wavelength. The mirror M_2 has a radius of curvature of 38 mm and a GDD of -250 fs^2 . The mirror M_3 has a 60 mm radius of curvature and a GDD of -500 fs^2 . The output coupler has a reflectivity of 95% and is mounted in reverse. The partially transmissive coating is outside while the 6.35 mm-long fused-silica substrate and the anti-reflection-coated backside are inside the cavity. This arrangement results in a net cavity round-trip dispersion of -300 fs^2 . The plane-plane optical elements, notably the gain medium and the output coupler, have a small wedge to avoid etalon effects. The output coupler is mounted on a piezo actuator

with 2 μm travel range for the later stabilization of the repetition rate. A hard aperture with 700 μm diameter is placed in front of the output coupler. The laser assembly, excluding the pump diode and its delivery fiber, is glued into a rigid and water-cooled aluminum housing with outer dimensions of $106 \times 46 \times 30 \text{ mm}^3$ for mechanical stability and heat extraction. There is no adjustable optical component left similar to Refs. [24,25]. The largest part of the output beam is sent to a power meter and beam diagnostics. The beam diagnostic comprises an optical and a radio-frequency spectrometer, an optical autocorrelator, and another fast photo diode feeding a phase noise analyzer (Rohde & Schwarz FSWP26). All radio-frequency equipment is linked to a 10 MHz reference derived from a hydrogen maser for long-term stable frequency calibration.

A 20%-fraction of the output, having passed a mirror with -500 fs^2 group delay dispersion, is used to generate an octave-spanning supercontinuum in a 1 m-long photonic crystal fiber (PCF, NKT SC-3.2-945) for f -to- $2f$ interferometry [23] as explained in the following: At the fiber exit, the continuum is split by a 1000 nm-cut-off long-pass filter to allow for compensation of the group delay between the generated Raman soliton at 1380 nm and the dispersive wave at 690 nm. Corresponding half-wave plates in the indicated positions allow rotating the polarization of both spectral components. The beams are recombined at the previous long-pass filter and picked up using a D-shaped mirror. The now overlapped beams are sent through a 3 mm-long periodically poled lithium-niobate crystal (PPLN, Poling period 14 μm , Temperature 50°C) where the Raman soliton is frequency doubled. The interference is detected by an avalanche photo diode (Menlo Systems APD 210) after a bandpass filter ($690 \pm 5 \text{ nm}$). The beat-note arising at around 300 MHz is electronically filtered and amplified to 10 dBm (2x RF Bay LNA-530) before it is inserted into a double-balanced mixer (Mini-Circuits ZAD-1-1+). There, it is mixed with a 10 dBm-level 300 MHz-frequency sine wave from a first reference synthesizer (HP 8656B). The mixer output is low-pass filtered and fed as error signal into a proportional-integral controller (New Focus LB1005) whose output is sent to the pump diode via a voltage-to-current converter (same as used in Ref. [19]). The direct-current supply of the pump diode is shielded from the current modulation using a large RC-element ($R = 1 \Omega$, $C = 0.1 \text{ F}$).

The repetition rate stabilization is implemented with a fast photo diode (New Focus 1434). The 10th harmonic of the repetition rate is selected by a cavity filter with 40 MHz bandwidth at 10 GHz frequency. The signal is amplified to 3 dBm (Mini-Circuits ZX60-05113LN+, RF Bay GNA-157F) and mixed (Mini-Circuits ZX05-153-S+) with a 5 dBm-level sine wave from a second reference synthesizer (Agilent E8257D). The resulting baseband signal is low-pass filtered at a corner frequency of 1 MHz and fed into a second proportional-integral controller (Vescent Photonics D2-125). The controller output is off-set and amplified in a high-voltage amplifier (Falco Systems WMA-300) to drive the unipolar piezo actuator.

3. Experiment

3.1. Laser characterization

Kerr-lens mode-locked oscillators pumped by transversal multi-mode beams are rarely self-starting and the rigid assembly forbids starting by mechanical perturbation. Here, mode-locked operation is reliably achieved by giving optical feedback to the cavity by rotating a mirror in front of the output coupler, which makes the average output power jump from 1.8 W in continuous-wave to 3.5 W in mode-locked operation. The laser then emits pulses at 1 GHz repetition rate and operates at an optical-to-optical efficiency of 25%. Single-pulse operation is verified by checking the harmonics of the radio-frequency spectrum and by checking the time domain signal in a fast-sampling scope.

The optical spectrum and the autocorrelation trace are depicted in Fig. 2. The spectrum features a hyperbolic secant (sech^2) shape centered at 1050 nm wavelength. The full width at half-maximum (FWHM) is 28 nm. Below 1000 nm wavelength, the spectrum is truncated by the dichroic cavity end mirror and a residual of the pump light is visible at 980 nm. Kelly sidebands

[26,27] arise at the wavelengths 1100 nm, 1130 nm, and 1145 nm. They occur due to the steep change of the round-trip GDD (overlaid in gray) in this wavelength range induced by the mirror coatings. On the short-wave end, the Kelly sidebands are cut by the dichroic. Implementing our in-house developed cross-polarization pumping scheme [28] would allow to suppress the Kelly sidebands and to reach even shorter pulse duration.

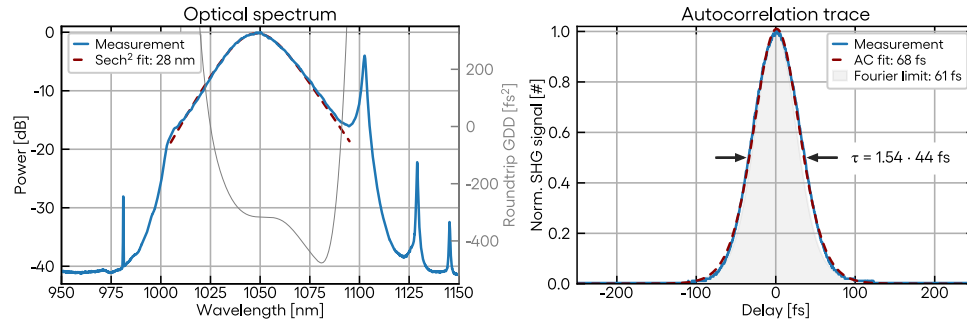


Fig. 2. (Left panel) Measured and fitted optical spectrum overlaid with the cavity round-trip group delay dispersion (gray). The peaks at 980 nm and beyond 1100 nm respectively are a residual of the pump and three Kelly sidebands. The short-wave end of the soliton spectrum is truncated at 1000 nm by the dichroic coating of the gain crystal. (Right panel) Measured, fitted, and calculated Fourier-limited autocorrelation traces revealing a pulse duration of 44 fs.

The measured (blue) and fitted (red) autocorrelation traces are shown in the right panel of Fig. 2. The fitted FWHM of 68 fs corresponds to a hyperbolic secant pulse duration of 44 fs. This is 11% above the Fourier limit (shown as gray area) of all spectral content above -25 dB level, which is explained by the deviation of the spectral shape from an ideal hyperbolic secant and residual dispersion.

3.2. Environmental stability

The passive stability of the laser was tested prior to stabilizing the laser into a frequency comb.

First, the average power and the repetition rate of the free-running laser were observed for 16 hours at constant setpoint of the water-cooling system. The repetition rate was measured every 10 seconds with the RF-spectrometer. The average power was tracked by measuring a 100 mW-level beam sample with a fast thermal power meter at 1 sample per second. The results are shown in the left panels of Fig. 3. Over the full time, the average power has a relative standard deviation of 0.27%. The repetition rate drifts by 4.5 kHz peak-to-peak, which is less than the 30-kHz repetition-rate lever of the piezo.

Second, the impact of larger temperature variation was tested with the results shown in the right panels of Fig. 3. The temperature was changed by adjusting the setpoint of the water-cooling system and it was measured using a PT100-sensor at the aluminum housing. Temperatures below 17°C were not tested to avoid condensation in the laser housing and the experiment was stopped at 47°C to avoid potential damage. Returning to the normal operating temperature of 21°C reestablished the initial output parameters. The mode-locking was continuous over the 30°C temperature span, which is a larger than reported for the similarly built soft-aperture Kerr-lens mode-locked laser in Ref. [29]. Apparently, the hard aperture keeps the laser mode-locked for even larger misalignment. The repetition rate reduced by 29 kHz per degree centigrade over the full temperature span. This is 26% more than expected from the relative linear expansion of aluminum alone and is most likely due to the temperature-induced refractive index change in the gain medium and in the output coupler. Regarding the free-running system, the long-term

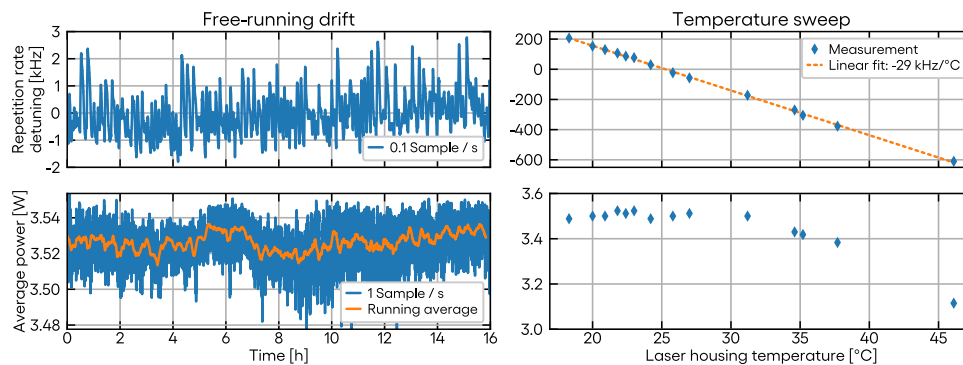


Fig. 3. Repetition-rate detuning and average power of the laser logged for 16 hours in free-running operation (left column) and for different housing temperatures (right column). The relative standard deviation of the average power is 0.27% and the repetition rate drifts within a span of 4.5 kHz.

frequency drifts infer a peak-to-peak temperature deviation of 0.15°C, which is within the specifications of the cooling system.

In essence, a robust laser oscillator has been built reproducing the power level and pulse duration achieved in Ref. [22]. The all-glued assembly impedes misalignment even after temperature cycling. The piezo travel range is sufficient to cover the free-running drift of the repetition rate for normal operating conditions.

3.3. Stabilization of the repetition rate and of the carrier-envelope offset frequency

The laser was stabilized via the two control loops shown in Fig. 1. The repetition rate was locked at its 10th harmonic to a 10-GHz reference. The self-referencing of the carrier-envelope offset frequency requires a supercontinuum and subsequent f -to- $2f$ interferometry. For that, an average power of 710 mW was coupled in the nonlinear fiber resulting in 490 mW average power at the output. This corresponds to a coupling efficiency of 70% and leaves 2.7 W average power in the main beam for application. The free-running carrier-envelope offset frequency was adjustable in the stable mode-locking range between 260 MHz and 320 MHz via the drive current. The current was set closer to the upper limit to lock at 300 MHz. For both control loops, the proportional and integral gain were optimized by visually minimizing the sidebands of the respective radio-frequency peaks. The phase noise of the repetition rate was measured using a separate, amplified photo diode. The phase noise of the carrier-envelope offset frequency was measured in-loop in lack of a second supercontinuum generation fiber and a second f -to- $2f$ interferometer. However, the difference between in-loop and out-of-loop measurements is typically not significant [30].

The resultant single-sideband phase noise power spectral densities (PSD) and their corresponding integrated curves are shown in Fig. 4. Data presented for a locked state is for both loops closed, while for a free-running state the respective other loop remains closed.

The repetition rate phase noise measured at 10 GHz carrier is displayed in the left panels. The flicker noise in free-running operation decreases at approximately 40 dB per decade from 1 Hz to 10 kHz before it subsides into the shot noise. There are scattered peaks at the grid-frequency and its harmonics that couple into the system via the driving electronics. Further, one broad bump exists at around 500 Hz, which indicates a mechanical resonance in the assembly. The free-running integrated timing jitter is 140 ps in the full span from 1 Hz and 10 MHz. Once the feedback loop is closed, the noise reduces to the synthesizer limit up to a frequency of 1 kHz

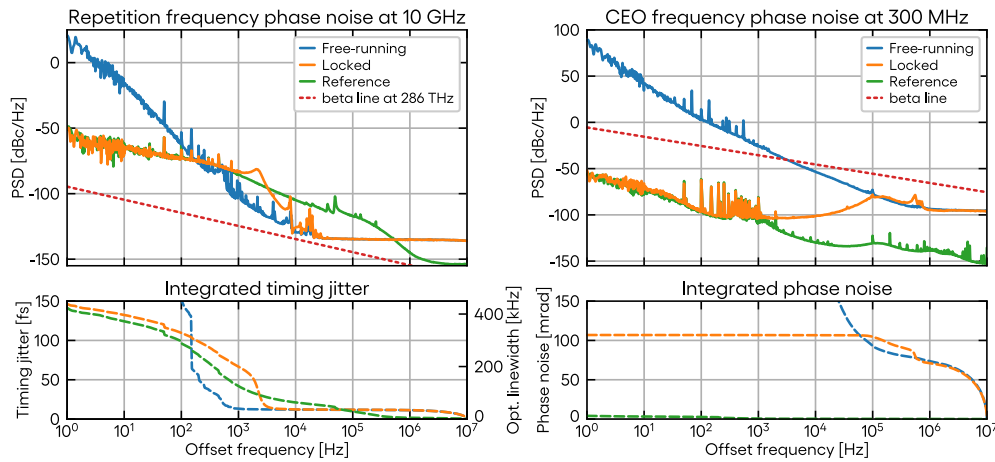


Fig. 4. Phase noise power spectral density of the repetition frequency (left column) and of the carrier-envelope offset frequency (CEO, right column) for free-running and simultaneously locked state. The phase noise of the respective reference synthesizers and the beta-separation lines are shown. Integrated over the full span, the timing jitter at the fundamental repetition rate is 146 fs and the phase noise of the carrier-envelope offset frequency is 107 mrad.

with a servo bump at 2.5 kHz and the full-span integrated timing jitter becomes 146 fs. This value is mostly limited by the servo bump and by the reference, while the detection noise floor at -135 dBc/Hz above 30 kHz is not a significant contribution. The beta separation line [31] is shown down-scaled from the optical frequency of 286 THz (1.05 μm) to the 10-GHz carrier measured and lies below all noise measured. Thus, the FWHM of the optical comb teeth [31] can be estimated and evaluates as an upper limit to 440 kHz for 1 s observation time. A better electronic reference or optical referencing would allow for further linewidth reduction.

The phase noise of the carrier-envelope offset frequency is depicted in the right panels and qualitatively behaves like the repetition rate phase noise. Albeit starting from a higher value in free-running operation, it decreases by approximately 40 dB per decade and disappears into the noise floor at -95 dBc/Hz limited by the interference contrast of the f -to- $2f$ -interferometer. The residual noise is limited by the reference synthesizer up to 1 kHz frequency. From 1 kHz to 100 kHz the limit is the noise floor of the f -to- $2f$ -interferometer. Finally, the servo bump is located between 100 kHz and 800 kHz. The full-span integrated phase noise is 107 mrad and is entirely determined by the servo bump and the detection noise floor. The residual noise lies well below the beta separation line at all frequencies, implying no influence of the carrier-envelope offset frequency on the comb tooth linewidth.

4. Comparison to state-of-the-art optical frequency combs

The presented source is the first multi-mode pumped Kerr-lens mode-locked OFC at gigahertz-level repetition rate. In the following, its residual noise is compared to state-of-the-art solid-state OFCs. All residual noise values with the accordingly adapted integration ranges are summarized in Table 1.

Compared to multi-mode pumped, SESAM mode-locked gigahertz oscillators [19,20,32], the residual phase noise of the carrier-envelope offset frequency is 6 to 8 times lower. Thus, operation close to the stability edge in Kerr-lens mode-locked oscillators is no disadvantage in this regard. Rather, the shorter pulse duration enabled by Kerr-lensing seems advantageous for obtaining a higher signal-to-noise ratio in the carrier-envelope offset frequency detection and,

Table 1. Comparison of this work's residual noise to other bulk optical frequency combs

Ref.	Architecture	Limits [Hz]	CEO noise [mrad]		Timing jitter [fs]	
			Ref.	This work	Ref.	This work
[19]	SESAM, Yb:Calgo, multimode pump	$10^\circ - 10^6$	680	80	700	146
[20]	SESAM, Yb:Calgo, multimode pump	$10^\circ - 5 \cdot 10^6$	774	94	-	-
[32]	SESAM, VECSEL, multimode pump	$10^\circ - 10^6$	448	80	257	146
[6]	SESAM, Er:Yb:glass, optical reference, single-mode pumps	$10^2 - 10^7$	438	107	0.03	110
[11]	SESAM, Er:Yb:glass, monolithic, single-mode pumps	$10^2 - 10^6$	14	80	-	-
[24]	KLM, Yb:Y ₂ O ₃ , single-mode pump	$10^\circ - 10^6$	-	-	318	146
[34]	KLM, Yb:CaF ₂ , single-mode pump	$10^\circ - 10^6$	67	80	-	-

thus, a tighter lock. Also, the timing jitter is improved by a factor of two, which is attributable to the higher rigidity of the assembly.

Next, this work is compared to two erbium-ytterbium-doped glass based master-oscillator power-amplifiers [6,11], which are considered well-suited for low-noise operation due to the low-pass filtering effect of the gain medium with respect to pump noise [33]:

Reference [6] exhibits an identical free-running carrier-envelope offset frequency noise. Thus, it seems not to be significant whether the comb is based on an ytterbium-doped or erbium-ytterbium-doped gain media. In closed-loop, the current work performs even better due to a larger control-loop bandwidth. Then, in Ref. [6] one comb tooth is locked in the optical domain to a cavity-stabilized continuous-wave laser, which naturally results in a superior timing jitter compared to locking in the radio-frequency domain.

Reference [11] presents a truly monolithic oscillator. Its residual noise for the carrier-envelope offset-frequency is 6-times lower compared to this work. This difference indeed could be due to the claimed fundamental-physical advantages or due to the control loop in this work not being optimized to obtain the smallest possible value for this frequency range. This difference will be the subject of future investigations.

Lastly, Refs. [24,34] present OFCs based on single-mode-pumped Kerr-lens mode-locked oscillators. Reference [24] is a similar all-glued assembly, but the residual timing jitter is slightly higher than in this work due to a lower control-loop bandwidth. Reference [34] features an almost identical residual carrier-envelope offset frequency noise, although not operating at gigahertz repetition rate. Thus, there is no apparent advantage in single-mode over multimode pumping for OFCs based on ytterbium-doped gain media.

Overall, the combination of Kerr-lens mode-locking with multimode pumping results in a similar or better noise performance compared to state-of-the-art bulk OFCs.

5. Conclusion

In summary, a powerful and low-noise optical frequency comb at 1 GHz repetition rate has been presented. The laser is based on Kerr-lens mode-locking of Ytterbium-doped CALGO and emits sub-50 femtosecond pulses and 3.5 W average power at 1.05 μm wavelength. The rigid, all-glued assembly ensures long-term stable operation and withstands temperature cycling. Stabilized, the residual timing jitter of the repetition rate is 146 fs and the residual phase noise of the carrier envelope offset frequency is 107 mrad, both in the frequency span from 1 Hz to 10 MHz. A comparison to state-of-the-art OFCs shows that Kerr-lens mode-locking and multimode pumping are not inhibiting low-noise operation.

The presented laser can be improved on by proper dispersive mirrors and further packaging, which so far has not included the pump diode. The stability and width of the optical comb lines can be reduced substantially by referencing in the optical domain to a stabilized continuous wave laser [6] instead of stabilizing the repetition-rate in the radio-frequency domain.

The presented source is the first multi-mode pumped Kerr-lens mode-locked OFC at gigahertz-level repetition rate. After stabilization, it features Watt-level average and multi-kW-level peak power enabling direct nonlinear frequency conversion, e.g. to ultraviolet [13] or mid-infrared [35]. Also, spectral broadening of the full output is conceivable to generate low-noise octave-spanning spectra, i.e. in a photonic crystal fiber [17]. Thus, this laser can be a versatile and cost-effective driver for various OFC-based applications.

Funding. Schweizerischer Nationalfonds zur Förderung der Wissenschaftlichen Forschung (198176, 200774).

Acknowledgments. The authors would like to thank Jakob Drs for helpful discussions and the support in electronics.

Disclosures. The authors declare no conflict of interest.

Data availability. Data underlying the results presented in Fig. 4 are available in Dataset 1, [36], Dataset 2 [37]. All other data underlying the results presented in this paper are not publicly available at this time but may be obtained from the authors upon reasonable request.

References

1. T. Fortier and E. Baumann, "20 years of developments in optical frequency comb technology and applications," *Commun. Phys.* **2**(1), 153 (2019).
2. N. Picqué and T. W. Hänsch, "Frequency comb spectroscopy," *Nat. Photonics* **13**(3), 146–157 (2019).
3. M. Endo, T. D. Shoji, and T. R. Schibli, "Ultralow Noise Optical Frequency Combs," *IEEE J. Select. Topics Quantum Electron.* **24**(5), 1–13 (2018).
4. S. A. Diddams, K. Vahala, and T. Udem, "Optical frequency combs: Coherently uniting the electromagnetic spectrum," *Science* **369**(6501), eaay3676 (2020).
5. S. Kurata, H. Ishii, K. Terada, *et al.*, "Dead-zone free single-shot three-dimensional measurement using a high-repetition-rate Yb: fiber comb," *Opt. Continuum* **1**(11), 2374–2387 (2022).
6. D. M. B. Lesko, A. J. Lind, N. Hoghooghi, *et al.*, "Fully phase-stabilized 1 GHz turnkey frequency comb at 1.56 μm ," *OSA Continuum* **3**(8), 2070–2077 (2020).
7. C. R. Phillips, B. Willenberg, A. Nussbaum-Lapping, *et al.*, "Coherently averaged dual-comb spectroscopy with a low-noise and high-power free-running gigahertz dual-comb laser," *Opt. Express* **31**(5), 7103–7119 (2023).
8. T. M. Fortier, A. Bartels, and S. A. Diddams, "Octave-spanning Ti:sapphire laser with a repetition rate >1 GHz for optical frequency measurements and comparisons," *Opt. Lett.* **31**(7), 1011–1013 (2006).
9. S. A. Diddams, T. Udem, J. C. Bergquist, *et al.*, "An Optical Clock Based on a Single Trapped $^{199}\text{Hg}^+$ Ion," *Science* **293**(5531), 825–828 (2001).
10. S. Pekarek, T. Südmeyer, S. Lecomte, *et al.*, "Self-referenceable frequency comb from a gigahertz diode-pumped solid-state laser," *Opt. Express* **19**(17), 16491–16497 (2011).
11. T. D. Shoji, W. Xie, K. L. Silverman, *et al.*, "Ultra-low-noise monolithic mode-locked solid-state laser," *Optica* **3**(9), 995–998 (2016).
12. V. Smolski, S. Vasilyev, I. Moskalev, *et al.*, "Half-Watt average power femtosecond source spanning 3–8 μm based on subharmonic generation in GaAs," *Appl. Phys. B* **124**(6), 101 (2018).
13. R. J. Jones, K. D. Moll, M. J. Thorpe, *et al.*, "Phase-Coherent Frequency Combs in the Vacuum Ultraviolet via High-Harmonic Generation inside a Femtosecond Enhancement Cavity," *Phys. Rev. Lett.* **94**(19), 193201 (2005).
14. M. Roiz, K. Kumar, J. Karhu, *et al.*, "Simple method for mid-infrared optical frequency comb generation with dynamic offset frequency tuning," *APL Photonics* **6**(2), 026103 (2021).
15. C. P. Bauer, S. L. Camenzind, J. Pupeikis, *et al.*, "Dual-comb optical parametric oscillator in the mid-infrared based on a single free-running cavity," *Opt. Express* **30**(11), 19904–19921 (2022).
16. T. Nakamura, V. Ramaiah Badarla, K. Hashimoto, *et al.*, "Simple approach to broadband mid-infrared pulse generation with a mode-locked Yb-doped fiber laser," *Opt. Lett.* **47**(7), 1790–1793 (2022).
17. E. Genier, S. Grelet, R. D. Engelsholm, *et al.*, "Ultra-flat, low-noise, and linearly polarized fiber supercontinuum source covering 670–1390 nm," *Opt. Lett.* **46**(8), 1820–1823 (2021).
18. H. Wang, J. Pan, Y. Meng, *et al.*, "Advances of Yb:CALGO Laser Crystals," *Crystals* **11**(9), 1131 (2021).
19. S. Hakobyan, V. J. Wittwer, P. Brochard, *et al.*, "Full stabilization and characterization of an optical frequency comb from a diode-pumped solid-state laser with GHz repetition rate," *Opt. Express* **25**(17), 20437–20453 (2017).
20. A. Klenner, S. Schilt, T. Südmeyer, *et al.*, "Gigahertz frequency comb from a diode-pumped solid-state laser," *Opt. Express* **22**(25), 31008–31019 (2014).
21. L. M. Molteni, L. M. Molteni, F. Canella, *et al.*, "Low-noise Yb:CALGO optical frequency comb," *Opt. Express* **29**(13), 19495–19505 (2021).

22. M. Hamrouni, F. Labaye, N. Modsching, *et al.*, “Efficient high-power sub-50-fs gigahertz repetition rate diode-pumped solid-state laser,” *Opt. Express* **30**(17), 30012–30019 (2022).
23. H. R. Telle, G. Steinmeyer, A. E. Dunlop, *et al.*, “Carrier-envelope offset phase control: A novel concept for absolute optical frequency measurement and ultrashort pulse generation,” *Appl. Phys. B: Lasers Opt.* **69**(4), 327–332 (1999).
24. Y. Feng, T. P. Lamour, H. Ostapenko, *et al.*, “Towards a space-qualified Kerr-lens mode-locked laser,” *Opt. Lett.* **46**(21), 5429–5432 (2021).
25. A. Delgoffe, S. Nazir, S. Hakobyan, *et al.*, “All-glass miniature GHz repetition rate femtosecond laser cavity,” *Optica* **10**(10), 1269–1279 (2023).
26. S. M. J. Kelly, “Characteristic sideband instability of periodically amplified average soliton,” *Electron. Lett.* **28**(8), 806–807 (1992).
27. S. Kelly, “Erratum: Characteristic sideband instability of periodically amplified average soliton,” *Electron. Lett.* **28**(16), 1562 (1992).
28. F. Labaye, V. J. Wittwer, M. Hamrouni, *et al.*, “Efficient few-cycle Yb-doped laser oscillator with Watt-level average power,” *Opt. Express* **30**(2), 2528–2538 (2022).
29. H. Ostapenko, Y. Feng, T. Lamour, *et al.*, “Misalignment-free, Kerr-lens-modelocked Yb:Y₂O₃ 2.2-GHz oscillator, amplified by a semiconductor optical amplifier,” *Opt. Express* **31**(2), 3249–3257 (2023).
30. E. Shestaev, S. Hädrich, N. Walther, *et al.*, “Carrier-envelope offset stable, coherently combined ytterbium-doped fiber CPA delivering 1 kW of average power,” *Opt. Lett.* **45**(23), 6350–6353 (2020).
31. G. Di Domenico, S. Schilt, and P. Thomann, “Simple approach to the relation between laser frequency noise and laser line shape,” *Appl. Opt.* **49**(25), 4801–4807 (2010).
32. D. Waldburger, A. S. Mayer, C. G. E. Alfieri, *et al.*, “Tightly locked optical frequency comb from a semiconductor disk laser,” *Opt. Express* **27**(3), 1786–1796 (2019).
33. A. Schlatter, S. C. Zeller, R. Grange, *et al.*, “Pulse-energy dynamics of passively mode-locked solid-state lasers above the Q-switching threshold,” *J. Opt. Soc. Am. B* **21**(8), 1469–1478 (2004).
34. M. Kowalczyk, A. Hudzikowski, M. Porebski, *et al.*, “Low-Noise Carrier-Envelope-Offset-Stabilized Yb:CaF₂ Oscillator,” *IEEE Photonics Technol. Lett.* **32**(13), 823–826 (2020).
35. V. Petrov, V. V. Badikov, D. V. Badikov, *et al.*, “Barium nonlinear optical crystals for the mid-IR: characterization and some applications,” *J. Opt. Soc. Am. B* **38**(8), B46–B58 (2021).
36. M. Müller, M. Hamrouni, A. Komagatam, *et al.*, “The phase noise data for the carrier-envelope offset stabilization as displayed in Figure 4,” figshare, (2023) <https://doi.org/10.6084/m9.figshare.24648312>.
37. M. Müller, M. Hamrouni, A. Komagatam, *et al.*, “The phase noise data for the repetition-rate stabilization as displayed in Figure 4,” figshare, (2023) <https://doi.org/10.6084/m9.figshare.24648309>.

2.3 Efficient few-cycle Yb-doped laser oscillator with Watt-level average power

In section 2.1, we observed that in the configuration optimized for short pulse duration, the generated spectrum exhibits undesired spectral features that subtract a part of the generated power off the main soliton. This limitation is mainly due to the utilization of a dichroic mirror to couple the pump inside the cavity. The dichroic mirror is transmissive for the pump at 980 nm and reflective for laser wavelengths above 980 nm. The sharp transition of the mirror reflectivity around 980 nm inherently results in rapid and strong variations of the group delay dispersion (GDD), which introduces undesired spectral features in the spectrum when operating close to this transition, in addition to limiting spectral extensions beyond the pump wavelength. The article presented in this section tackles this issue and demonstrates a novel pumping technique for efficient generation of few-cycle pulses using Yb:CALGO gain material.

2.3.1 Article outlines

Context

Over the last two decades, Yb-doped gain materials have stimulated a lot of enthusiastic research for delivering high average power and short pulse durations. Among those gain materials, Yb:CALGO is one of the most promising candidates. In the overview plot (Fig. 1.(c,d) in the article), we observe that Yb-doped materials have already surpassed Ti:sapphire in terms of average power and optical-to-optical efficiency when operating with pulses longer than 50 fs [22, 23]. In contrast, in the sub-50-fs regime, Ti:sapphire performance still dominates the literature. In this regime, we observe a significant decrease of the average power and optical-to-optical efficiency of Yb-based lasers as the pulse duration approaches the few-cycle regime. For instance, prior to this work, Yb:CALGO laser oscillators operating with sub-30-fs pulses never exceeded optical-to-optical efficiency higher than a few percents. As previously mentioned, regular collinear pumping schemes employ a dichroic mirror that has a high transmission for the pump wavelength and a high reflectivity for the laser wavelength. Those mirrors hinder spectral extension below the 980-nm pump wavelength and introduce detrimental spectral features when the blue tail of the spectrum approaches 980 nm. The consequences of these mirrors can be clearly observed in [24] where sub-20-fs pulses with only 0.5% efficiency are demonstrated using the conventional collinear pumping scheme. There, the generated soliton is accompanied by a dispersive wave that manifests by a sharp

peak around 1000 nm. Also, the peak of the spectrum is red-shifted away from the peak of the emission gain bandwidth, which further reduces the efficiency.

Instead of using a conventional dichroic mirror, in our article we present a novel mirror concept where the reflectivity and dispersion properties depend on the polarization of the beam. More specifically, these mirrors are highly transmissive for the p-polarized pump light and highly reflective for the s-polarized laser beam over a broad wavelength range extending well beyond the pump wavelength (see Fig. 1 from the article). This concept enables efficient collinear pumping while bypassing the limitation imposed by the low quantum defect. In contrast to a standard thin-film polarizer, these mirrors provide a low and flat GDD over a broad spectral range for the laser s-polarized light.

Results

When optimized for short pulse durations, the KLM Yb:CALGO laser delivers 22-fs pulses at a remarkably high optical-to-optical efficiency of 25% and 730 mW of average power. The generated pulses are close to the Fourier-transform limit and the spectrum, which extends well beyond the pump wavelength, remains much smoother over the entire bandwidth compared to previous Yb-based oscillators operating around 20-fs pulse durations [24, 25]. Typically, the absence of a dispersive wave in the spectrum for such large spectral bandwidths clearly underlines the benefits of our concept. Additionally, the bandwidth extends well beyond the blue tail of the Yb:CALGO gain cross section, which indicates that the laser operates with a high amount of self-phase modulation (SPM).

In the final section, we further study the advantages of our approach. We compare two distinct configurations, both employing the cross-polarization pumping scheme. In the first configuration, we use highly reflective mirrors that feature broad and flat GDD. In the second configuration, one of those broadband mirrors is substituted with a conventional dichroic mirror. This apple-to-apple comparison isolates the impact of regular dichroic mirrors on the laser performance. We repeat this comparison for different output coupling rates. The results are summarized in Table 1 and shown Fig. 5 of the article. The presence of dichroic mirrors clearly leads to lower average power, smaller spectral bandwidths and lower optical-to-optical efficiencies. Also, the impact of the dichroic mirror on the output power is exacerbated at higher output coupling rates. This behavior is expected since the Yb:CALGO gain cross-section shifts toward the pump wavelength at higher inversion levels, which effectively further reduces the quantum defect.

Conclusion

This work unambiguously demonstrates the strong benefit of the cross-polarization pumping technique to achieve short pulse duration at high optical-to-optical efficiency using Yb:CALGO gain material. The results obtained here do not suggest the technique has reached limitations. Using mirrors with broader reflectivity and GDD bandwidths, in addition to leveraging SPM should allow the generation of shorter pulses.

2.3.2 Towards a cost-efficient version: multimode diode pumping

In the article, the Yb:CALGO crystal is pumped by a high-brightness diffraction-limited fiber laser from Azur Light Systems. The large cost (approximately 20k\$) and footprint of this pumping system present a barrier to replicate the laser and limit its use to in-lab applications. In fact, the price of the pump exceeds by far the rest of the laser components, and its volume is larger than the cavity itself. In the conclusion of the article, we state that it should be possible to demonstrate similar performance using a cost-efficient multimode diode. In a follow-up experiment, we address this challenge and replace the high-brightness pump system by a low-cost (<1k\$), off-the-shelf, powerful multimode pump diode. In addition, the pump wavelength of the diode is selected and stabilized by a volume Bragg grating (VBG) directly implemented in the diode package to perfectly match the absorption peak of the Yb:CALGO material. In contrast, the Azur Light system used in the previous experiment emits around 976 nm, which is 4 nm off from the Yb:CALGO absorption peak at 980 nm and results in 1.7-times lower absorption.

Experimental setup

A schematic of the new laser version pumped by the multimode diode is depicted in figure 2.4. The 4-mm-long Yb:CALGO crystal is pumped by a fiber-coupled (105- μm core and 0.15 of numerical aperture) multimode laser diode delivering a maximum power of 20 W centered at 980 nm. The pump beam is collimated by a 60-mm focal length aspherical lens and subsequently focused into the crystal with another identical lens. The diameter of the pump beam at the focus inside the gain crystal is estimated to be 120 μm . The size of the pump and laser beam in the crystal was experimentally optimized to achieve a good tradeoff between high intensity and large gain volume. To compensate the astigmatism introduced by the cross-polarized dichroic mirror placed at 60° angle of incidence, a plate with an antireflection coating for the s-polarization is put in the orthogonal plane in front of the pump diode. A Kerr-medium (5-mm YAG plate) is

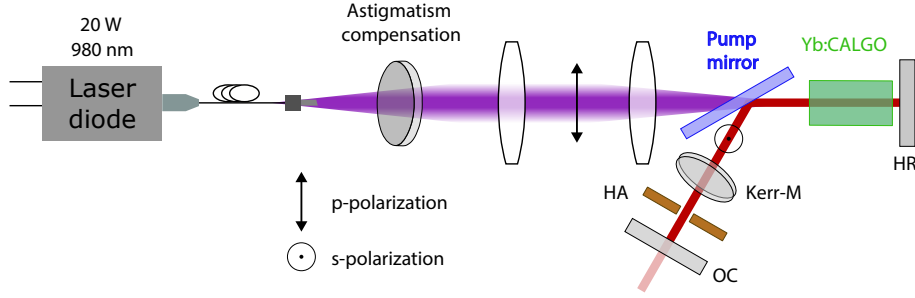


Figure 2.4: Simplified scheme of the laser oscillator combining our novel cross-polarization pumping approach with a multimode pump diode. The multimode diode delivers up to 20 W centered around 980 nm. HR: high reflective mirror; Kerr-M: Kerr medium; HA: hard aperture; OC: output coupler. The curved and dispersive mirrors of the cavity and the hard aperture are not shown.

inserted inside the cavity at the Brewster angle to further enhance the generation of spectral components via SPM. We use dispersive mirrors to over-compensate the dispersion introduced by the gain material and the Kerr-medium. The laser operates with a total GDD per cavity round-trip of -300 fs^2 . Due to the high mode mismatch between the multimode pump and the laser beam, operating the KLM regime in the soft-aperture configuration is not convenient. Thus, we design the cavity for hard-aperture mode-locking. The hard aperture consisting of an uncooled copper plate is inserted in front of the output coupler where the laser beam is collimated. Besides promoting the KLM regime, the hard aperture significantly improve the beam quality. Operation in the KLM regime is initiated by gently pushing the output coupler mounted on a translation stage. The experimental results are discussed below and summarized in Table 2.1.

Experimental results

Using a 3% output coupling rate, the laser delivers 300 mW in 22-fs pulses at 85 MHz repetition rate, resulting in a peak power of 140 kW and 4% optical-to-optical efficiency. The generated spectrum and autocorrelation trace are shown in Figure 2.5. The optical spectrum is centered at 1044 nm and has a full width at half maximum (FWHM) bandwidth of 70 nm. The spectral contents extend well beyond the pump wavelength, which is enabled by the cross-polarized pumping scheme. The SHG-FROG measurements indicate the generated pulses are close to the transform limit. The spectral phase features a quadratic coefficient of only $\sim 20 \text{ fs}^2$, showing the out-coupled pulses are only slightly chirped. We observe the presence of discrepancies between the measured and retrieved spectra. We note here that the measured spectrum was acquired with a HP 70952 spectrometer while the retrieved spectrum from the FROG measurement

Table 2.1: Laser performance in mode-locked operation. The first row corresponds to the results obtained in this work. To facilitate the comparison, the results obtained in the article using a high brightness pump are summarized in the second row.^a

	T_{OC} (%)	f_{rep} (MHz)	P_{pump} (W)	P_{ave} (mW)	τ (fs)	$\Delta\lambda$ (nm)	P_{peak} (kW)	η_{eff} (%)
This work	3	85	7.75	250	22	70	140	3.5
From the article	11.5	134	2.93	729	22	82	218	25

^a T_{OC} : output coupling rate; f_{rep} : repetition rate; P_{pump} : pump power; P_{ave} : output average power; τ : pulse duration; $\Delta\lambda$: spectral bandwidth; P_{peak} : output peak power; η_{eff} : optical-to-optical efficiency

was obtained using a Femto Easy device. The spectral discrepancies can be attributed to the reconstruction error in the FROG algorithm combined with the limited accuracy of the FROG spectrometer. We observe the presence of spikes on the tails of the measured spectrum, which are not captured by the FROG retrieval. This may indicate these spectral features are temporally separated from the main pulses. However, given the small amplitude of these spikes, they have only minor contribution to the generated power. We also verified the stability of the mode-locking regime and the single-pulse operation using a radio-frequency spectrum analyzer and a sampling scope, respectively (not shown in the figure).

Comparison to state-of-the-art mode-locked lasers

We first compare these results with those reported in the article, obtained with the expensive pump (section 2.3.4). Both lasers demonstrate the same pulse duration and achieve comparable spectral bandwidths (Figure 2.6). However, the laser employing the high-brightness pump generates a slightly cleaner spectrum and reaches significantly higher optical-to-optical efficiency. While further investigation is necessary to pinpoint the exact causes of these differences, I expect they stem from better management of the cavity dispersion and SPM effects.

To put this work in more context, it is interesting to compare this source with other Yb-doped bulk laser oscillators (Fig. 2.7). We observe that within the category of lasers pumped by a single-mode diode (red dots), only the result obtained in our article demonstrates shorter pulses and higher average power at the same time. Additionally, our laser demonstrates the shortest pulse duration compared to any other Yb-based oscillator pumped with a multimode diode. It also achieves the highest average power when restraining the comparison to sources delivering sub-30-fs pulse duration.

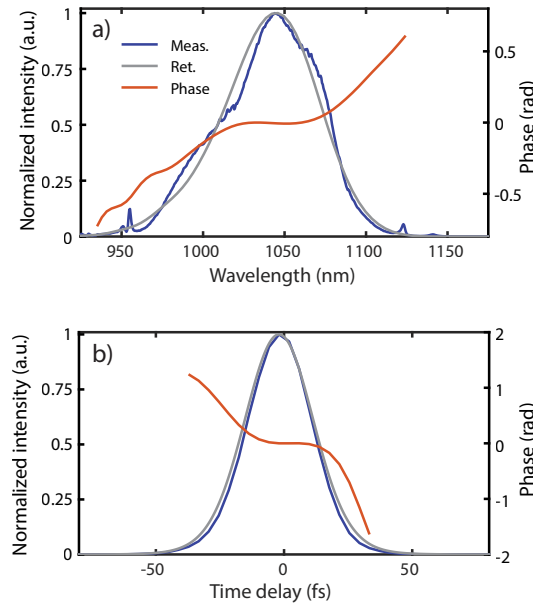


Figure 2.5: Characterization of the hard-aperture KLM Yb:CALGO laser oscillator pumped with a multimode pump diode. (a) Measured (blue) and retrieved (gray) optical spectra and spectral phase (light blue curve). (b) Measured (blue) and retrieved (gray) intensity profile and temporal phase (light red) of the output pulses. The slight discrepancies between the measured and retrieved traces can be attributed to the reconstruction error in the FROG algorithm combined with the limited accuracy of the FROG spectrometer.

Outlook

Looking ahead, I believe achieving shorter pulses will require considerable additional efforts. Even in the optimal configuration, which is based on single-mode pumping, the generated spectra slightly deviate from perfect solitons. This behavior may indicate that the laser operates with spectral bandwidths at the limit of what the cavity mirrors can support. Also, it is possible that additional nonlinear effects occurring in the Kerr medium are no longer negligible and must be taken into account to fully capture the pulse dynamics inside the cavity. In the future, I foresee few changes that can be done to reach shorter pulses. First, controlling the cavity dispersion using ultra-broadband complementary pairs of chirped mirrors instead of conventional dispersive mirrors should allow to extend the GDD bandwidth. Since those ultra-broadband pair of mirrors have been already employed in Ti:sapphire lasers for delivering nearly single-cycle pulses [26, 27], I expect this technique could also be implemented in our laser.

Another challenge is increasing the amount of SPM to counteract the gain clipping effects and further improve the efficiency. For this, we could insert a multi-pass compression cell directly inside the laser cavity. Multi-pass cells

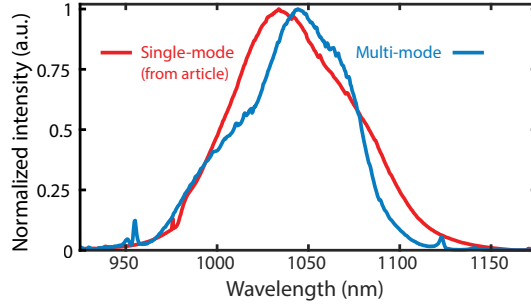


Figure 2.6: Comparison of the spectrum generated by the single-mode (red) and multi-mode (blue) -pumped laser. The spectrum in red is extracted from the article 2.3.4 (Figure 3a).

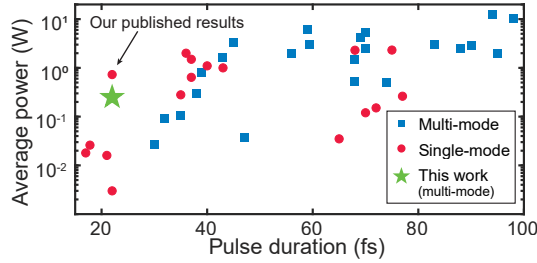


Figure 2.7: Selection of state-of-the-art Yb-based solid-state laser oscillators delivering sub-100-fs pulses. The blue squares and red dots correspond to multimode and single-mode pumping, respectively.

are commonly used to post-compress high-energy pulses down to few cycles with high spectral purity [28–30], however they have never been employed inside a laser oscillator for this purpose. This approach may open a new path for generating clean few-cycles soliton pulses at high efficiency. However, this technique imposes stringent requirements on the reflectivity of the mirrors and GDD bandwidth, which is technically challenging to achieve.

2.3.3 Acknowledgment

The experiments conducted in this section have been performed to a major extent by my co-workers, especially Francois Labaye and Firas Trawi for the first and second version, respectively. Sincere thanks for their outstanding results. I also thank Valentin Wittwer for the excellent coatings at the core of this work, and for his technical support.



Efficient few-cycle Yb-doped laser oscillator with Watt-level average power

FRANÇOIS LABAYE,^{1,*}  VALENTIN J. WITTEW, ¹  MARIN HAMROUNI,¹ NORBERT MODSCHING,¹  ERIC CORMIER,^{2,3} AND THOMAS SÜDMEYER¹ 

¹Laboratoire Temps-Fréquence, Institut de Physique, Université de Neuchâtel, Avenue de Bellevaux 51, 2000 Neuchâtel, Switzerland

²Laboratoire Photonique, Numérique et Nanosciences, UMR 5298, CNRS-IOGS-Université Bordeaux, 33400 Talence, France

³Institut Universitaire de France (IUF), 1 rue Descartes, 75231 Paris, France

*francois.labaye@unine.ch

Abstract: So far, the operation of ultrafast bulk laser oscillators based on Yb-doped gain materials and directly emitting few-cycle pulses have been restricted to low optical-to-optical efficiencies and average output powers of only a few milliwatt. This performance limitation can be attributed to the commonly-applied standard collinear pumping scheme in which the optical pump is transmitted through a dichroic mirror whose spectral transmission and dispersion properties severely perturb the oscillating pulse when its optical spectrum extends towards the pump wavelength. In this study, we report on a novel pumping scheme relying on cross polarization that overcomes this challenge. In our concept, the pump transmitting mirror is highly transmissive for the pump light in p-polarization, while it is highly reflective for the laser light in s-polarization over a broad wavelength range, even covering the pump wavelength and beyond. In contrast to a standard thin-film polarizer featuring similar polarization dependent properties, it provides a low and flat dispersion profile over a broad spectral range for the s-polarization. Implementing this pumping scheme in a soft-aperture Kerr-lens mode-locked bulk laser oscillator based on the gain material Yb:CALGO, we achieve clean 22-fs soliton pulses at 729 mW of average output power and an optical-to-optical efficiency of 25%. In a second configuration optimized for the highest average output power, we demonstrate a high optical-to-optical efficiency of 36.6%, which was obtained for 31-fs pulses at 1.63 W of average output power. In a third configuration we experimentally confirm the limiting effect of a dichroic mirror commonly used in the standard collinear pumping scheme. All the results presented here and obtained in the first and second configuration generate pulses with a center wavelength ranging from 1030 nm to 1056 nm, well within the spectral region of high gain cross sections of Yb:CALGO. While this initial demonstration was realized using a commercial diffraction-limited fiber laser as pump source, the pump geometry appears also well suited for pumping with laser diodes coupled into multimode fibers. This novel approach opens up new opportunities for compact and cost-efficient high-power few-cycle bulk laser oscillators based on Yb-doped gain materials and can be applied to any gain material with small quantum defect.

© 2022 Optica Publishing Group under the terms of the [Optica Open Access Publishing Agreement](#)

1. Introduction

A wide range of applications in biology, medicine and physics strongly benefit from ultrashort pulses. To date, Ti:sapphire based laser systems have usually been the working horse for those applications. Passive mode-locking techniques have been applied to this gain material since the early nineties and have allowed for the generation of few-cycles pulses routinely [1–3]. However, Ti:sapphire suffers from two limitations. First, while cost-effective diode pumping starts to be developed [4,5], Ti:sapphire laser oscillators are still typically optically pumped at 532 nm using

frequency-doubled diode-pumped solid-state lasers operating at 1064 nm, which increases the cost and the complexity of the systems. Second, their relatively high quantum defect limits the optical-to-optical (opt.-to-opt.) efficiency and the average output power due to thermal issues. An alternative are Yb-doped gain materials. Thanks to their excellent thermal and spectral properties [6], combined with the availability of multi-watt pump diodes for those gain materials allowing for cost efficient and more compact systems, they have experienced tremendous successes for more than a decade, allowing to develop laser systems with unprecedented performances (see e.g. [7–9]). Among them, Yb:CaGdAlO₄ (Yb:CALGO) is one of the most promising candidates for delivering ultrashort sub-30-fs pulses at high average output power directly from an ultrafast bulk laser oscillator.

Yb:CALGO is a disordered uniaxial crystal providing a broad emission bandwidth [10–12] combined with comparably good thermal properties [10,13]. Since the first demonstration of a mode-locked laser oscillator based on this gain material in 2006 [11], there have been numerous research developments dedicated to improve its performance, both in terms of average output power and pulse duration. In the standard collinearly-pumped configuration with pulse durations below 100 fs, the highest average output power so far was 12.5 W in 94-fs pulses [14]. Very recently, pulses as short as 17.8 fs have been obtained [15]. This is an outstanding result which further confirms the suitability of Yb:CALGO to deliver few-cycle pulses directly from the output of a bulk laser oscillators based on Yb-doped gain materials (Yb-based laser oscillators). However, the average output power was only 26 mW with an opt.-to-opt. efficiency of 3.3% and the center wavelength of 1118 nm was outside of the favorable gain region centered at about 1050 nm. Additionally, in a standard collinearly-pumped configuration, similar results have been recently obtained using Yb:CaYAlO₄, allowing for 10.4 W in 98-fs pulses [16] and 17-fs pulse duration [17]. However, also here the 17-fs pulses were limited to 18 mW of average output power with an opt.-to-opt. efficiency of only 0.5%.

Typical dichroic mirrors used in collinear pumping [Fig. 1(a), top] are required to have a high transmission for the pump wavelength and a high reflectivity for the laser wavelength. Since the pump and the laser wavelengths are close to each other for gain materials with a low quantum defect, this sets a boundary on the possible spectral expansion towards shorter wavelengths. Additionally, the sharp change in reflectivity between the pump and the laser wavelength also leads to a strongly varying group delay dispersion (GDD) as shown in Fig. 1(b) which further limits the expansion of the optical spectrum towards short wavelengths. This effect was experimentally reported in [18], where the authors demonstrated that such a dichroic mirror forces a red shift of the optical spectrum towards the spectral region where the intra-oscillator negative GDD is more flat. Furthermore, to reach higher power levels, higher output coupling is required, resulting in a stronger population inversion. For common broadband Yb-doped gain materials, this usually shifts the gain maximum towards shorter wavelengths until reaching the spectral edge of the dichroic mirror. This typical gain shift behavior is linked to the quasi-three-level system and the inversion-dependent shape of the gain cross section (see e.g. [12,18,19]). Both reasons set a severe limitation to efficiently exploit the available gain bandwidth for the generation of even shorter pulses and hinder further power scaling of Yb-based bulk laser oscillators in the sub-30-fs regime. Figure 1(c) and Fig. 1(d) show an overview of the opt.-to-opt. efficiency and the average output power versus the pulse duration of bulk laser oscillators based on Yb-doped and Ti:sapphire gain materials. Those plots clearly show that for Yb-based bulk laser oscillators, both parameters significantly drop for pulse durations below 40 fs, while this decrease is not as significant for laser oscillators based on Ti:sapphire for which the opt.-to-opt. efficiency still remains above 10%. For Yb-based bulk laser oscillators, this effect ultimately leads to a trade-off between the pulse duration and the average output power.

So far, there have been a few alternatives attempting to mitigate the spectral limitation of the dichroic mirror. The first one is to combine the effect of self-phase modulation (SPM) with

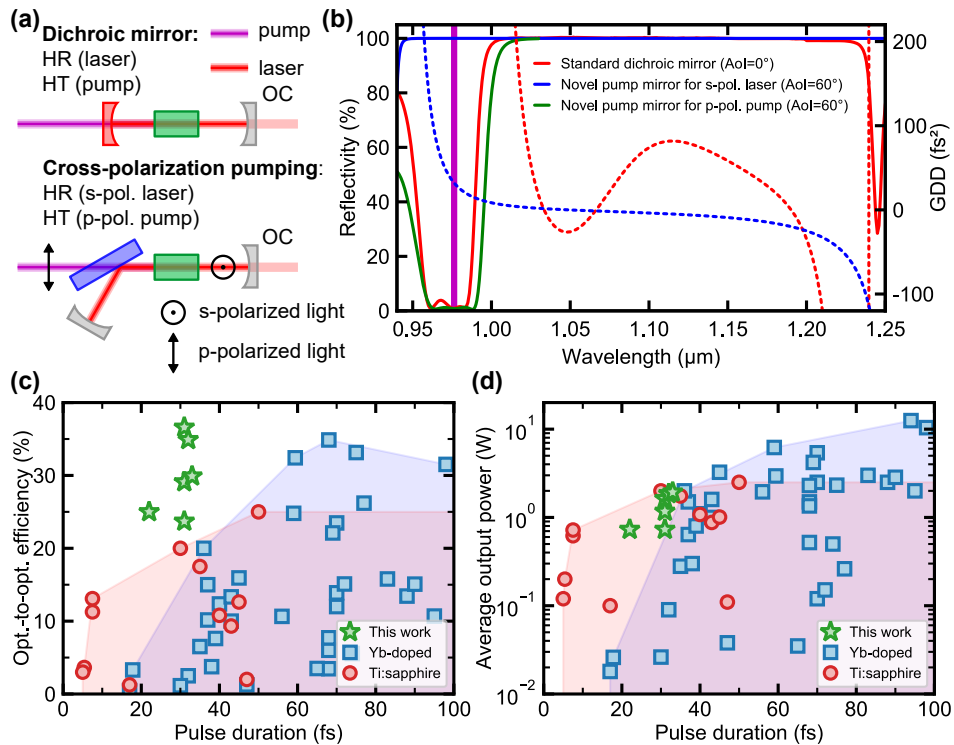


Fig. 1. (a) Schematic of collinear pumping using a standard dichroic mirror (top) and cross-polarization pumping (bottom). (b) Reflectivity (solid lines) and group delay dispersion (dashed lines) of a standard dichroic mirror (red), of the novel pump mirror presented here for a s-polarized laser light (blue) and for a p-polarized pump light (green). The typical wavelength for optical pumping is shown with the purple line. (c) Optical-to-optical efficiency and (d) average output power in function of pulse duration for several bulk laser oscillators based on various Yb-doped gain materials and Ti:sapphire [1,3,11,16–19,24–38]. s-pol.: s-polarization; p-pol.: p-polarization; AoI: angle of incidence; HR: highly reflective; HT: highly transmissive; OC: output coupler.

stimulated Raman scattering in the gain medium. This effect allows to partially Stokes-shift the optical spectrum and to generate additional spectral components further in the infrared. In a Raman-assisted Kerr-lens mode-locked (KLM) laser oscillator, pulses as short as 22 fs have been generated but at the expense of a low average output power of 3 mW and an opt.-to-opt. efficiency of only 0.35% [20]. Furthermore, the widely modulated optical spectrum leads to pulses with low temporal contrast. A second alternative is to use a drilled mirror to direct the pump beam towards the gain crystal [21]. The pump mirror is placed such that the laser beam passes through the hole and therefore the laser cavity and the pump optics do not share any optical component besides the gain medium. A third alternative also decoupling the optical path of the pump beam from the laser beam is the thin-disk geometry. As the pump delivery and the laser cavity share no optics except of the disk, this concept allows for the optimization of the intra-cavity components for shorter pulses independently of the pump wavelength [22]. Very recently, this allowed for the generation of 27-fs pulses at 3.3 W average power from a Kerr-lens mode-locked Yb:YAG thin-disk laser oscillators [23].

In this paper, we report on a novel pump mirror concept relying on cross-polarization pumping [Fig. 1(a), bottom], allowing to bypass the spectral limitation of collinear pumping using standard dichroic mirrors. The developed pump mirror is highly transmissive for the pump light in p-polarization, while it is highly reflective for the laser light in s-polarization over a broad wavelength range, even covering the pump wavelength and beyond [Fig. 1(b)]. In contrast to a standard thin-film polarizer, it provides a low and flat GDD over a broad spectral range for the laser s-polarized light [Fig. 1(b)]. Implementing this mirror in a soft-aperture KLM bulk laser oscillator based on Yb:CALGO, we demonstrate an order of magnitude higher opt.-to-opt. efficiency and the highest average output power of any Yb-based laser oscillators operating in the sub-30-fs pulse duration regime.

2. Experimental setup

The laser oscillator cavity is shown in Fig. 2. A 3-mm-long a-cut anti-reflection coated Yb(3 at.%):CALGO crystal is placed between two concave mirrors (CM1 and CM2) with a 100-mm radius of curvature. The novel pump mirror is placed between the crystal and CM2. The crystal is pumped at a wavelength of 976 nm by a commercial diffraction-limited fiber laser from Azur Light Systems. The p-polarized pump is focused into the gain material through the novel pump mirror under an angle of incidence (AoI) of 60° with a transmission higher than 99%. The Yb:CALGO crystal is optically pumped along its c-axis in p-polarization for maximum pump absorption and the laser operates along its a-axis in s-polarization for highest gain cross section [12]. The pump beam diameter at the crystal position is $\sim 64 \mu\text{m}$. One cavity arm (400-mm long) ends with a dispersive mirror (DM) in a first configuration optimized for the shortest pulse duration (config. 1). In a second configuration optimized for highest average power (config. 2) a highly reflective mirror (HR) replaces the DM. Finally, the latter is exchanged for a standard dichroic mirror in a third configuration to study its effect on the laser performance (config. 3). The other cavity arm (600-mm long) ends with a broadband output coupler (OC). To enforce laser operation in s-polarization, a 1-mm thick fused silica window is placed at Brewster angle with respect to its incidence plane which is perpendicular to the plane of incidence of all the other laser components [Fig. 2]. The SPM in the crystal and the positive GDD from both the gain material and the fused silica window are balanced by four -100 fs^2 DMs ($3 \times$ double-pass and $1 \times$ single-pass per cavity roundtrip) in config. 1 and by two -100 fs^2 DM and two -150 fs^2 DM (one of each in both cavity arms) in config. 2 and config. 3. Except for the anti-reflection coatings on the crystal facets, the optical coatings of every cavity component have been designed and manufactured in our ion-beam-sputtering facility. Soft-aperture Kerr-lens mode-locking is initiated by slightly pushing one cavity end mirror and the pump power is adjusted in each configuration for the maximum average output power, slightly below the appearance of parasitic continuous-wave (cw) lasing oscillations. Two -100 fs^2 DMs are placed in the beam line before characterization to compensate for a positive chirp attributed to the transmission through the OC substrate and the collimating lens in the detection beam line.

For all configurations, the opt.-to-opt. efficiency was calculated using the pump power measured just before the lens focusing the pump beam into the gain material. To determine the unabsorbed pump power in mode-locked operation we placed an additional pump mirror under an AoI of 60° in the output beam line after the OC. The measured transmitted pump power is then corrected by the OC transmission (T_{OC}) and the transmission through the fused silica plate for the pump wavelength and polarization ($T_{\text{BP}} \approx (1-0.127)^2$) was also considered. For the opt.-to-opt. efficiency with respect to the absorbed pump power, we estimated two extreme scenarios in which either all of the pump which was not absorbed during the first pass and reflected by the OC and transmitted by the fused silica plate is absorbed in the gain material or none of it.

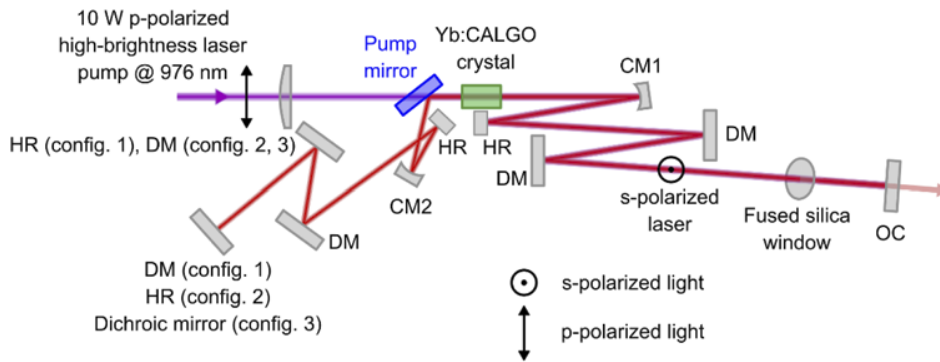


Fig. 2. Experimental setup of the soft-aperture Kerr-lens mode-locked Yb:CALGO laser oscillator implementing our novel cross-polarization pumping approach. Config. 1 enabled the generation of 22-fs pulses at 729 mW of average output power. Config. 2 enabled the highest optical-to-optical efficiency and the highest average output power. Config. 3 was used to demonstrate the limiting effect of a standard dichroic mirror. OC: broadband output coupler; CM: curved mirror; DM: dispersive mirror; HR: highly reflective mirror.

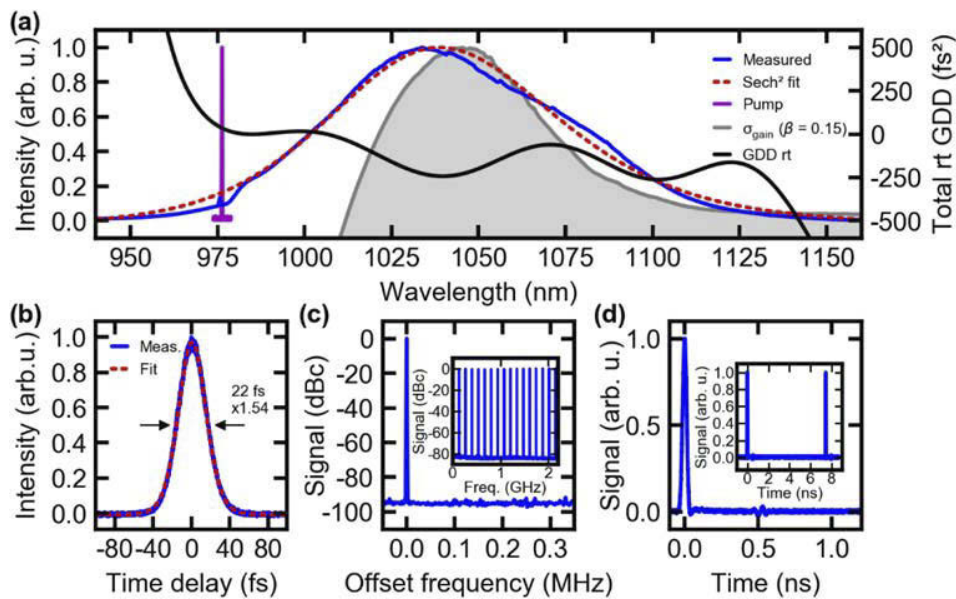


Fig. 3. Characterization of the soft-aperture Kerr-lens mode-locked Yb:CALGO laser oscillator in config. 1 delivering 22-fs pulses at 729 mW of average output power. (a) Measured optical spectrum of the laser (blue) and the pump (purple). The normalized Yb:CALGO gain cross section for an inversion level of $\beta = 0.15$ is shown for reference (left y-axis). Estimated total group delay dispersion per cavity round trip (right y-axis). (b) Intensity autocorrelation trace. (c) Radio-frequency (RF) spectrum of the laser fundamental repetition rate measured with a 10-Hz resolution bandwidth (RBW). Inset: RF spectrum of the higher repetition rate harmonics measured with 100-Hz RBW. (d) 1.2-ns and 9-ns (inset) sampling oscilloscope trace.

3. Experimental results for the shortest pulse duration

In config. 1 optimized for the shortest pulse duration and using a $T_{OC} = 11.5\%$, the laser oscillator delivers an average output power of 729 mW in 22-fs pulses and a peak power of 218 kW at 134 MHz repetition rate with an opt.-to-opt. efficiency of 25%. At the center wavelength of 1041.9 nm, this pulse duration corresponds to 6.4 optical cycles. The optical spectrum has a full width at half maximum (FWHM) bandwidth of 82 nm and extends even beyond the pump wavelength [Fig. 3(a)]. A least-square sech^2 fit shown in comparison agrees well with the expected spectral shape for soliton pulses. A SHG-FROG measurement confirms the generation of almost ideal transform-limited soliton pulses [Fig. 4] and agrees well with an additional intensity autocorrelation measurement [Fig. 3(b)]. The radio-frequency spectra [Fig. 3(c)] shows stable mode-locking operation. Single-pulse operation was confirmed by a 60-ps autocorrelator scan and by observing the pulse train on a 40-GHz sampling oscilloscope with an 18.5-ps-rise-time photodetector [Fig. 3(d)]. Finally, the output beam is of high spatial quality with a measured beam quality factor of $M^2 \leq 1.1$.

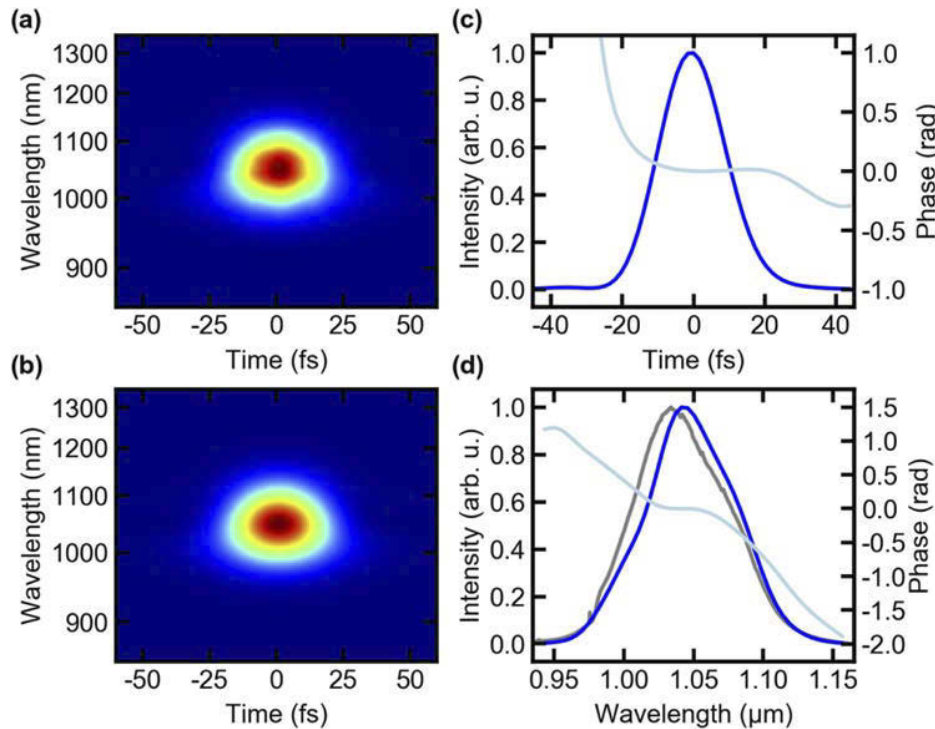


Fig. 4. SHG-FROG characterization of the soft-aperture Kerr-lens mode-locked Yb:CALGO laser oscillator in config. 1 delivering 22-fs pulses at 729 mW of average output power. (a) Experimental and (b) Retrieved SHG-FROG trace. (c) Retrieved intensity profile (blue curve) and temporal phase (light blue curve) of the output pulses. (d) Retrieved (blue curve) and experimental (grey curve) spectra and spectral phase (light blue curve). We attribute the slight discrepancy in wavelength between the measured and retrieved spectra to the reconstruction error in the FROG algorithm combined with the limited accuracy of the FROG spectrometer.

4. Experimental results for the highest average output power

In order to optimize both the average output power and the pulse duration, we studied the laser performance in mode-locked operation for various T_{OC} ranging from 2.4% to 23.0%. In comparison to the shortest pulse configuration, this study was performed with a slightly increased intra-oscillator negative GDD estimated to be ≈ -320 fs² and using a HR mirror as one end mirror [Fig. 2, config. 2]. For each setup, the laser was operated with a pump power just below the threshold for the appearance of parasitic cw lasing oscillations. The obtained results are summarized in Table 1 and shown in Fig. 1(c), Fig. 1(d), and Fig. 5. For each setup, a beam quality factor of $M^2 \leq 1.1$ was measured.

Table 1. Laser performance in mode-locked operation in the three configurations obtained for various output coupler transmissions.^a

T_{OC} (%)	P_{pump} (W)	$P_{unabs.}$ (W)	P_{out} (W)	η (%)	η_{abs} (%)	λ_c (nm)	$\Delta\lambda$ (nm)	$\Delta\nu$ (THz)	$\Delta\tau$ (fs)
Configuration 1									
11.5	2.93	-	0.729	25	-	1040.7	81.6	22.6	22
Configuration 2									
2.4	2.87	0.59–0.25	0.256	8.9	11.2–9.8	1049.3	49.3	13.4	29
4.9	3.10	0.65–0.29	0.520	16.8	21.2–18.5	1047.0	51.4	14.1	29
7.3	3.09	0.71–0.33	0.733	23.7	30.7–26.5	1045.8	48.1	13.2	30
11.5	4.02	1.19–0.58	1.17	29.1	41.3–34.0	1041.8	49.8	13.8	31
16.4	4.45	1.32–0.67	1.63	36.6	51.9–43.1	1040.6	46.7	12.9	31
21.3	5.31	2.06–1.10	1.85	34.9	57.0–44.0	1037.6	43.6	12.2	32
23.0	6.46	2.87–1.57	1.93	29.9	53.8–39.5	1036.7	42.9	12.0	33
Configuration 3									
2.4	2.59	0.54–0.24	0.253	9.8	12.4–10.7	1057.6	46.5	12.5	29
4.9	2.75	0.64–0.28	0.502	18.3	23.8–20.4	1057.4	47.2	12.7	29
7.3	2.88	0.72–0.33	0.651	22.6	30.1–25.6	1054.1	43.9	11.9	31
11.5	3.32	0.94–0.46	1.00	30.1	42.0–34.9	1053.6	38.6	10.4	36
16.4	4.07	1.37–0.70	1.30	31.9	48.1–38.6	1047.8	39.0	10.7	35
21.3	4.18	1.54–0.82	1.40	33.5	53.0–41.7	1043.5	33.8	9.3	39
23.0	5.86	2.80–1.53	1.52	25.9	49.6–35.1	1042.8	34.0	9.4	40

^a T_{OC} : broadband output coupler transmission; P_{pump} : pump power measured just before the lens focusing the pump beam in the gain material; $P_{unabs.}$: pump power that is not absorbed in the first pass through the gain crystal – minimal unabsorbed pump power assuming all the pump light which is guided back to the gain crystal is fully absorbed in the second pass; P_{out} : average output power; η : optical-to-optical efficiency calculated as P_{out}/P_{pump} ; η_{abs} : optical-to-optical efficiency relative to the absorbed pump power and is calculated as $P_{out}/(P_{pump}-P_{unabs.})$. The first value is calculated using the pump power that is not absorbed in the first pass through the gain crystal. The second value is calculated using the minimal unabsorbed pump power assuming all the pump light which is guided back to the gain crystal is fully absorbed in the second pass; λ_c : center wavelength; $\Delta\lambda$ and $\Delta\nu$: FWHM spectral bandwidth; $\Delta\tau$: FWHM pulse duration. The center wavelengths were estimated using the spectra first order momentum to calculate the spectra center of mass.

By optimizing T_{OC} , we achieved watt-level average output power with opt.-to-opt. efficiencies above 25% and pulse durations of around 30 fs. The highest opt.-to-opt. efficiency of 36.6% with an average output power of 1.63 W in 31-fs pulses was obtained for $T_{OC} = 16.4\%$. The highest average output power of 1.93 W in 33-fs pulses with an opt.-to-opt. efficiency of 29.9%, as well as the highest peak power of 385 kW were obtained for $T_{OC} = 23.0\%$. In comparison to previous Yb-based bulk laser oscillators operating at a similar pulse duration [15,17,18,20], the

opt.-to-opt. efficiency and the average output power of the here presented results are more than one order of magnitude higher as depicted in Fig. 1(c) and Fig. 1(d).

From Table 1, Fig. 5(a) and Fig. 5(b), one can observe a blue shift of the optical spectrum when T_{OC} is increased while at the same time the spectral bandwidth decreases. Here, when T_{OC} is increased by almost an order of magnitude from 2.4% to 23.0%, the FWHM spectral bandwidth decreases by 13% from 49.3 nm to 42.9 nm. At the same time, the center wavelength shifts by 12.6 nm from 1049.9 nm to 1036.7 nm. While similar trends have been observed in a previous study using a standard dichroic mirror [18], here it appears less pronounced thanks to our novel pumping scheme. However, to unambiguously demonstrate the benefit of our novel pumping scheme, it is important to study the effect of a standard dichroic mirror in the same laser oscillator.

5. Limiting impact of a standard dichroic mirror

To demonstrate more clearly the limiting effect of a standard dichroic mirror, we modified our laser cavity by replacing the (HR) cavity end mirror with a standard dichroic mirror keeping the same cavity geometry and mirror positions [Fig. 2, config. 3]. Then we repeated the previous study with the same T_{OC} . For each setup, the laser was again operated with a pump power just below the threshold for the appearance of parasitic cw lasing oscillations and the beam quality factor remained very good with a measured $M^2 \leq 1.1$. Overall, we can observe in this second study the same trends as in the previous one but more clearly pronounced [Table 1 and Fig. 5]. With a dichroic mirror in the cavity, the achievable FWHM spectral bandwidth is narrower and decreases when T_{OC} is increased. With $T_{OC} = 2.4\%$ the FWHM spectral bandwidth is 6% narrower when a dichroic mirror is inserted. Then, when T_{OC} is increased from 2.4% to 23.0%, the FWHM spectral bandwidth decreases by 27% from 46.5 nm to 34.0 nm, twice as much as the previous configuration without dichroic mirror [Fig. 5(a)]. This inherently leads to an increase in the pulse duration [Fig. 5(c)]. Additionally, on average, the center wavelength is shifted by about 8 nm towards longer wavelengths [Fig. 5(b)].

A similar discrepancy is observed with the average output power. While with $T_{OC} = 2.4\%$ the average output power is only 1% lower when the dichroic mirror is inserted, this difference increases with T_{OC} and the average output power significantly drops by 21% for $T_{OC} = 23.0\%$ [Fig. 5(d)]. In the configuration enabling the highest average power, again reached for $T_{OC} = 23.0\%$, the dichroic mirror limits the pulse duration to 40 fs while, 33 fs was achieved without dichroic mirror in config. 2 [Fig. 5(c)].

These observations can be explained by the shift of the gain cross section towards shorter wavelengths with higher inversion level [12], as it is the case with higher T_{OC} . This leads to a shift of the optical spectrum towards the shorter wavelengths [Fig. 5(b)]. However, the lower reflectivity and the rising GDD of the dichroic mirror around 1 μm limit this spectral shift and can additionally give rise to a pedestal on the short wavelength side of the optical spectrum [Fig. 5(e) and Fig. 5(f)]. Eventually, these effects lead to a decrease in the maximum achievable average output power with ultrashort pulses for higher T_{OC} because the optical spectrum cannot follow the maximum of the gain cross section which shifts towards shorter wavelengths with increased inversion level [Fig. 5(d)]. Ultimately the dichroic mirror can be clearly identified as the limiting cavity component for achieving higher average output powers and opt.-to-opt. efficiencies with shorter pulse durations. Our study demonstrates unambiguously the strong benefit of our cross-polarization pumping approach compared to using a standard dichroic mirror to generate ultrashort pulses with high opt.-to-opt. efficiencies and high average output power from Yb-based bulk laser oscillators at a center wavelength between 1030 nm and 1050 nm, corresponding to the bandwidth where the gain cross section is the highest.

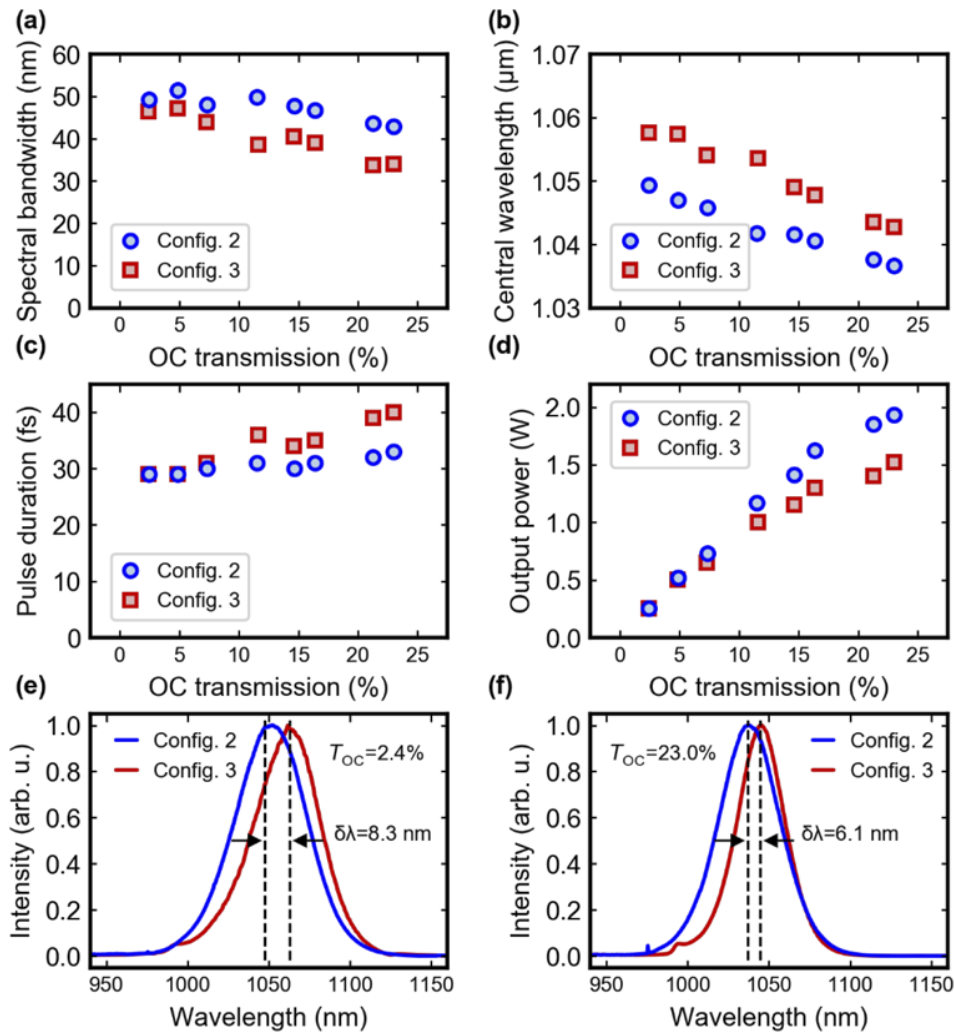


Fig. 5. Evolution of the spectral bandwidth (a), center wavelength (b), pulse duration (c) and average output power of the pulses delivered by the laser oscillator with (config. 3, red) and without (config. 2, blue) dichroic mirror. (d) Optical spectra with $T_{OC} = 2.4\%$ (e) and $T_{OC} = 23.0\%$ (f) in the absence (config. 2, blue) or presence (config. 3, red) of a standard dichroic mirror. $\delta\lambda$ shows the difference between the central wavelengths of both configurations.

6. Conclusion

In conclusion, we have presented a simple and effective way to by-pass previous limitations in the achievable spectral bandwidth of Yb-based bulk laser oscillators. By using a novel pump mirror design based on cross-polarization pumping which allows laser operation where the lasing wavelength overlaps the pump wavelength, we were able to mitigate the previous limitations on the possible spectral expansion towards shorter wavelengths. We have implemented this mirror in a soft-aperture KLM Yb:CALGO laser oscillator and obtained record high opt.-to-opt. efficiencies for sub-50-fs laser oscillators. We believe that this technique can be implemented for any gain material where the quantum defect is small. Furthermore, our pump source operated

only at a wavelength of 976 nm. Yb:CALGO presents a ≈ 1.7 times higher maximal absorption cross section at a wavelength of 980 nm. Therefore, optical pumping at this wavelength should allow for a further increased opt.-to-opt. efficiency of the system, as indicated by the significant amount of unabsorbed pump power in some configurations. Finally, while the results presented here have been obtained using a high brightness fiber laser as pump source, both soft (see e.g. [16,32,37]) and hard (see e.g. [36,39,40]) aperture KLM have been reported using multimode pump diodes with lower brightness and we believe that using those will allow for cost efficient multi-watt few-cycle laser oscillators.

Funding. Schweizerischer Nationalfonds zur Förderung der Wissenschaftlichen Forschung (200020_179146/1, 200021_200774, R'Equip 206021_198176, SPARK CRSK-2_190593); Institut Universitaire de France.

Disclosures. The authors declare that there are no conflicts of interest related to this article.

Data availability. Data underlying the results presented in this paper are available in Ref. [41].

References

- U. Morgner, F. X. Kärtner, S. H. Cho, Y. Chen, H. A. Haus, J. G. Fujimoto, E. P. Ippen, V. Scheuer, G. Angelow, and T. Tschudi, "Sub-two-cycle pulses from a Kerr-lens mode-locked Ti:sapphire laser," *Opt. Lett.* **24**(6), 411–413 (1999).
- D. H. Sutter, G. Steinmeyer, L. Gallmann, N. Matuschek, F. Morier-Genoud, U. Keller, V. Scheuer, G. Angelow, and T. Tschudi, "Semiconductor saturable-absorber mirror-assisted Kerr-lens mode-locked Ti:sapphire laser producing pulses in the two-cycle regime," *Opt. Lett.* **24**(9), 631–633 (1999).
- R. Ell, U. Morgner, F. X. Kärtner, J. G. Fujimoto, E. P. Ippen, V. Scheuer, G. Angelow, T. Tschudi, M. J. Lederer, A. Boiko, and B. Luther-Davies, "Generation of 5-fs pulses and octave-spanning spectra directly from a Ti:sapphire laser," *Opt. Lett.* **26**(6), 373–375 (2001).
- K. Gürel, V. J. Wittwer, M. Hoffmann, C. J. Saraceno, S. Hakobyan, B. Resan, A. Rohrbacher, K. Weingarten, S. Schilt, and T. Südmeyer, "Green-diode-pumped femtosecond Ti:Sapphire laser with up to 450 mW average power," *Opt. Express* **23**(23), 30043–30048 (2015).
- S. Backus, M. Kirchner, C. Durfee, M. Murnane, and H. Kapteyn, "Direct diode-pumped Kerr Lens 13 fs Ti:sapphire ultrafast oscillator using a single blue laser diode," *Opt. Express* **25**(11), 12469–12477 (2017).
- F. Druon, F. Balembois, and P. Georges, "New Materials for Short-Pulse Amplifiers," *IEEE Photonics J.* **3**(2), 268–273 (2011).
- H. Fattahi, H. G. Barros, M. Gorjan, T. Nubbemeyer, B. Alsaif, C. Y. Teisset, M. Schultze, S. Prinz, M. Haefner, M. Ueffing, A. Alismail, L. Vámos, A. Schwarz, O. Pronin, J. Brons, X. T. Geng, G. Arisholm, M. Ciappina, V. S. Yakovlev, D.-E. Kim, A. M. Azzeeer, N. Karpowicz, D. Sutter, Z. Major, T. Metzger, and F. Krausz, "Third-generation femtosecond technology," *Optica* **1**(1), 45 (2014).
- T. Nubbemeyer, M. Kaumanns, M. Ueffing, M. Gorjan, A. Alismail, H. Fattahi, J. Brons, O. Pronin, H. G. Barros, Z. Major, T. Metzger, D. Sutter, and F. Krausz, "1 kW, 200 mJ picosecond thin-disk laser system," *Opt. Lett.* **42**(7), 1381–1384 (2017).
- M. Müller, C. Aleshire, A. Klenke, E. Haddad, F. Légaré, A. Tünnermann, and J. Limpert, "10.4 kW coherently combined ultrafast fiber laser," *Opt. Lett.* **45**(11), 3083–3086 (2020).
- J. Petit, P. Goldner, and B. Viana, "Laser emission with low quantum defect in Yb:CaGdAlO₄," *Opt. Lett.* **30**(11), 1345–1347 (2005).
- Y. Zaouter, J. Didierjean, F. Balembois, G. L. Leclin, F. Druon, P. Georges, J. Petit, P. Goldner, and B. Viana, "47-fs diode-pumped Yb³⁺:CaGdAlO₄ laser," *Opt. Lett.* **31**(1), 119–121 (2006).
- K. Hasse, T. Calmano, B. Deppe, C. Liebald, and C. Kränkel, "Efficient Yb³⁺:CaGdAlO₄ bulk and femtosecond-laser-written waveguide lasers," *Opt. Lett.* **40**(15), 3552–3555 (2015).
- P. Loiko, F. Druon, P. Georges, B. Viana, and K. Yumashev, "Thermo-optic characterization of Yb:CaGdAlO₄ laser crystal," *Opt. Mater. Express* **4**(11), 2241–2249 (2014).
- A. Greborio, A. Guandalini, and J. Aus der Au, "Sub-100 fs pulses with 12.5-W from Yb:CALGO based oscillators," *Proc. SPIE* **8235**, 823511 (2012).
- Y. Wang, X. Su, Y. Xie, F. Gao, S. Kumar, Q. Wang, C. Liu, B. Zhang, B. Zhang, and J. He, "17.8 fs broadband Kerr-lens mode-locked Yb:CALGO oscillator," *Opt. Lett.* **46**(8), 1892–1895 (2021).
- W. Tian, R. Xu, L. Zheng, X. Tian, D. Zhang, X. Xu, J. Zhu, J. Xu, and Z. Wei, "10-W-scale Kerr-lens mode-locked Yb:CALYO laser with sub-100-fs pulses," *Opt. Lett.* **46**(6), 1297–1300 (2021).
- J. Ma, F. Yang, W. Gao, X. Xiaodong, X. Jun, D. Shen, and D. Tang, "Sub-five-optical-cycle pulse generation from a Kerr-lens mode-locked Yb:CaYAlO₄ laser," *Opt. Lett.* **46**(10), 2328–2331 (2021).
- P. Sévillano, P. Georges, F. Druon, D. Descamps, and E. Cormier, "32-fs Kerr-lens mode-locked Yb:CaGdAlO₄ oscillator optically pumped by a bright fiber laser," *Opt. Lett.* **39**(20), 6001–6004 (2014).
- J. Boudeile, F. Druon, M. Hanna, P. Georges, Y. Zaouter, E. Cormier, J. Petit, P. Goldner, and B. Viana, "Continuous-wave and femtosecond laser operation of Yb:CaGdAlO₄ under high-power diode pumping," *Opt. Lett.* **32**(14), 1962–1964 (2007).
- S. Kimura, S. Tani, and Y. Kobayashi, "Raman-assisted broadband mode-locked laser," *Sci. Rep.* **9**(1), 3738 (2019).

21. V. E. Kisel, A. S. Rudenkov, A. A. Pavlyuk, A. A. Kovalyov, V. V. Preobrazhenskii, M. A. Putyato, N. N. Rubtsova, B. R. Semyagin, and N. V. Kuleshov, "High-power, efficient, semiconductor saturable absorber mode-locked Yb:KGW bulk laser," *Opt. Lett.* **40**(12), 2707–2710 (2015).
22. N. Modsching, C. Paradis, F. Labaye, M. Gaponenko, I. J. Graumann, A. Diebold, F. Emaury, V. J. Wittwer, and T. Südmeyer, "Kerr lens mode-locked Yb:CALGO thin-disk laser," *Opt. Lett.* **43**(4), 879–882 (2018).
23. J. Drs, J. Fischer, N. Modsching, F. Labaye, V. J. Wittwer, and T. Südmeyer, "Sub-30-fs Yb:YAG thin-disk laser oscillator operating in the strongly self-phase modulation broadened regime," *Opt. Express* **29**(22), 35929–35937 (2021).
24. N. H. Rizvi, P. M. W. French, and J. R. Taylor, "Continuously self-mode-locked Ti:sapphire laser that produces sub-50-fs pulses," *Opt. Lett.* **17**(4), 279–281 (1992).
25. L. Xu, G. Tempea, A. Poppe, M. Lenzner, C. Spielmann, F. Krausz, A. Stingl, and K. Ferencz, "High-power sub-10-fs Ti:sapphire oscillators," *Appl. Phys. B* **65**(2), 151–159 (1997).
26. A. M. Kowalevicz Jr., A. T. Zare, F. X. Kärtner, J. G. Fujimoto, S. Dewald, U. Morgner, V. Scheuer, and G. Angelow, "Generation of 150-nJ pulses from a multiple-pass cavity Kerr-lens mode-locked Ti:Al₂O₃ oscillator," *Opt. Lett.* **28**(17), 1597–1599 (2003).
27. S. Naumov, A. Fernandez, R. Graf, P. Dombi, F. Krausz, and A. Apolonski, "Approaching the microjoule frontier with femtosecond laser oscillators," *New J. Phys.* **7**, 216 (2005).
28. S. Uemura and K. Torizuka, "Sub-40-fs Pulses from a Diode-Pumped Kerr-Lens Mode-Locked Yb-Doped Yttrium Aluminum Garnet Laser," *Jpn. J. Appl. Phys.* **50**, 010201 (2011).
29. E. Seres, J. Seres, and C. Spielmann, "Extreme ultraviolet light source based on intracavity high harmonic generation in a mode locked Ti:sapphire oscillator with 9.4 MHz repetition rate," *Opt. Express* **20**(6), 6185–6190 (2012).
30. G. Machinet, P. Sevillano, F. Guichard, R. Dubrasquet, P. Camy, J.-L. Doualan, R. Moncorgé, P. Georges, F. Druon, D. Descamps, and E. Cormier, "High-brightness fiber laser-pumped 68 fs–23 W Kerr-lens mode-locked Yb:CaF₂ oscillator," *Opt. Lett.* **38**(20), 4008–4010 (2013).
31. A. Klenner, M. Golling, and U. Keller, "High peak power gigahertz Yb:CALGO laser," *Opt. Express* **22**(10), 11884–11891 (2014).
32. R. Akbari and A. Major, "High-power diode-pumped Kerr-lens mode-locked bulk Yb:KGW laser," *Appl. Opt.* **56**(31), 8838–8844 (2017).
33. R. Akbari, K. A. Fedorova, E. U. Rafailov, and A. Major, "Diode-pumped ultrafast Yb:KGW laser with 56 fs pulses and multi-100 kW peak power based on SESAM and Kerr-lens mode locking," *Appl. Phys. B* **123**(4), 123 (2017).
34. M. Kowalczyk, A. Major, and J. Sotor, "High peak power ultrafast Yb:CaF₂ oscillator pumped by a single-mode fiber-coupled laser diode," *Opt. Express* **25**(21), 26289–26295 (2017).
35. S. Manjooan and A. Major, "Diode-pumped 45 fs Yb:CALGO laser oscillator with 1.7 MW of peak power," *Opt. Lett.* **43**(10), 2324–2327 (2018).
36. W. Tian, Y. Peng, Z. Zhang, Z. Yu, J. Zhu, X. Xu, and Z. Wei, "Diode-pumped power scalable Kerr-lens mode-locked Yb:CYA laser," *Photonics Res.* **6**(2), 127–131 (2018).
37. R. Akbari and A. Major, "Kerr-lens mode locking of a diode-pumped Yb:KGW laser using an additional intracavity Kerr medium," *Laser Phys. Lett.* **15**(8), 085001 (2018).
38. W. Tian, C. Yu, J. Zhu, D. Zhang, Z. Wei, X. Xu, and J. Xu, "Diode-pumped high-power sub-100 fs Kerr-lens mode-locked Yb:CaYAlO₄ laser with 1.85 MW peak power," *Opt. Express* **27**(15), 21448–21454 (2019).
39. H. Liu, J. Nees, and G. Mourou, "Diode-pumped Kerr-lens mode-locked Yb:KY(WO₄)₂ laser," *Opt. Lett.* **26**(21), 1723–1725 (2001).
40. T. Ishikawa, A. A. Eilanlou, Y. Nabekawa, Y. Fujihira, T. Imahoko, T. Sumiyoshi, F. Kannari, M. Kuwata-Gonokami, and K. Midorikawa, "Kerr lens mode-locked Yb:Lu₂O₃ bulk ceramic oscillator pumped by a multimode laser diode," *Jpn. J. Appl. Phys.* **54**(7), 072703 (2015).
41. F. Labaye, "Efficient few-cycle Yb-doped laser oscillator with Watt-level average power," EUDAT (2021), <https://b2share.eudat.eu/records/b97841e33796483aacb76753741ae1ce>.

2.4 Chapter conclusion

In this first chapter, I have presented the development of a broadband, powerful OFC source with 1-GHz comb line spacing. This work was divided in two steps. First we developed an ultrafast Yb:CALGO laser oscillator operating at 1 GHz of repetition rate, and second we achieved its full stabilization. The resulting OFC source delivers 50-fs pulses with 2.5 W of average power and 50 kW peak power available for applications. Typically, such power levels allow straightforward up- or down-frequency conversion towards UV or MIR wavelength ranges, respectively. A part of this work was dedicated to develop a highly functional, robust and stable version of the laser source, which can be reliably reproduced and used out of the laboratory. The final source represents a real step towards the realization of cost-efficient and commercially available powerful low-noise OFC.

In the last section of this chapter, we addressed the challenge of generating few-cycle pulses at high optical-to-optical efficiency using Yb-based gain materials. We successfully implemented a novel pumping scheme that circumvents the limitations due to the low quantum defect and allows more efficient generation of spectral components beyond the pump wavelength. This approach enables efficient pumping of the crystal and operation in a spectral region where the gain cross-section is the highest, in contrast to previous approaches demonstrating few-cycle pulses. Follow-up works have been made to develop this new concept with a cost-efficient and powerful pump diode, which is crucial for potential replication of the laser and real-world applications.

References

- [1] N. Picqué and T. W. Hänsch, “Frequency comb spectroscopy”, *Nature Photonics* **13**, 146 (2019).
- [2] S. A. Diddams, K. Vahala, and T. Udem, “Optical frequency combs: Coherently uniting the electromagnetic spectrum”, *Science* **369**, eaay3676 (2020).
- [3] T. Fortier and E. Baumann, “20 years of developments in optical frequency comb technology and applications”, *Communications Physics* **2**, 153 (2019).
- [4] A. Klenner, M. Golling, and U. Keller, “A gigahertz multimode-diode-pumped Yb: KGW enables a strong frequency comb offset beat signal”, *Optics express* **21**, 10351 (2013).

- [5] A. Klenner, M. Golling, and U. Keller, “High peak power gigahertz Yb: CALGO laser”, *Optics Express* **22**, 11884 (2014).
- [6] S. Hakobyan, V. J. Wittwer, P. Brochard, K. Gürel, S. Schilt, A. S. Mayer, U. Keller, and T. Südmeyer, “Full stabilization and characterization of an optical frequency comb from a diode-pumped solid-state laser with GHz repetition rate”, *Optics Express* **25**, 20437 (2017).
- [7] L. M. Krüger, A. S. Mayer, Y. Okawachi, X. Ji, A. Klenner, A. R. Johnson, C. Langrock, M. M. Fejer, M. Lipson, A. L. Gaeta, et al., “Performance scaling of a 10-GHz solid-state laser enabling self-referenced CEO frequency detection without amplification”, *Optics Express* **28**, 12755 (2020).
- [8] A. Bartels and H. Kurz, “Generation of a broadband continuum by a Ti: sapphire femtosecond oscillator with a 1-GHz repetition rate”, *Optics letters* **27**, 1839 (2002).
- [9] S. Pekarek, C. Fiebig, M. C. Stumpf, A. E. H. Oehler, K. Paschke, G. Erbert, T. Südmeyer, and U. Keller, “Diode-pumped gigahertz femtosecond Yb: KGW laser with a peak power of 3.9 kW”, *Optics express* **18**, 16320 (2010).
- [10] S. Pekarek, T. Südmeyer, S. Lecomte, S. Kundermann, J. M. Dudley, and U. Keller, “Self-referenceable frequency comb from a gigahertz diode-pumped solid-state laser”, *Optics express* **19**, 16491 (2011).
- [11] A. Klenner and U. Keller, “All-optical Q-switching limiter for high-power gigahertz modelocked diode-pumped solid-state lasers”, *Optics Express* **23**, 8532 (2015).
- [12] L. Zheng, W. Tian, H. Liu, G. Wang, C. Bai, R. Xu, D. Zhang, H. Han, J. Zhu, and Z. Wei, “2-GHz watt-level Kerr-lens mode-locked Yb: KGW laser”, *Optics Express* **29**, 12950 (2021).
- [13] Y. Zaouter, J. Didierjean, F. Balembois, G. L. Leclin, F. Druon, P. Georges, J. Petit, P. Goldner, and B. Viana, “47-fs diode-pumped Yb 3+: CaGdAlO₄ laser”, *Optics letters* **31**, 119 (2006).
- [14] K. Hasse, T. Calmano, B. Deppe, C. Liebald, and C. Kränkel, “Efficient Yb 3+: CaGdAlO₄ bulk and femtosecond-laser-written waveguide lasers”, *Optics letters* **40**, 3552 (2015).
- [15] J. Petit, P. Goldner, and B. Viana, “Laser emission with low quantum defect in Yb: CaGdAlO₄”, *Optics letters* **30**, 1345 (2005).
- [16] P. Loiko, F. Druon, P. Georges, B. Viana, and K. Yumashev, “Thermo-optic characterization of Yb: CaGdAlO₄ laser crystal”, *Optical Materials Express* **4**, 2241 (2014).

- [17] M. Hamrouni, F. Labaye, N. Modsching, V. J. Wittwer, and T. Südmeyer, “Efficient high-power sub-50-fs gigahertz repetition rate diode-pumped solid-state laser”, *Optics Express* **30**, 30012 (2022).
- [18] S. Hakobyan, V. J. Wittwer, K. Gürel, A. S. Mayer, S. Schilt, and T. Südmeyer, “Carrier-envelope offset stabilization of a GHz repetition rate femtosecond laser using opto-optical modulation of a SESAM”, *Optics Letters* **42**, 4651 (2017).
- [19] G. Di Domenico, S. Schilt, and P. Thomann, “Simple approach to the relation between laser frequency noise and laser line shape”, *Applied optics* **49**, 4801 (2010).
- [20] A. Schlatter, S. C. Zeller, R. Grange, R. Paschotta, and U. Keller, “Pulse-energy dynamics of passively mode-locked solid-state lasers above the Q-switching threshold”, *JOSA B* **21**, 1469 (2004).
- [21] R. Paschotta, H. R. Telle, and U. Keller, in *Solid-State Lasers and Applications* (CRC Press, 2017), pp. 473–510.
- [22] A. Greborio, A. Guandalini, and J. A. der Au, “Sub-100 fs pulses with 12.5-W from Yb: CALGO based oscillators”, in *Solid State Lasers XXI: Technology and Devices*, Vol. 8235 (SPIE, 2012), pp. 200–205.
- [23] W. Tian, R. Xu, L. Zheng, X. Tian, D. Zhang, X. Xu, J. Zhu, J. Xu, and Z. Wei, “10-W-scale Kerr-lens mode-locked Yb: CALYO laser with sub-100-fs pulses”, *Optics Letters* **46**, 1297 (2021).
- [24] J. Ma, F. Yang, W. Gao, X. Xiaodong, X. Jun, D. Shen, and D. Tang, “Sub-five-optical-cycle pulse generation from a Kerr-lens mode-locked Yb: CaYAlO₄ laser”, *Optics Letters* **46**, 2328 (2021).
- [25] Y. Wang, X. Su, Y. Xie, F. Gao, S. Kumar, Q. Wang, C. Liu, B. Zhang, B. Zhang, and J. He, “17.8 fs broadband Kerr-lens mode-locked Yb: CALGO oscillator”, *Optics Letters* **46**, 1892 (2021).
- [26] R. Ell, U. Morgner, F. X. Kärtner, J. G. Fujimoto, E. P. Ippen, V. Scheuer, G. Angelow, T. Tschudi, M. J. Lederer, A. Boiko, et al., “Generation of 5-fs pulses and octave-spanning spectra directly from a Ti: sapphire laser”, *Optics letters* **26**, 373 (2001).
- [27] F. Kärtner, U. Morgner, R. Ell, T. Schibli, J. Fujimoto, E. Ippen, V. Scheuer, G. Angelow, and T. Tschudi, “Ultrabroadband double-chirped mirror pairs for generation of octave spectra”, *JOSA B* **18**, 882 (2001).
- [28] K. Fritsch, M. Poetzlberger, V. Pervak, J. Brons, and O. Pronin, “All-solid-state multipass spectral broadening to sub-20 fs”, *Optics letters* **43**, 4643 (2018).

- [29] P. Balla, A. B. Wahid, I. Sytceвич, C. Guo, A.-L. Viotti, L. Silletti, A. Cartella, S. Alisauskas, H. Tavakol, U. Grosse-Wortmann, et al., “Postcompression of picosecond pulses into the few-cycle regime”, *Optics letters* **45**, 2572 (2020).
- [30] M. Müller, J. Buldt, H. Stark, C. Grebing, and J. Limpert, “Multipass cell for high-power few-cycle compression”, *Optics Letters* **46**, 2678 (2021).

Chapter 3

Towards low-power efficient nonlinear frequency conversion

As discussed in the thesis introduction, while mode-locked laser oscillators stand as the most mature technology for generating OFCs, their spectral versatility is inherently limited by the properties of the gain material. So far, most of the gain media used to realize ultrafast lasers are limited to visible and near-infrared regions. Although recent advances, such as the development of thulium-, holmium- or chromium-based gain materials, have extended these boundaries to the short-wavelength side of the MIR, slightly above $\sim 3 \mu\text{m}$ [1], today directly generating OFCs beyond these wavelengths remains technologically challenging. This limitation is particularly prohibitive in spectroscopy where many applications involve interrogating molecular transitions located from mid-infrared to terahertz frequency regions.

To overcome these limitations, a common approach is to down-convert near-infrared pulses delivered by mode-locked lasers via nonlinear frequency conversion. As mentioned in the introduction and discussed in more details in this section, nonlinear frequency conversion features its own set of challenges. The driving power levels required to realize efficient frequency conversion are often not straightforward to achieve, imposing stringent requirements on the initial laser source. Secondly, in traditional methods, which employ bulk crystals or weakly-confining waveguides as nonlinear media, the bandwidth of the nonlinear process is limited by the dispersion of the material. As a result, while Yb-based mode-locked laser oscillators can routinely produce sub-100-fs pulses, achieving efficient nonlinear conversion across the corresponding spectral bandwidth is still challenging.

The work presented in this chapter focuses on revisiting different nonlinear approaches for efficient frequency conversion with reduced power requirements. In a first work, I report on efficient and broadband terahertz generation obtained by driving frequency conversion directly inside the cavity of a powerful and ultrafast Yb:CALGO laser oscillator. This approach differs from conventional methods that typically drive the frequency conversion at the laser output. In the article we show that our method reduces the stringent requirements placed on the overall pump system.

The second and third section build on the recent progress of thin-film lithium niobate technologies. In the second experiment, we present a new approach for efficient and broadband mid-infrared generation with unprecedented low power requirements. We drive optical parametric amplification inside TFLN nanophotonic waveguides. Besides enabling large field intensities, the confinement of the light in extremely small volumes offers the freedom to engineer the dispersion of the waveguide modes. In this work, we leverage this advantage to operate the OPA in a regime where the nonlinear interaction lengths and conversion bandwidths are no longer limited by the natural dispersion of the nonlinear material. Our approach demonstrates efficient and broadband frequency conversion in the 3-4 μm region, consuming only picojoules of on-chip pump-pulse energy.

In the last section, we further leverage the potential offered by this nanophotonic platform to generate coherent and broadband supercontinuum with a power requirement two to three orders of magnitude smaller than traditional fiber-based methods. In addition, we show that our approach to supercontinuum generation is compatible with on-chip f_{CEO} detection, enabling to drastically simplify conventional f-to-2f methods by replacing complicated, bulky, and power-hungry systems with a single chip.

3.1 Intra-oscillator broadband THz generation in a compact ultrafast diode-pumped solid-state laser

Frequency comb sources directly emitting in the terahertz region are not mature. While terahertz quantum cascade lasers hold promise for compact, versatile, and high-power sources [2–4], the main approach is still to down-convert near infrared pulses from mature mode-locked lasers into the terahertz domain. For this, different nonlinear approaches such as optical rectification [5, 6], difference frequency generation [7, 8] and plasma-based generation [9–11] have been proposed. However, the near-infrared to terahertz conversion efficiency rarely

exceeds 1%, which imposes high requirements on the driving power levels. Here again, Ti:sapphire laser systems have long remained the key enabling driver of terahertz radiation [12]. While these systems are capable of delivering high peak power and energetic pulses, they are typically not suitable for operating at high average power and large repetition rates, which is prohibitive for applications requiring sufficient driving power levels and fast measurements. For instance, the lack of average power often prevents the study of biological samples due to the strong absorption of water in the terahertz domain, limiting interesting possibilities in medical imaging or diagnostics [13, 14]. The development of table-top Ytterbium systems combining high power levels at megahertz repetition rates rather than kilohertz and short pulse durations appeared as appealing drivers for terahertz generation [15, 16]. For instance, Yb-based thin-disk laser oscillators, which are capable of delivering tens of watts of average power and sub-100-fs pulses at megahertz repetition rates [17], have been used to realize milliwatt-class broadband terahertz sources [18, 19]. Although this new class of lasers opened a route towards the realization of powerful and compact terahertz sources, their size and complexity may remain still prohibitive for real-world applications that require embedded sources. In this section, we propose a solution to overcome these limitations and demonstrate high terahertz performances based on a compact and cost-efficient ultrafast laser driver.

3.1.1 Article outline

Context

Frequency shifting light from Yb-based lasers (around 1 μm) to the terahertz range suffers from low conversion efficiencies that rarely exceed a few percents. Terahertz sources based on plasmonic-enhanced photoconductive antennas [20, 21] and organic crystals [22, 23] are among the most efficient technologies and can demonstrate milliwatt-class broadband terahertz generation from moderate pump power levels of only a few watts. Another approach is frequency conversion in conventional $\chi^{(2)}$ nonlinear crystals such as LN, GaP, GaAs, ZnTe, etc. While those emitters are less efficient than plasmonic antennas and organic crystals, they feature much higher damage thresholds. Thus, it is possible to operate with high pump power levels and generate powerful THz radiation despite the low conversion efficiency. In this direction, Yb-based thin-disk lasers emerged as promising table-top drivers for powerful terahertz generation [16, 18, 19]. For instance, in [19], driving optical rectification in a LN crystal with more than 100 W of average power (30 MW peak power) from a post-compressed thin-disk laser, the authors achieve a record-high terahertz average power of 66 mW. However, such sources are rather complex and expensive, and may require operation

in vacuum. Put together, these disadvantages have so far precluded their usage out of the laboratory.

In this paper, we propose a new approach consisting of driving the frequency conversion directly inside an ultrafast DPSSL based on a bulk gain material. While the output peak power delivered by bulk-based Yb-doped laser oscillators is typically limited to a few hundred kilowatts, it can easily reach a few megawatts inside the cavity. In fact, most of the Yb-based bulk sources reported in the overview Figure 2.7 (section 2.3.2) demonstrate intra-cavity peak power in excess of 1 MW. Here, we harness the high power levels available inside the cavity of a home-built Yb:CALGO bulk laser oscillator to demonstrate efficient and broadband terahertz generation via optical rectification.

Results

A comprehensive description of the driving laser source is written in the published article (section 3.1.4). The laser oscillator is based on an Yb:CALGO crystal pumped at 980 nm by a commercially-available multimode laser diode. The pump beam is coupled inside the cavity using a regular dichroic mirror. An output coupler with a transmission of 1.5% is placed as a folding mirror, thus providing two out-coupled beams for near-infrared and terahertz diagnostics. The terahertz emitter is an anti-reflection coated GaP crystal placed inside the cavity. The generated terahertz radiation is collected and sent to detection by an off-axis parabolic mirror placed inside the cavity. A small hole was drilled in the center of the parabola so that its presence in the cavity does not affect the laser beam.

The laser is operated in two configurations, optimized for either high terahertz average power or broad spectral bandwidths. For both configurations, the pump power is set to ~ 7 W, which results in an intra-cavity average power of approximately 20 W. In the first configuration, we drive a 0.3-mm-thick GaP crystal with 105-fs pulses, leading to 150 μ W of terahertz average power within a 5.5 THz spectral bandwidth. In the second configuration, the driving pulse duration is decreased to sub-50 fs to allow broader terahertz spectral bandwidths. Accordingly, the thickness of the GaP crystal is reduced to extend the phase-matching bandwidth [24]. Using a 0.1-mm-thick GaP, we generate a broad spectral bandwidth extending up to 7 THz, at the expense of the generated power that reduces to 35 μ W.

Conclusion

In summary, this work shows a technique to realize powerful and broadband terahertz sources based on a simple DPSSL oscillator. The stringent requirement placed on typical driving sources is alleviated by operating the frequency

3.1. Intra-oscillator broadband THz generation in a compact ultrafast diode-pumped solid-state laser

conversion inside the oscillator. To compare, we achieve terahertz performances similar to that reported in [18, 24], where the output from an expensive thin-disk laser is used to drive optical rectification.

3.1.2 Further discussion

Comparisons with previous intra-oscillator approaches

To put this work in context, we compare our results with other approaches based on intra-cavity terahertz generation. Intra-cavity terahertz generation has already been demonstrated both inside passive enhancement cavities [25] and inside laser oscillators [26–28]. These two approaches follow the same principle that consists in recycling the unconverted pump pulse energy at each round trip for profiting from higher power. In practice, passive enhancement cavities are challenging to implement. They often need an active stabilization for phase synchronization, and require low cavity losses to reach high enhancement factors. In contrast, placing the terahertz emitter inside the cavity of a laser-oscillator is in general simpler since it does not require coherent coupling and the round-trip gain compensates the losses. In this section, we compare our result to [26–29], which all report on intra-oscillator terahertz generation. The performance of each source are summarized Table 3.1.

Table 3.1: Comparison of different approaches to intra-oscillator terahertz generation.^a

Ref.	Method	Driving laser	P_{av} (μW)	$\Delta\nu$ (THz)	η_{IR}	η_{pump}
[26]	transient photocurrent	Ti:sapphire (bulk)	7	3	$7.8 \cdot 10^{-7}$	$1.8 \cdot 10^{-6}$
[27]	transient photocurrent	Yb-doped (fiber)	4.2	<1	$3.1 \cdot 10^{-5}$	NR
[28]	OR in ZnTe	Ti:sapphire (bulk)	NR	2.5	NR	NR
This paper	OR in GaP	Yb:CALGO (bulk)	35	7	$1.8 \cdot 10^{-6}$	$5 \cdot 10^{-6}$
This paper	OR in GaP	Yb:CALGO (bulk)	150	5.5	$6.8 \cdot 10^{-6}$	$2.3 \cdot 10^{-5}$
[29]	OR in LN	Yb-doped (TDL)	500	3	$1.9 \cdot 10^{-6}$	$1.4 \cdot 10^{-6}$

^a OR: optical rectification; P_{av} : generated terahertz average power; $\Delta\nu$: generated terahertz spectral bandwidth; η_{IR} : conversion efficiency with respect to the near-infrared driving pulses; η_{pump} : conversion efficiency with respect to the power delivered by the laser pump.

To compare the results, we use two types of optical efficiency as metrics. First, the infrared-to-terahertz conversion efficiency, defined as the ratio between the generated terahertz power and intra-cavity driving power, characterizes the efficiency of the terahertz emitter. Then we use the pump-to-terahertz efficiency, which is the ratio between the terahertz power and the power used to pump the laser. This ratio characterizes the efficiency of the overall system.

The first demonstration of terahertz generation inside the cavity of a laser oscillator was reported in 2002 [26]. In this work, the terahertz radiation is generated inside a Ti:sapphire laser oscillator by a transient photocurrent at the surface of a semiconductor saturable absorber mirror, which also ensures self-starting and stable mode-locking. With 4 W of pump power, the laser operates at 0.9 W of intra-cavity average power, which results in 7 μW of terahertz radiation within a 3-THz broad spectrum. This corresponds to a pump-to-terahertz efficiency of only $1.8 \cdot 10^{-6}$, which may be due to the fact the Ti:sapphire laser was not optimized for high intra-cavity average power. A similar approach based on transient photocurrent was demonstrated inside the cavity of Yb-doped fiber laser oscillator [27]. Here, the authors achieve 4.2 μW of average power with a bandwidth smaller than 1 THz. The overall efficiency of the system is not reported in the paper. While those two works were the first to demonstrate terahertz generation directly intra-oscillator, the power levels were limited to only few microwatts. The first intra-oscillator terahertz generation based on optical rectification was reported in 2010 [28]. The authors drive the frequency conversion in zinc telluride crystals placed inside the cavity of a Ti:sapphire laser oscillator. The terahertz power was not reported and the spectrum extends only to 2.5 THz due to the 1-mm-thick zinc telluride crystal that drastically limits the phase-matching bandwidth of optical rectification. In summary, we achieve more than 20 times higher average power, broader spectral bandwidths as well as larger pump-to-terahertz efficiency compared to previous intra-oscillator based approaches. These improvements can be attributed to the design of the system. First, we employ an efficient and robust ultrafast laser oscillator that exploits the potential of Yb:CALGO for generating ultrashort pulses at high average power and high optical-to-optical efficiency. Second, driving optical rectification in GaP crystals enables larger spectral bandwidths compared to other commonly used crystals such as ZnTe or LN.

Comparison with our thin-disk result

In this paragraph, we compare our results to a conventional single-pass approach based on optical rectification in GaP [24]. Using a powerful thin-disk laser delivering 20 W of average power at 95 fs pulse duration and 48 MHz repetition rate, they drive a 0.3-mm-thick GaP crystal and achieve up to 110 μW of

3.1. Intra-oscillator broadband THz generation in a compact ultrafast diode-pumped solid-state laser

terahertz radiation with a >5 -THz bandwidth. The corresponding infrared-to-terahertz efficiency of $5.5 \cdot 10^{-6}$ is comparable to what we report in the paper, which is expected since the driving settings of the two experiments are similar. However, the overall efficiency with respect to the 126-W pump power drastically reduces to only $8.7 \cdot 10^{-7}$, which is twenty five times lower than what we achieved in our work.

Limitations and prospects

Further power scaling of our approach may be challenging. At high driving power levels, GaP crystals suffer from linear and nonlinear absorptions, which besides causing strong detrimental thermal lensing, induce an inverse saturable absorber effect that can lead to mode-locking instabilities [30, 31]. However, our technique has been recently scaled to higher power levels [29]. To circumvent the potential limitations arising from the GaP material, they use a lithium niobate crystal featuring less nonlinear absorptions and even higher damage threshold. The 50- μm -thick LN crystal is placed inside the cavity of a powerful thin-disk laser that operates with more than 250 W of intra-cavity average power. This way, they achieve up to 0.5 mW of terahertz average power and 3 THz of spectral bandwidth. This result may indicate that exploring other nonlinear materials may be the key for future power scaling.

Additionally, looking ahead, it would be interesting to repeat this study using the gigahertz laser source described in chapter 1. Besides further reducing the size of the overall system, high repetition rates are beneficial to improve the signal-to-noise ratio in terahertz time-resolved spectroscopy.

3.1.3 Acknowledgment

I would like to thank Jakub Drs for his support in implementing the terahertz diagnostic stage.

Intra-oscillator broadband THz generation in a compact ultrafast diode-pumped solid-state laser

MARIN HAMROUNI,^{*} JAKUB DRS, NORBERT MODSCHING,[✉]
VALENTIN J. WITTEW,[✉] FRANÇOIS LABAYE,[✉]
AND THOMAS SÜDMEYER[✉]

Laboratoire Temps-Fréquence (LTF), Institut de Physique, Université de Neuchâtel, Avenue de Bellevaux 51, 2000 Neuchâtel, Switzerland

^{*}marin.hamrouni@unine.ch

Abstract: We demonstrate broadband and powerful terahertz (THz) generation at megahertz repetition rate based on intra-oscillator optical rectification (OR) in gallium phosphide (GaP). By placing the nonlinear crystal directly inside the cavity of a Kerr-lens mode-locked ultrafast diode-pumped solid-state laser (DPSSL) oscillator, we demonstrate a compact and single-stage THz source. Using only 7 W of diode-pump power, we drive OR in a GaP crystal with 22 W of average power at ~80 MHz repetition rate. In a first configuration, using a 0.3-mm-thick GaP and 105 fs driving pulses, we generate up to 150 μ W of THz radiation with a spectrum extending to 5.5 THz. In a second configuration allowing for sub-50-fs pulse duration, we generate up to 7 THz inside a 0.1-mm-thick GaP crystal. This performance is well suited for THz time-domain spectroscopy and THz imaging. Intra-oscillator THz generation in sub-100-fs DPSSLs is a promising way to scale down footprint, complexity and cost of powerful broadband THz sources.

© 2021 Optical Society of America under the terms of the [OSA Open Access Publishing Agreement](#)

1. Introduction

During the last decades, broadband terahertz (THz) generation driven by ultrafast lasers has opened up access to numerous applications such as THz time-domain spectroscopy or spectral imaging [1]. However, the conversion efficiency between the driving laser and the THz radiation is typically relatively low, ranging between a few parts per million up to a few percent. Although several microwatts of THz average power are sufficient for some applications such as terahertz time-domain spectroscopy, many others such as THz imaging or spectroscopy of highly absorptive samples would strongly benefit from higher THz average powers [2]. In recent years, we have witnessed a considerable progress in the development of high-power THz systems. New THz sources based on plasmonic-enhanced photoconductive antennas [3,4] and organic nonlinear crystals [5,6] achieve milliwatt-class broadband THz generation from moderate pump power levels of only a few watts. Another highly promising direction for increased THz power is the use of well-established techniques such as optical rectification (OR) in nonlinear crystals or two-color laser filamentation at much higher pump power levels from novel ultrafast lasers. Up to 1.35 mW of THz average power with a spectrum reaching up to 6 THz have been generated by driving OR in gallium phosphide (GaP) with a 100-W nonlinearly compressed thin-disk laser (TDL) oscillator [7]. Later on, driving OR in lithium niobite instead of GaP, 66 mW of THz average power with a spectrum extending up to 2 THz were generated using the same driving laser [8]. Finally, 50 mW of THz average power with a spectrum expected to extend up to 30 THz was demonstrated using two-color laser filamentation in a neon gas target driven by a 160-W chirped-pulse fiber-amplifier system at 100 kHz repetition rate [9]. However, the complexity, the size and the cost of these systems due to, e.g., the required diode pump power or the vacuum

chamber might still be a limiting factor for many applications requiring small and compact sources.

Driving a nonlinear frequency conversion process inside a laser cavity has proven to be a successful approach for reducing the complexity of the system and increasing the overall efficiency [10–12]. Similarly, placing the THz generation crystal in a laser cavity allows for recycling of the unconverted pulse energy in each cavity roundtrip. This strongly increases the available driving power in comparison to the outcoupled beam. However, previous demonstrations of intra-cavity THz generation were so far strongly restricted in the demonstrated power levels. In [13], intra-oscillator THz generation reaching up to 7 μW of THz average power was achieved by a transient photocurrent at the surface of a semiconductor saturable absorber mirror, which also initiated and stabilized the pulses in a femtosecond Ti:sapphire oscillator. In 2008, this intra-oscillator technique was applied in a soliton fiber laser [14]. Here a THz yield of 4 μW and a conversion efficiency of 3.1×10^{-5} were achieved. In the same year, passive enhancement cavities were used for the generation of THz radiation using OR [15] and THz generation inside a dual frequency optical parametric oscillator via difference frequency generation in DAST was achieved [16]. The first optical rectification inside a femtosecond oscillator was demonstrated in 2010 using a Ti:sapphire laser oscillator [17]. However, the THz average power was not measured and the THz spectrum was restricted to 2.5 THz due to the 1-mm-thick zinc telluride crystal used for OR.

In the last decade, ultrafast technology strongly progressed [18–20]. Today, ultrafast solid-state laser oscillators can operate at several hundred watts of intra-oscillator average power with sub-100-fs pulses [21–25] which is required for powerful and broadband THz generation [7,26–28].

In our experiment, we drive OR in a GaP crystal which is placed inside the cavity of a Kerr-lens mode-locked (KLM) Yb:CALGO bulk laser oscillator. Yb:CALGO is an outstanding gain material for ultrafast lasers thanks to its broadband gain emission spectrum combined with a low quantum defect and relatively high thermal conductivity [29–31], making it particularly attractive for compact and efficient ultrafast DPSSLs [32]. For example, 30-fs pulses at optical-to-optical efficiencies of $\sim 30\%$ were recently achieved [33]. Moreover, it can be pumped by low cost 980 nm multimode pump diodes. In our intra-oscillator THz system, OR was driven in a GaP crystal at 22 W of intra-cavity laser power, 105 fs pulse duration, and 75 MHz repetition rate. We achieve up to 150 μW of THz average power with a spectrum extending to 5.5 THz using only 7 W of diode pump power. Compared to a single-pass system with similar performance [27], the intra-cavity approach requires 20 times less pump power. We also demonstrate that the THz spectrum can be extended up to ~ 7 THz at the expense of THz average power using a thinner GaP crystal combined with shorter pulse duration. These results show that intra-oscillator THz generation via OR is a promising way to simplify and reduce the size of the current state-of-the-art THz sources. GaP can support more than hundred watts of driving power [34], and we expect that milliwatt THz power levels are within reach of this technology.

2. Experimental setup

The experimental setup is shown in Fig. 1. The laser oscillator is based on a 3-mm-long, antireflection-coated (AR) Yb(3 at.%):CALGO crystal. The crystal is mounted in a water-cooled copper holder and optically pumped at 980 nm by a commercially available 10-W multimode fiber coupled laser diode module. The positive group delay dispersion (GDD) introduced by the gain medium, the GaP crystal, and the self-phase modulation is compensated by several dispersive mirrors (DM). A 2.7-mm diameter hard aperture enables stable KLM operation. An output coupler (OC) with a transmission of 1.5% is placed as a folding mirror, thus providing two out-coupled beams. One beam is used to characterize the driving laser while the other beam is used for electro-optic sampling (EOS). The GaP crystal is placed close to the end mirror of

the laser cavity without any active cooling. Both faces of the GaP crystal have an AR coating which was designed and grown in our own ion beam sputtering coating facility. The THz radiation is generated in two directions inside the GaP crystal, however, only one direction is characterized. The strongly diverging THz beam is directed by two off-axis parabolic mirrors (OAPM) onto a second 0.15-mm-thick GaP crystal for EOS. The THz beam is mechanically chopped at around 75 Hz for subsequent lock-in detection. The THz average power is measured by placing a pyroelectric power meter at the position of the GaP crystal used for the detection. Three layers of black plastic foil were inserted between the two OAPMs in order to prevent any of the parasitic scattered infrared light from reaching the detector. Their individual THz transmission of 46% has been determined in a previous study [27] and the here stated measured THz average powers were corrected by this transmission factor. The system was purged by dry air to decrease the relative humidity to below 20% in order to reduce the water vapour absorption of the THz radiation.

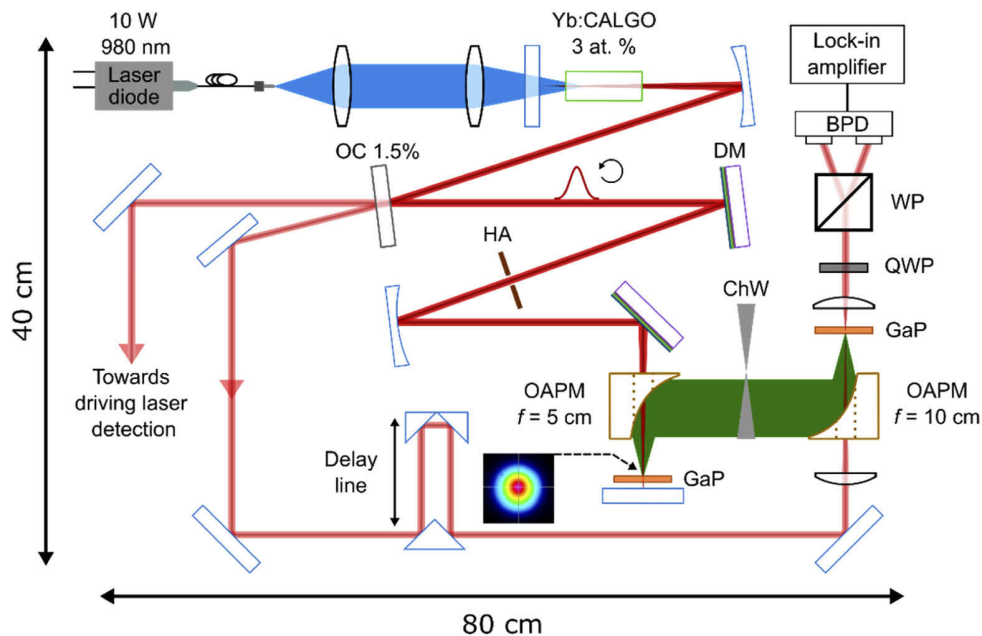


Fig. 1. Experimental setup for intra-oscillator THz generation and detection by electro-optic sampling. OC, 1.5% transmission output coupler; DM, dichroic mirror; HA, hard aperture; OAPM, off-axis parabolic mirror; ChW, chopper wheel; QWP, quarter waveplate; WP, Wollaston prism; BPD, balanced photodetector. The footprint of the overall system is 80 cm \times 40 cm.

3. Experimental results

We characterized the system in two different configurations optimized for either high THz average power or for a broader THz spectrum. Table 1 summarizes the characteristics of the driving laser and the resulting THz performance. The first configuration optimized for high THz average power uses a 0.3-mm-thick GaP crystal. OR in GaP was driven at 22 W of intra-cavity average power with 105 fs pulse duration corresponding to 12.2 nm of full width at half maximum (FWHM) spectral bandwidth [Figs. 2(a) and 2(b)] and 75 MHz repetition rate.

The pulse duration was adapted to the phase matched window of the 0.3-mm GaP crystal according to [27]. The beam diameter inside the crystal was \sim 400 μ m, corresponding to a

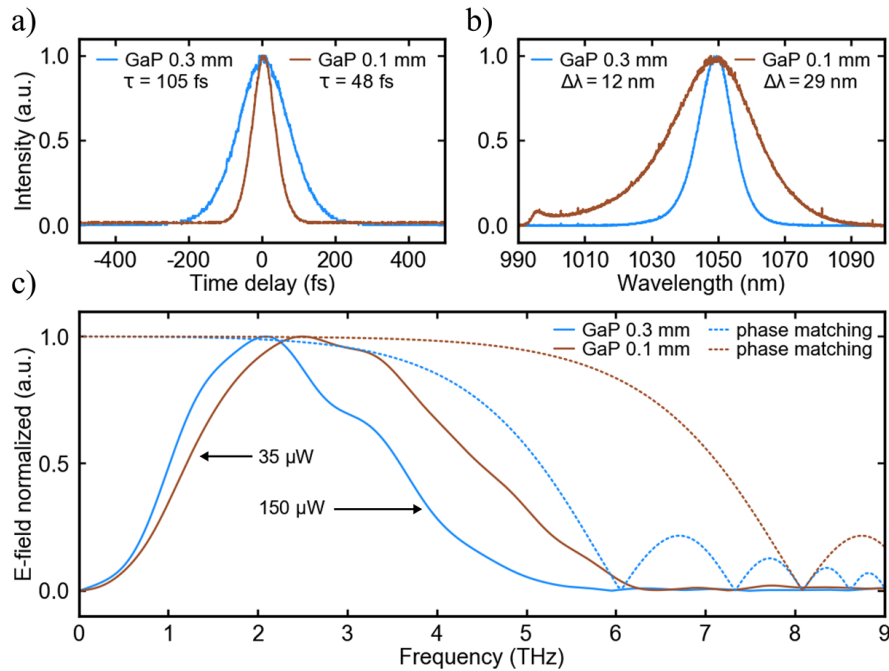


Fig. 2. a) Autocorrelation trace and b) optical spectrum of the driving pulse for the configuration 1 (using a 0.3-mm-thick GaP) and the configuration 2 (using a 0.1-mm-thick GaP). c) Normalized THz E-field in the frequency domain detected by electro-optic sampling (plain line) and the corresponding theoretical phase matching curves (dashed lines) for both configurations. τ , FWHM pulse duration; $\Delta\lambda$, FWHM spectral bandwidth.

Table 1. Driving laser parameters and resulting THz performance corresponding to the configuration 1 using a 0.3-mm-thick GaP crystal and the configuration 2 using a 0.1-mm-thick crystal.^a

GaP thickness	Driving laser					THz results			
	P_{pump} (W)	$P_{\text{av.intra}}$ (W)	f_{rep} (MHz)	τ (fs)	$\Delta\lambda$ (nm)	2ω ($1/e^2$) (μm)	I_p (GW/cm^2)	$P_{\text{av,THz}}$ (μW)	$\nu_{\text{THz,max}}$ (THz)
0.3 mm	6.5	22	75	105	12.2	400	4	150	5.5
0.1 mm	7	20	80	48	29.4	350	9	35	7

^a P_{pump} , pump power of the laser; $P_{\text{av.intra}}$, intra-cavity average power; f_{rep} , repetition rate; τ , FWHM pulse duration; $\Delta\lambda$, FWHM spectral bandwidth; $2(1/e^2)$, beam diameter in the GaP; I_p , peak intensity in the GaP; $P_{\text{av,THz}}$, THz average power; $\nu_{\text{THz,max}}$, maximal THz spectrum frequency.

peak intensity of $\sim 4 \text{ GW}/\text{cm}^2$, significantly below the damage threshold of $60 \text{ GW}/\text{cm}^2$ [35]. Figure 2(c) shows the generated THz spectrum (blue line) retrieved from the EOS measurement in the frequency domain. The THz spectrum is centred at 2 THz and extends up to 5.5 THz, slightly below the limit imposed by the phase matching condition. We measured up to $150 \mu\text{W}$ of THz average power leading to an optical-to-optical efficiency of 7×10^{-6} and 2×10^{-5} with respect to the driving laser and the multimode pump diode average power, respectively.

The second configuration aims to further exploit the potential of the ultrafast driving source for broadband THz generation. It utilizes a 0.1-mm GaP crystal allowing for a phase-matched window extending up to ~ 8 THz. However, the broader phase-matched window of the thinner

GaP crystal comes at the expense of a reduced THz average power due to the shorter interaction length. The pulse duration was adjusted to 48 fs corresponding to 12.2 nm of FWHM spectral bandwidth by reducing the negative GDD introduced by the DMs. The laser beam diameter inside the GaP crystal was decreased to $\sim 350 \mu\text{m}$ by slightly adjusting the cavity length. The decrease of the pulse duration and beam diameter led to a higher peak intensity inside the GaP crystal estimated to be $\sim 9 \text{ GW/cm}^2$ in this configuration. Driving OR at 20 W of intra-cavity average power and 80 MHz repetition rate resulted in the generation of 35 μW of THz average power with a spectrum centred at 3 THz and extending up to ~ 7 THz. The drop of the average THz power is consistent with the change in the crystal thickness and the driving laser peak intensity. The measured spectrum does not reach the 8-THz phase-matching limit mostly due to the thicker GaP crystal of 0.15 mm used for EOS, restricting the measurement range to approximately 7 THz.

In the current setup we were limited to intra-cavity average powers of ~ 20 W by the onset of a continuous-wave lasing breakthrough at higher pumping powers. We attribute this effect to the thermal lens and multiphoton absorption inside the GaP crystal disrupting the KLM operation. We expect that optimization of the cavity layout to accommodate the thermal lens combined with higher repetition rate will allow for significant increase of the intra-cavity driving power. Further advances are expected by implementing efficient cooling of the GaP crystal.

4. Conclusion

In this proof-of-principle experiment, we have demonstrated efficient and broadband THz generation based on OR in GaP in a simple collinear geometry directly inside the cavity of an ultrafast laser oscillator. In a first configuration, the system generated up to 150 μW of THz average power with an optical spectrum extending up to 5.5 THz and 35 μW with a spectrum extending up to 7 THz in a second configuration. This simple concept of intra-oscillator THz generation allows for high average driving powers in combination with short pulse duration which are otherwise available only from more complex laser systems requiring diode pump powers exceeding the 100 W range. For instance, in comparison to a single-pass THz-source based on OR in GaP driven by a high-power TDL oscillator utilizing the same GaP thickness, our intra-oscillator approach requires 20 times lower pump power at a fraction of the component cost [27]. We also expect a further improvement of the technology is easily within reach. Since up to 1.35 mW of THz average power has already been generated by single-pass OR in GaP [7], we believe that the intra-oscillator approach will soon reach a comparable performance.

Funding. Schweizerischer Nationalfonds zur Förderung der Wissenschaftlichen Forschung (200021_188456, SPARK CRSK-2_190593).

Disclosures. The authors declare that there are no conflicts of interest related to this article.

Data availability. Data underlying the results presented in this paper are available in Ref. [36].

References

1. P. U. Jepsen, D. G. Cooke, and M. Koch, "Terahertz spectroscopy and imaging – Modern techniques and applications," *Laser & Photon. Rev.* **5**(1), 124–166 (2011).
2. M. Tonouchi, "Cutting-edge terahertz technology," *Nat. Photonics* **1**(2), 97–105 (2007).
3. N. T. Yardimci, S.-H. Yang, C. W. Berry, and M. Jarrahi, "High-power terahertz generation using large-area plasmonic photoconductive emitters," *IEEE Trans. Terahertz Sci. Technol.* **5**(2), 223–229 (2015).
4. N. T. Yardimci, S. Cakmakyan, S. Hemmati, and M. Jarrahi, "A High-Power Broadband Terahertz Source Enabled by Three-Dimensional Light Confinement in a Plasmonic Nanocavity," *Sci. Rep.* **7**(1), 1–8 (2017).
5. T. O. Buchmann, E. J. Railton Kelleher, M. Jazbinsek, B. Zhou, J.-H. Seok, O.-P. Kwon, F. Rotermund, and P. U. Jepsen, "High-power few-cycle THz generation at MHz repetition rates in an organic crystal," *APL Photonics* **5**(10), 106103 (2020).
6. C. Vicario, M. Jazbinsek, A. V. Ovchinnikov, O. V. Chefonov, S. I. Ashitkov, M. B. Agranat, and C. P. Hauri, "High efficiency THz generation in DSTMS, DAST and OHI pumped by Cr:forsterite laser," *Opt. Express* **23**(4), 4573–4580 (2015).

7. F. Meyer, N. Hekmat, T. Vogel, A. Omar, S. Mansourzadeh, F. Fobbe, M. Hoffmann, Y. Wang, and C. J. Saraceno, "Milliwatt-class broadband THz source driven by a 112 W, sub-100 fs thin-disk laser," *Opt. Express* **27**(21), 30340–30349 (2019).
8. F. Meyer, T. Vogel, S. Ahmed, and C. J. Saraceno, "Single-cycle, MHz repetition rate THz source with 66 mW of average power," *Opt. Lett.* **45**(9), 2494–2497 (2020).
9. J. Buldt, M. Mueller, H. Stark, C. Jauregui, and J. Limpert, "Fiber laser-driven gas plasma-based generation of THz radiation with 50-mW average power," *Appl. Phys. B* **126**(2), 1–5 (2020).
10. R. G. Smith, K. Nassau, and M. F. Galvin, "Efficient continuous optical second harmonic generation," *Appl. Phys. Lett.* **7**(256), 129 (1965).
11. Q. H. Xue, Q. Zheng, Y. K. Bu, F. Q. Jia, and L. S. Qian, "High-power efficient diode-pumped Nd:YVO₄/LiB₃O₅ 457 nm blue laser with 46 W of output power," *Opt. Lett.* **31**(8), 1070 (2006).
12. L. McDonagh and R. Wallenstein, "Low-noise 62 W CW intracavity-doubled TEM₀₀ Nd:YVO₄ green laser pumped at 888 nm," *Opt. Lett.* **32**(7), 802–804 (2007).
13. J. Darmo, T. Müller, G. Strasser, K. Unterrainer, T. Le, A. Stingl, and G. Tempea, "Voltage-controlled intracavity terahertz generator for self-starting Ti:sapphire lasers," *Opt. Lett.* **27**(21), 1941 (2002).
14. G. Matthäus, B. Ortaç, J. Limpert, S. Nolte, R. Hohmuth, M. Voitsch, W. Richter, B. Pradarutti, and A. Tünnermann, "Intracavity terahertz generation inside a high-energy ultrafast soliton fiber laser," *Appl. Phys. Lett.* **93**(26), 261105 (2008).
15. M. Theuer, D. Molter, K. Maki, C. Otani, J. A. L'huillier, and R. Beigang, "Terahertz generation in an actively controlled femtosecond enhancement cavity," *Appl. Phys. Lett.* **93**(4), 041119 (2008).
16. T. Shibuya, T. Akiba, K. Suizu, H. Uchida, C. Otani, and K. Kawase, "Terahertz-Wave Generation Using a 4-Dimethylamino-*N*-methyl-4-stilbazolium tosylate Crystal Under Intra-Cavity Conditions," *Appl. Phys. Express* **1**, 042002 (2008).
17. S. Xu, J. Liu, G. Zheng, and J. Li, "Broadband terahertz generation through intracavity nonlinear optical rectification," *Opt. Express* **18**(22), 22625–22630 (2010).
18. U. Keller, "Ultrafast solid-state laser oscillators: a success story for the last 20 years with no end in sight," *Appl. Phys. B* **100**(1), 15–28 (2010).
19. H. Fattahi, H. G. Barros, M. Gorjan, T. Nubbemeyer, B. Alsaif, C. Y. Teisset, M. Schultze, S. Prinz, M. Haefner, M. Ueffing, A. Alismail, L. Vámos, A. Schwarz, O. Pronin, J. Brons, X. T. Geng, G. Arisholm, M. Ciappina, V. S. Yakovlev, D.-E. Kim, A. M. Azzeer, N. Karpowicz, D. Sutter, Z. Major, T. Metzger, and F. Krausz, "Third-generation femtosecond technology," *Optica* **1**(1), 45 (2014).
20. D. T. Reid, C. M. Heyl, R. R. Thomson, R. Trebino, G. Steinmeyer, H. H. Fielding, R. Holzwarth, Z. Zhang, P. Del'Haye, T. Südmeyer, G. Mourou, T. Tajima, D. Faccio, F. J. M. Harren, and G. Cerullo, "Roadmap on ultrafast optics," *J. Opt.* **18**(9), 093006 (2016).
21. A. Greborio, A. Guandalini, and J. Aus der Au, "Sub-100 fs pulses with 12.5-W from Yb:CALGO based oscillators," in *Proc. SPIE*, (2012), paper 823511.
22. A. Diebold, F. Emaury, C. Schriber, M. Golling, C. J. Saraceno, T. Südmeyer, and U. Keller, "SESAM mode-locked Yb:CaGdAlO₄ thin disk laser with 62 fs pulse generation," *Opt. Lett.* **38**(19), 3842–3845 (2013).
23. A. Klenner, M. Golling, and U. Keller, "High peak power gigahertz Yb:CALGO laser," *Opt. Express* **22**(10), 11884–11891 (2014).
24. S. Hakobyan, V. J. Wittwer, K. Gürel, A. S. Mayer, S. Schilt, and T. Südmeyer, "Carrier-envelope offset stabilization of a GHz repetition rate femtosecond laser using opto-optical modulation of a SESAM," *Opt. Lett.* **42**(22), 4651–4654 (2017).
25. J. Fischer, J. Drs, F. Labaye, N. Modsching, V. Wittwer, and T. Südmeyer, "Intra-oscillator high harmonic generation in a thin-disk laser operating in the 100-fs regime," *Opt. Express* **29**(4), 5833–5839 (2021).
26. C. Paradis, J. Drs, N. Modsching, O. Razskazovskaya, F. Meyer, C. Kränkel, C. J. Saraceno, V. J. Wittwer, and T. Südmeyer, "Broadband terahertz pulse generation driven by an ultrafast thin-disk laser oscillator," *Opt. Express* **26**(20), 26377–26384 (2018).
27. J. Drs, N. Modsching, C. Paradis, C. Kränkel, V. J. Wittwer, O. Razskazovskaya, and T. Südmeyer, "Optical rectification of ultrafast Yb lasers: pushing power and bandwidth of terahertz generation in GaP," *JOSA B* **36**(11), 3039–3045 (2019).
28. G. Barbiero, H. Wang, J. Brons, B.-H. Chen, V. Pervak, and H. Fattahi, "Broadband terahertz solid-state emitter driven by Yb:YAG thin-disk oscillator," *J. Phys. B: At. Mol. Opt. Phys.* **53**(12), 125601 (2020).
29. J. Petit, P. Goldner, and B. Viana, "Laser emission with low quantum defect in Yb:CaGdAlO₄," *Opt. Lett.* **30**(11), 1345–1347 (2005).
30. Y. Zaouter, J. Didierjean, F. Balembois, G. L. Leclin, F. Druon, P. Georges, J. Petit, P. Goldner, and B. Viana, "47-fs diode-pumped Yb³⁺:CaGdAlO₄ laser," *Opt. Lett.* **31**(1), 119–121 (2006).
31. F. Druon, F. Balembois, and P. Georges, "New Materials for Short-Pulse Amplifiers," *IEEE Photon. J.* **3**(2), 268–273 (2011).
32. P. Sévillano, P. Georges, F. Druon, D. Descamps, and E. Cormier, "32-fs Kerr-lens mode-locked Yb:CaGdAlO₄ oscillator optically pumped by a bright fiber laser," *Opt. Lett.* **39**(20), 6001–6004 (2014).

33. F. Labaye, V. J. Wittwer, N. Modsching, O. Razskazovskaya, E. Cormier, and T. Südmeyer, "Yb:CALGO bulk oscillator generating ultrashort pulses at high efficiency by cross-polarized optical pumping," in *9th EPS-QEOD Europhoton conference*, (2020), paper We-A1.4.
34. N. Hekmat, T. Vogel, Y. Wang, S. Mansourzadeh, F. Aslani, A. Omar, M. Hoffmann, F. Meyer, and C. J. Saraceno, "Cryogenically cooled GaP for optical rectification at high excitation average powers," *Opt. Mater. Express* **10**(11), 2768–2782 (2020).
35. Y. Li, F. Liu, Y. Li, L. Chai, Q. Xing, M. Hu, and C. Wang, "Experimental study on GaP surface damage threshold induced by a high repetition rate femtosecond laser," *Appl. Opt.* **50**(13), 1958–1962 (2011).
36. M. Hamrouni, J. Drs, N. Modsching, V. J. Wittwer, F. Labaye, and T. Südmeyer, *EUDAT B2SHARE repository: b2share*, (2021), <http://doi.org/10.23728/b2share.089c82b5f3594c558af796e13285beaa>

3.2 Efficient parametric downconversion by gain-trapped solitons

As discussed in the introduction, one of the latest breakthroughs in nonlinear optics has been the development of nanophotonic waveguide structures that confine the light inside subwavelength mode volumes. Besides featuring large nonlinear couplings, this new class of integrated devices offers additional degrees of freedom to engineer the optical properties via, for example, dispersion engineering. Among the most common nanophotonic materials, TFLN emerged as a standard platform for broadband frequency conversion at low power requirements [32, 33].

In practice, these devices use a thin film of LN bonded onto a lower-index cladding layer chosen for strong optical confinement. Depending on the index contrast between the LN and the substrate, a fraction more or less important of the guided mode propagates through the cladding. Hence, the optical properties of the cladding have significant impacts on the nonlinear performances. Besides influencing the dispersion properties of the nanowaveguide, the substrate contributes to the overall absorption losses experienced by the guided modes. So far, most TFLN devices have been using silica as bottom cladding, which suffers from high absorptions above $\sim 2.5 \mu\text{m}$, ultimately degrading the device performance for frequency conversion in the mid-infrared. Recently, TFLN-on-sapphire emerged as a promising alternative platform, which besides ensuring strong light confinement, features lower absorption coefficients across the entire LN transparency window. Since this platform is relatively new, only few studies have been using TFLN-on-sapphire for MIR frequency conversion [34–36]. In the following article, we harness the promising advantages of TFLN-on-sapphire to drive optical parametric amplification (OPA) and generate broadband and coherent light in the mid-infrared.

3.2.1 Article outline

Context

In the context of spectroscopy, optical parametric amplification is often used as a source of broadband and coherent light at wavelengths that are difficult, or even impossible, to produce with laser gain media. In the pulsed regime, when seeded by a coherent signal, OPA can transfer the comb structure of the driving pulses to the idler, thus realizing a broadband OFC at the desired wavelengths. For nearly all applications, both broadband and efficient frequency conversion are desirable. When driven with femtosecond pulses, the natural dispersion of

the nonlinear media tends to restrict the interaction length between the pump, signal and idler pulses to only a few millimeters [37]. As a consequence, the short interaction length not only limits the conversion efficiency, but also reduces the bandwidth of the nonlinear process. To overcome this limitation, OPA can be operated in regimes where the nonlinear interactions are no longer limited by the dispersion. For instance, when the group velocities of the interacting pulses are such that the signal and idler walk-off from the pump in opposite directions, referred as symmetric walk-off, an interplay between the high nonlinear gain and the temporal offset can trap the three pulses together. More specifically, the large parametric gain located around the peak of the pump amplifies the overlapping tails of the signal and idler, which effectively pulls the centroid of each pulse towards the peak of the pump, and counteracts the temporal walk-off [37]. Provided enough nonlinear gain, this mechanism can completely balance the GVM and trap the pulses together, thus forming a three-wave soliton. In this case, the pulses interact over distances well in excess of the natural pulse walk-off length, enabling efficient conversions and large bandwidths at low input power. This approach of OPA, referred to as gain-guiding OPA, has been already demonstrated inside bulk nonlinear media, which typically require laser systems capable of delivering at least several nanojoules of pulse energy [37–41], imposing stringent requirements on the driving source, especially at high repetition rates.

In principle, these limitations can be overcome by using TFLN nanowaveguides, drastically reducing the power required to achieve the pulse trapping regime to picojoules, rather than nanojoules. Second, in contrast to bulk nonlinear media where the symmetric walk-off regime is restricted to spectral ranges imposed by the natural dispersion of the material, nanodevices offer the possibility to tailor the GVMs via dispersion engineering techniques, allowing operation at any wavelength within the transparency window. In this work, we realize the first demonstration of gain-trapped parametric down-conversion in integrated devices. In the first section, we discuss the theory of gain-trapped OPA in waveguides. We derive a simple model capturing the essential OPA dynamics, which we subsequently verify. In the next section, we perform the experimental study.

Results

In the theoretical part, we write the coupled-wave equations (CWEs) for undepleted pump OPA in the frequency domain and show the differential equation system reduces to an eigenvalue problem that can be numerically solved by standard computers in seconds. This simple formalism captures the main features of the down-conversion dynamics and shows the ultimate advantages of gain-trapping OPA. In a nutshell, gain-guiding OPA features lower power

requirement, enables higher conversion efficiency and broader bandwidths, in addition to being robust to seeding conditions. In practice, the latter point is a major advantage since it enables generation of a broadband idler using a pulsed pump laser and a continuous-wave seed, evading the need for both a pump and seed pulsed source. The behaviour of gain-trapped OPA is discussed in more detail in the manuscript 3.2.4.

In the second part, we discuss about the design and characterization of the fabricated TFLN on sapphire waveguides. We use geometric dispersion engineering to achieve symmetric walk-off between pump, signal and idler pulses centered around 1045, 1550 and 3200 nm, respectively. The waveguides are pumped by a commercially available Yb-doped fiber laser, and seeded by a low-power continuous-wave laser at telecom wavelengths. After verifying the fabricated waveguides operate in the regime of gain-trapped OPA, we characterize the performance of the nonlinear process. When seeded with microwatts of average power, OPA saturation occurs with as little as 5.5 pJ of on-chip pump pulse energy, which gives a gain coefficient as large as 140 dB/cm. Before saturation, the down-converted signal and idler spectra have 3-dB bandwidths of 5 THz, which support transform-limited pulse durations as short as 70 fs. In the saturated regime, using in-coupled pulse energies smaller than 10 pJ, we observe photon conversion efficiencies as large as 50%. With a maximum on-chip pump pulse energy of 11 pJ, we record up to 155 μ W and 320 μ W of idler and signal average power, respectively, and measure a broad idler spectrum extending across 600 nm at the -20 dB level.

In the last section, we investigate the robustness of the gain-trapping regime with respect to changes in the phase-matched wavelengths. We use three waveguides with different poling periods that produce signal wavelength of 1495 nm, 1555 nm and 1585 nm, respectively. Since the pump wavelength is the same in the three configurations, the idler wavelength shifts accordingly to 3500, 3200 and 3100 nm, respectively. The formation of gain-trapped signal and idler pulses is confirmed in the three configurations. Furthermore, all the configurations achieve both broad bandwidths and high conversion efficiencies, despite the significant GVM differences due to the presence of group velocity dispersion. In summary, in this section we show gain-trapped OPA is robust against phase-matched wavelength tunings and dispersion variations.

Conclusion

Operating gain-trapped OPA in nanophotonic waveguides is highly promising for coherent generation of mid-infrared light at low power and energy requirements. Also, in addition to high conversion efficiencies and broad spectral bandwidths, this regime of OPA is robust against realistic fabrication errors

that could affect the optimal dispersion conditions. This approach to dispersion engineering is general and can be extended to any wavelength within the transparency window of the nonlinear medium. In principle, it can also be implemented in other nanophotonic platforms that offer enough degree of freedom for dispersion-engineering. For instance, extending this technique to material such as thin-film InGaP and AlGaAs is promising for realizing compact sources operating at longer mid-infrared wavelengths.

3.2.2 Further discussion: eigenmode decomposition

Gain-trapped parametric down-conversion has been theoretically described in in [42, 43]. In [43], they theoretically study the effect of gain-trapped OPA for three pulses undergoing temporal walk-off. By neglecting the pump depletion and temporal stretching of the three pulses (besides other common approximations), they show the temporal-domain CWEs for OPA reduce to an eigenvalue problem. Using this model, they derive closed-form solutions for the trapped signal and idler pulses assuming a sech-like pump.

In contrast to [36], in our article we derive the numerical model in the frequency domain. This choice is motivated by the fact that the solutions to the frequency-domain CWEs can be obtained for arbitrary dispersion relation. This approach transforms the time-domain CWEs, characterized by a set of three partial-differential equations, into a large system of differential equations that describes the interplay of the Fourier components of each wave. This section provides further details about the derivation of this model. More specifically, we describe the calculation steps from the time-domain CWEs to the eigenvalue problem (Eqn. 3 in the article).

We start with the time-domain CWEs for the signal and idler. Assuming an undepleted pump,

$$\partial_z A_s(z, t) = -i\kappa_s A_p(t) A_i^*(z, t) \exp(-i\Delta k_0 z) - (i\hat{D}_s(\partial_t) + \Delta k'_s \partial_t) A_s(z, t), \quad (3.1a)$$

$$\partial_z A_i(z, t) = -i\kappa_i A_p(t) A_s^*(z, t) \exp(-i\Delta k_0 z) - (i\hat{D}_i(\partial_t) + \Delta k'_i \partial_t) A_i(z, t), \quad (3.1b)$$

where A_s , A_i and A_p are the complex field amplitudes of the signal, idler, and pump, respectively, normalized such that $|A(z, t)|^2$ has units of Watts and corresponds to the instantaneous power contained in the corresponding wave. $\Delta k_0 = k_p(\omega_p) - k_s(\omega_s) - k_i(\omega_i) - 2\pi/\Lambda_g$ is the phase-mismatch for three-wave mixing evaluated at the carrier frequencies of the pump (ω_p), signal (ω_s), and idler (ω_i), respectively. Λ_g is the grating period used for quasi-phases matching. We note here that the subscripts associated with the propagation constants

are meant to convey that each wave can have different dispersion relations. $\Delta k'_\mu = k'_\mu - k'_p$ is the group velocity mismatch with respect to the pump. The dispersion operator $\hat{D}_\mu(\partial_t) = \sum_{j \geq 2} ((-i)^j k_\mu^{(j)} / j!) \partial_t^j$ contains contributions from second and higher dispersion orders. Here, $k_\mu^{(j)}$ represents the j^{th} derivative of the propagation constant k_μ at the central frequency ω_μ of the corresponding wave. The nonlinear coupling κ_μ is given in the article.

In absence of pump depletion, considering the periodic structure of the pump pulses, each envelope can be expanded into Fourier series,

$$A_\mu(z, t) = \sum_m A_{\mu,m}(z) \exp(2\pi i m t / T) \quad (3.2a)$$

$$A_{\mu,m}(z) = \frac{1}{T} \int_0^T A_\mu(z, t) \exp(-2\pi i m t / T) dt \quad (3.2b)$$

where μ denotes the subscripts p , s or i , $T = f_{\text{rep}}^{-1}$ is the repetition period of the pump laser and $A_{\mu,m}$ corresponds to m^{th} the Fourier components of the relevant wave.

We now replace the envelopes in Eqns. 3.1 by their series expansion, multiply each side of the resulting equation by $\exp(-2\pi i m t / T)$ and integrate to eliminate the product of exponential terms that have different frequencies. This gives the dynamical equation of the m^{th} Fourier component of the signal or idler, coupled with the components of the other wave through the pump modes. For the signal we find,

$$\partial_z A_{s,m}(z) = -i\kappa_s \sum_l A_{p,m+l} A_{i,l}^* \exp(-i\Delta k_0 z) - (i\hat{D}_s(\Omega_m) + i\Omega_m \Delta k'_s) A_{s,m}(z) \quad (3.3)$$

where $D_s(\Omega_m) = \sum_{j \geq 2} (\Omega_m^j k_s^{(j)} / j!)$ and $\Omega_m = 2\pi m / T$. The equations for the idler Fourier components are obtained interchanging the subscripts s and i . Eqn. 3.3 becomes translation invariant when transforming the signal and idler Fourier components according to $\tilde{A}_{\mu,m} = A_{\mu,m} \exp(i\Delta k_0 z / 2)$,

$$\partial_z \tilde{A}_{s,m}(z) = -i\kappa_s \sum_l A_{p,m+l} \tilde{A}_{i,l}^* - i(\hat{D}_s(\Omega_m) + \Omega_m \Delta k'_s - \frac{1}{2} \Delta k_0) \tilde{A}_{s,m}(z) \quad (3.4a)$$

$$\partial_z \tilde{A}_{i,m}^*(z) = i\kappa_i \sum_l A_{p,m+l} \tilde{A}_{s,l} + i(\hat{D}_i(\Omega_m) + \Omega_m \Delta k'_i - \frac{1}{2} \Delta k_0) \tilde{A}_{i,m}^*(z). \quad (3.4b)$$

Written this way, the dynamical equations can be recast into a single large

matrix that couples all the Fourier components of each wave:

$$\partial_z \begin{pmatrix} \vdots \\ \tilde{A}_{s,m}(z) \\ \vdots \\ \tilde{A}_{i,n}^*(z) \\ \vdots \end{pmatrix} = \begin{pmatrix} \ddots & & & & \\ & -i\Delta k_{s,m} & & & \\ & & \ddots & & \\ & & & \gamma_{s,mn} & \\ & & & & \ddots \\ & & & & & -\gamma_{i,nm} & & \\ & & & & & & i\Delta k_{i,n} & \\ & & & & & & & \ddots \end{pmatrix} \begin{pmatrix} \vdots \\ \tilde{A}_{s,m}(z) \\ \vdots \\ \tilde{A}_{i,n}^*(z) \\ \vdots \end{pmatrix}. \quad (3.5)$$

The diagonal blocks of the system matrix comprise the phase-mismatch of the Fourier components with respect to the central frequency, $\Delta k_{\mu,m} = -\frac{1}{2}\Delta k_0 + \Delta k'_\mu \Omega_m + \hat{D}_\mu(\Omega_m)$. The anti-diagonal blocks couple the signal and idler Fourier components via the modes of the pump rescaled by the waveguide nonlinearity, $\gamma_{\mu,mn} = -i\kappa_\mu A_{p,m+n}$. We note here that this equation corresponds to Eqn. 3 in the article. The only difference is the envelope normalization. Here, $|\tilde{A}_m|^2$ corresponds to the power in Watt while in the article $|\tilde{a}_m|^2$ is the photon flux contained inside the Fourier mode m .

We close this supplemental section by a comment about the Fourier decomposition. The model derived here assumes the periodicity of the pump (which is the case in practice). However, it is important to note that the discretization of the spectra through the periodicity of the pump is a mathematical convenience, rather than necessary to capture the physics. In that sense, the results do not depend on the repetition rate of the pump pulses, only on their duration and energy. Since numerical simulations require the discretization of the spectra, in essence the formalism and behaviour remains the same if we consider a single pump pulse rather than a train of pulses.

3.2.3 Acknowledgment

I have conducted the experiments in the laboratories of Martin Fejer and Amir Safavi-Naeini, in close collaboration with Alex Hwang for the design and fabrication of the waveguides and I would like to thank Marc Jankowski for his overall indispensable contribution.



Efficient parametric down-conversion by gain-trapped solitons

MARIN HAMROUNI,^{1,2,†}  MARC JANKOWSKI,^{1,3,†,*}  ALEXANDER Y. HWANG,¹ 
NAYARA JORNOD,¹  JATADHARI MISHRA,¹  HUBERT S. STOKOWSKI,¹ 
TIMOTHY P. MCKENNA,¹  CARSTEN LANGROCK,¹  THOMAS SÜDMEYER,² 
AMIR SAFAVI-NAEINI,¹  AND MARTIN M. FEJER¹

¹E. L. Ginzton Laboratory, Stanford University, Stanford, California 94305, USA

²Laboratoire Temps-Fréquence, Université de Neuchâtel, Avenue de Bellevaux 51, Neuchâtel, Switzerland

³NTT Research Inc., Physics & Informatics Laboratories, 940 Stewart Drive, Sunnyvale, California 94085, USA

[†]These authors contributed equally to this work.

*marc.jankowski@ntt-research.com

Received 3 November 2023; revised 3 January 2024; accepted 7 January 2024; published 22 February 2024

Optical parametric amplification is one of the most flexible approaches for generating coherent light at long wavelengths, but typical implementations require prohibitively large pump pulse energies to realize useful amounts of gain. In this work, we experimentally demonstrate an approach to optical parametric amplification in which an interplay between parametric gain and symmetric temporal walk-off confines the non-degenerate signal and idler to form a three-wave soliton. Gain-trapped solitons propagate stably over arbitrarily long interaction lengths, which reduces the energy required for high-gain operation by orders of magnitude. The devices demonstrated here realize large parametric gains (>70 dB) with only picojoules of pump pulse energy in a 5-mm-long thin-film lithium niobate on sapphire nanowaveguide. In addition, we observe an array of desirable features including high conversion efficiencies (>50%), wide tuning ranges (>100 nm), and broad spectral bandwidths (>180 nm 3 dB for the 3200-nm idler). When combined with the dispersion engineering available in tightly confining nanowaveguides, this approach enables high-gain optical parametric amplifiers operating at any wavelength. © 2024 Optica Publishing Group under the terms of the [Optica Open Access Publishing Agreement](#)

<https://doi.org/10.1364/OPTICA.510591>

1. INTRODUCTION

Optical parametric amplification (OPA) in second-order ($\chi^{(2)}$) nonlinear media is commonly used as a source of both broadband and broadly tunable coherent light at wavelengths that are difficult to access with laser gain media. Typical systems based on optical parametric amplification are used to produce ultrashort pulses in the mid-infrared (MIR) region [1–7], where coherent sources are desirable for rovibrational spectroscopy and sensing [8,9]. In almost all applications, both efficient and broadband operation is necessary to realize useful light sources. At this time, common approaches include aperiodic poling [10–14], chirped pulse amplification [15,16], or adiabatic frequency conversion [17–20], all of which have been reported to achieve both large conversion efficiencies and broad bandwidths. However, in bulk nonlinear media these approaches require large pump pulse energies and peak powers, which are typically delivered by complex, expensive, and bulky amplified laser systems. The large footprint and power requirements of OPA-based systems has precluded their use outside of photonics laboratories, where bench-top or field-deployable systems that consume milliwatts of power are desired.

In principle, these limitations can be removed by leveraging recent progress in thin-film lithium niobate [21], which has led to the development of efficient degenerate OPAs that operate with ultra-low pump powers [22,23]. Power reductions in these thin-film devices have been achieved by combining wavelength-scale transverse confinement with dispersion engineering [24–26]. By using the waveguide geometry to eliminate temporal walk-off between the pump and the degenerate signal, these systems can realize arbitrarily long interaction lengths for femtosecond pulses, which has enabled saturated degenerate OPA with picojoules [22], rather than nanojoules, of pump pulse energy. Further engineering of higher-order dispersion has enabled extremely large parametric gains across an octave of bandwidth [22,23]. A natural question, then, is how to extend these benefits to non-degenerate OPA, where the interaction length is set by temporal walk-off between three pulses. In this case, using the waveguide geometry for dispersion engineering rarely gives sufficient control to simultaneously group-velocity-match all three waves.

In this work, we experimentally demonstrate an approach to non-degenerate OPA that enables arbitrarily long interaction lengths. Rather than achieving group-velocity matching between

the pump, signal, and idler, we engineer the group velocities of the signal and idler to walk off from the pump pulse in opposite directions. In this configuration, hereafter referred to as symmetric walk-off, the large parametric gain localized around the peak of the pump traps the generated signal and idler pulses to form a three-wave soliton. This process is robust with respect to perturbations of the waveguide dispersion relations, including realistic errors of the group velocity associated with each wave and the presence of higher-order dispersion. We note here that this approach is heavily inspired by previous demonstrations of OPA [5] that have used temporal gain-guiding [27–30] in bulk nonlinear media to realize both broadband and efficient parametric sources. In contrast to temporal gain guiding, the gain-trapped solitons that form in guided-wave devices have several advantages: (i) the devices demonstrated here operate with picojoules, rather than nanojoules, of pulse energy, and are therefore compatible with compact, high-repetition-rate pump lasers; (ii) the dispersion engineering available in wavelength-scale devices enables operation at any wavelength within the transparency window of the nonlinear medium; and (iii) in the absence of diffraction, the full input-output map of the OPA can be well approximated using a handful of modes that correspond to the gain-trapped solitons. This feature enables a concise description of both the underlying physics and the design principles of OPAs that operate in the gain-trapped regime. We further note that symmetric walk-off OPAs have been previously used in the low-gain regime to generate spectrally separable biphotons [31,32]. This work extends these treatments to the high-gain regime, where the gain-trapped signal and idler solitons may be used to generate pure two-mode squeezing.

This paper is organized into two main sections. First, in Section 2, we discuss the theory of gain-trapped solitons in a nanophotonic waveguide. In the absence of pump depletion, the coupled-wave equations (CWEs) for OPA are more naturally solved in the frequency domain, where they can be recast as a linear dynamical system describing the evolution of each Fourier component of the signal and idler fields. In this context, gain-trapped solitons can be identified as the eigenvectors of the system matrix with real eigenvalues. These solutions correspond to modes that extract large parametric gains during propagation without undergoing any changes to the shape of the associated pulse envelope.

Section 3 presents the first experimental study of gain-trapped solitons in integrated photonics. Here, we use a periodically poled thin-film lithium niobate on a sapphire nanowaveguide [33,34] to down-convert a femtosecond pump pulse centered around 1045 nm to broadband signal and idler photons centered around 1560 and 3200 nm, respectively. When driven with 80-fs pump pulses from a mode-locked Yb: fiber laser, we observe unsaturated gains as large as $30 \text{ dB}/\sqrt{\text{pJ}}$ in a 5-mm-long waveguide. When seeded with a continuous-wave (CW) telecom laser, saturation occurs with as little as 5.5 pJ of pump pulse energy, which corresponds to a gain coefficient as large as 140 dB/cm. In the saturated regime the three-wave soliton breaks up, which causes the signal and idler to undergo temporal walk-off. This saturated behavior reduces back-conversion by sum-frequency generation. In this limit, we observe photon conversion efficiencies as large as 50%. The down-converted signal and idler each have 3-dB bandwidths of 5 THz, which support transform-limited pulse durations as short as 70 fs.

This approach to dispersion engineering is general and can be extended to almost any wavelength range within the transparency

window of the nonlinear medium. We expect this technique to be useful in any integrated photonics platform that offers sufficient flexibility to realize dispersion-engineered nonlinear interactions. In principle, the extension of temporal gain-trapping to material systems such as orientation-patterned thin films of InGaP or AlGaAs can enable both efficient and broadband sources operating at any mid-infrared wavelength.

2. THEORY AND DESIGN

To better motivate the model used throughout this article, we first consider a qualitative comparison between the observed behaviors of conventional and gain-trapped OPAs in Fig. 1. If, for simplicity, we consider the case where the group-velocity mismatch between the pump and signal pulses ($\Delta k'_s = v_{g,s}^{-1} - v_{g,p}^{-1}$) is equal to that of the idler and pump ($\Delta k'_i = \Delta k'_p$), then a signal pulse seeded at the input of the waveguide generates a co-propagating idler pulse as shown in Fig. 1(b). In this case OPA is naturally modeled by integrating the time-domain coupled-wave equations [Eqs. 1(a) and 1(b)] along a characteristic, as in [35]. Here, the signal and idler pulses will extract gain for an interaction length given by $L_{\text{int}} \approx \tau/\Delta k'_s$, where τ is the pulse duration of the pump. In contrast, Fig. 1(c) shows the behavior of gain-trapped OPA where the signal and idler pulses are assumed to undergo symmetric walk-off ($\Delta k'_s = -\Delta k'_i$). Here, the large field intensity near the peak of the pump amplifies the tails of the signal and idler pulses, which effectively pulls the centroid of each pulse in towards the pump. In the limit of large parametric gain, this effect can completely cancel the temporal walk-off of the signal and idler, thereby realizing arbitrarily long interaction lengths [5]. Remarkably, this process can be shown to be robust with respect to the boundary conditions of the waveguide; when a weak CW laser is used to seed the signal, the pump pulse amplifies this seed into coherent gain-trapped signal and idler pulses as shown in Fig. 1(d).

The observation that gain-trapping occurs in the undepleted limit motivates a frequency-domain model, where solutions to the coupled-wave equations can be obtained for arbitrary dispersion relations. This approach converts the time-domain coupled-wave equations, a system of three partial-differential equations, into a large linear dynamical system that describes the coupling between the Fourier components of each wave. In this context, the gain coefficient and shape of the gain-trapped solitons are completely characterized by the corresponding eigenvalues and eigenvectors of a linear operator. We note here that closed-form solutions for gain-trapped solitons have been obtained for three waves undergoing spatial walk-off in [36], and for three pulses undergoing temporal walk-off in [37]. We start with the time-domain CWEs for the signal and idler, assuming an undepleted pump:

$$\begin{aligned} \partial_z A_s(z, t) = & -i\kappa_s A_p(t) A_i^*(z, t) \exp(-i\Delta k_0 z) - (i\hat{D}_s(\partial_t) \\ & + \Delta k'_s \partial_t) A_s(z, t), \end{aligned} \quad (1a)$$

$$\begin{aligned} \partial_z A_i(z, t) = & -i\kappa_i A_p(t) A_s^*(z, t) \exp(-i\Delta k_0 z) - (i\hat{D}_i(\partial_t) \\ & + \Delta k'_i \partial_t) A_i(z, t), \end{aligned} \quad (1b)$$

where A_s , A_i , and A_p are the complex field amplitudes of the signal, idler, and pump, respectively, normalized such

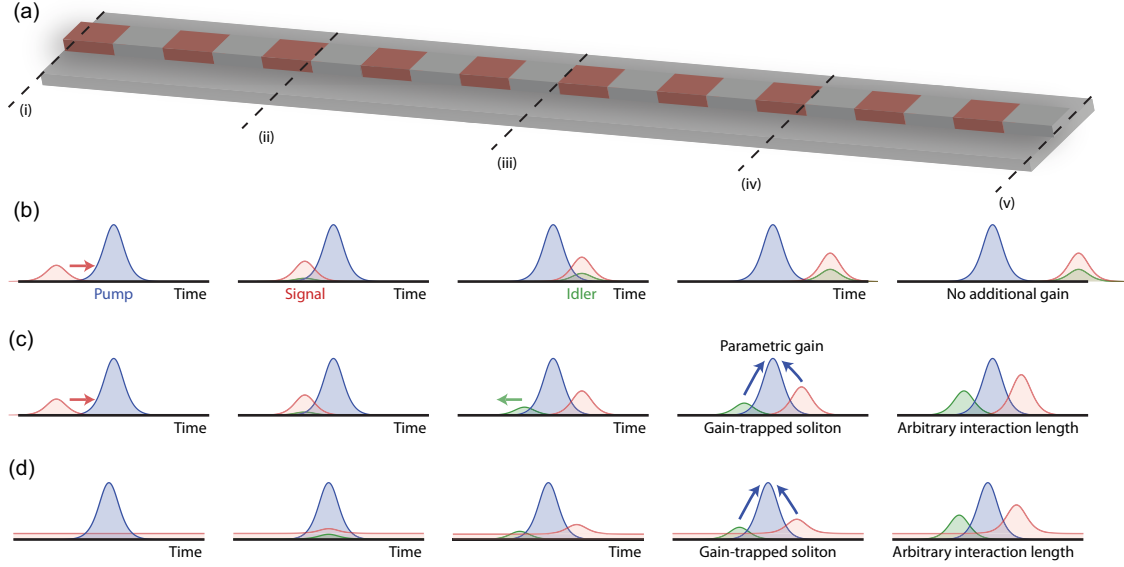


Fig. 1. (a) We contrast the behaviors of gain-trapped OPA with conventional OPA during propagation from the input of a waveguide (i) to the output (v). (b) For a co-propagating signal and idler ($\Delta k'_s = \Delta k'_i$), a seeded signal pulse (red) walks through the pump pulse (blue), and generates a weak idler pulse (green) for a finite interaction length in which the three pulses overlap with the pump. (c) In the symmetric walk-off regime ($\Delta k'_s = -\Delta k'_i$), the large parametric gain located around the peak of the pump amplifies the overlapping tails of the signal and idler pulses, which draws the centroid of each pulse in towards the peak of the pump to form a gain-trapped soliton. This process enables arbitrarily long interaction lengths in the undepleted limit. (d) Gain-trapped solitons form for a wide variety of boundary conditions. When seeded by a continuous-wave laser, the pump generates a pulse of signal and idler, which become trapped as in (c).

that $|A(z, t)|^2$ has units of Watts and corresponds to the instantaneous power contained in the corresponding wave. $\Delta k_0 = k_p(\omega_p) - k_s(\omega_s) - k_i(\omega_i) - 2\pi/\Lambda_g$ is the phase-mismatch for three-wave mixing evaluated at the carrier frequencies of the pump (ω_p), signal (ω_s), and idler (ω_i). Λ_g is the grating period used for quasi-phase-matching. We note here that the subscripts associated with the propagation constants are meant to convey that each wave can have different dispersion relations. The dispersion operator $\hat{D}_\mu(\partial_t) = \sum_{j \geq 2} ((-i)^j k_\mu^{(j)} / j!) \partial_t^j$ contains contributions from second and higher dispersion orders. Here, $k_\mu^{(j)}$ represents the j^{th} derivative of the propagation constant k_μ at the central frequency of the corresponding wave, ω_μ . The nonlinear coupling, κ_μ , is given by

$$\kappa_\mu = \frac{\sqrt{2Z_0}\omega_\mu d_{\text{eff}}}{c\sqrt{n_p n_s n_i} A_{\text{eff}}}, \quad (2)$$

where Z_0 is the impedance of free space, $d_{\text{eff}} = 2d_{33}/\pi$ is the effective nonlinear coefficient for a PPLN grating of 50% duty cycle, and n_μ is the effective refractive index of a guided TE₀₀ mode at the respective pump, signal, and idler frequency. A_{eff} is the effective interaction area [24], which accounts for the overlap between the interacting modes.

In the absence of pump depletion, the coupled-wave equations can be solved for by expanding each envelope into a Fourier series, $A_s(z, t) = \sum_m A_{s,m} \exp(2\pi i m t / T)$, where $T = f_{\text{rep}}^{-1}$ is the repetition period of the pump laser. Here, each Fourier component is given by $A_{s,m}(z) = \frac{1}{T} \int_0^T A_s(z, t) \exp(-2\pi i m t / T) dt$. By defining flux amplitudes $a_{s,m} = A_{s,m} / (\hbar\omega_{s,m})^{1/2}$, where $\omega_{s,m} = \omega_s + 2\pi m / T$, and moving into a rotating frame given by

$\tilde{a}_{s,m} = a_{s,m} \exp(-i\Delta k_0 z / 2)$, the coupled-wave equations become a translation-invariant linear dynamical system:

$$\partial_z \begin{pmatrix} \vdots \\ \tilde{a}_{s,m}(z) \\ \vdots \\ \tilde{a}_{i,n}^*(z) \\ \vdots \end{pmatrix} = \begin{pmatrix} \ddots & & & & \\ & -i\Delta k_{s,m} & & & \\ & & \ddots & & \\ & & & \gamma_{mn} & \\ & & & & \ddots \\ \gamma_{nm} & & & & & i\Delta k_{i,n} \\ & & & & & & \ddots \end{pmatrix} \begin{pmatrix} \vdots \\ \tilde{a}_{s,m}(z) \\ \vdots \\ \tilde{a}_{i,n}^*(z) \\ \vdots \end{pmatrix}. \quad (3)$$

Throughout this paper, Eq. (3) will be written more succinctly as $\partial_z \tilde{\mathbf{a}}(z) = M \tilde{\mathbf{a}}(z)$, where M is the system matrix that describes the evolution of the signal and idler modes. The diagonal of M contains contributions to the phase-mismatch from the dispersion relations of the signal and idler waves, $\Delta k_{s,m} = \frac{1}{2} \Delta k_0 - \Delta k'_s \Omega_m - \hat{D}_s(i\Omega_m)$, where $\Omega_m = 2\pi m / T$. The off-diagonal blocks contain couplings between the signal and idler modes by each Fourier component of the pump, $\gamma_{mn} = -i\sqrt{\kappa_s \kappa_i} A_{p,m+n}$, where $-iA_{p,m+n}$ can be assumed to be real for an unchirped pump. Equation (3) can be non-dimensionalized by rescaling any length scale by the peak gain coefficient $\gamma_{\text{pk}} = \sqrt{\kappa_s \kappa_i} \max(|A_p(t)|)$, and any time or bandwidth scale by the duration of the pump pulse τ . We note here that the use of discrete Fourier modes is a mathematical convenience, and that the pulse repetition rate does not contribute to the dynamics beyond setting the average power required to obtain a given pulse energy. In the absence of higher-order dispersion, and for a given shape of the pump pulse, the solutions are characterized

completely by the gain-per-walk-off, $\gamma_{\text{pk}}2\tau/(\Delta k'_s + \Delta k'_p)$, and the walk-off asymmetry, $(\Delta k'_s - \Delta k'_p)/(\Delta k'_s + \Delta k'_p)$.

A. Gain-Trapped Solitons

The behaviors of pulsed OPAs operating in the high-gain regime are typically analyzed in terms of a basis of broadband input and output modes [38–40]. Here, Eq. (3) is solved with a matrix exponential, $\tilde{\mathbf{a}}(z) = \exp(Mz)\tilde{\mathbf{a}}(0)$, where $\exp(Mz)$ is commonly referred to as the Green's function of the OPA since the columns of $\exp(Mz)$ correspond to the impulse response of M [41,42]. The Green's function is typically calculated using an eigenvalue decomposition, $M = W\Lambda W^{-1}$, which allows us to rewrite $\exp(Mz) = W\exp(\Lambda z)W^{-1}$. In practice, the structure of the Green's function is not typically studied in terms of eigenvalues and eigenvectors since W is not a unitary matrix; W^{-1} does not project the input field onto a basis of eigenmodes. Instead, $\exp(Mz) = U\Sigma V^\dagger$ is decomposed into a basis of input and output modes using the singular value decomposition, where U and V are unitary matrices, \dagger denotes the Hermitian conjugate, and Σ is a diagonal matrix of singular values [43,44]. This approach enables an intuitive picture of pulsed OPA: the unitary matrix V^\dagger projects the input fields into a basis of input modes, v_i , each of which is then rescaled by the singular values, Σ_{ii} , before being reconstituted into the output fields by u_i . We note here that in almost every case, the input modes, output modes, and singular values associated with the Green's function $\exp(Mz)$ are functions of the propagation length, z .

In the context of gain-trapped solitons we are interested in identifying a subset of modes that propagate without changing shape. For these states the input modes and output modes are invariant with respect to z . In this case the eigenvalue decomposition is better suited for analyzing the structure of M since the eigenvectors w_i do not depend on z . Our goal is to understand the conditions under which a subset of eigenvectors of M becomes singular vectors of $\exp(Mz)$. When Eq. (3) is non-dimensionalized to the nonlinear length, γ_{pk}^{-1} , we find that the system matrix M becomes Hermitian in the limit as $\gamma_{\text{pk}} \rightarrow \infty$. In this limit, the eigenvalues of M are real and the eigenmodes form an orthonormal basis with $U = W = V$. Put simply, in the high-gain limit the parametric gain dominates over the temporal walk-off and dispersive pulse spreading described by $\Delta k_{s,m}$ and $\Delta k_{i,m}$, and every mode becomes a gain-trapped soliton. This behavior suggests that as the parametric gain is increased, the eigenmodes of the OPA system matrix undergo a transition from linearly propagating Fourier modes to gain-trapped solitons. In all further discussion the terms gain-trapped soliton and gain-trapped eigenmode will be used interchangeably, since these solitons are eigenfunctions of a linear operator.

To better clarify the transition from linear propagation to gain-trapping, Fig. 2 shows the eigenvalue structure of a symmetric walk-off OPA as a function of the input pump pulse energy. Here, for simplicity, we have ignored dispersion beyond temporal walk-off, and have chosen typical values for the nonlinearity ($\kappa_s, \kappa_i = 488\%/W - \text{cm}^2$), pump pulse duration (80 fs), and group-velocity mismatch ($\Delta k'_s = -\Delta k'_i = 50 \text{ fs/mm}$) for a dispersion-engineered nanowaveguide. In the absence of any nonlinear coupling ($U_{\text{in}} = 0 \text{ pJ}$), the eigenvalues are purely imaginary [Fig. 2(b, i)], corresponding to the propagation constant of each Fourier mode in the rotating frame. The eigenvectors associated with these continuum modes are each a delta function in frequency

[Fig. 2(c, i)]. For a weakly driven waveguide [Figs. 2(a, ii)–2(c, ii)], signal and idler pairs within the OPA gain bandwidth acquire a real part, corresponding to either amplified or de-amplified continuum modes for positive and negative values of the real part, respectively. As the pump pulse energy is increased, the gain of the continuum modes exhibits a turning point around 0.8 pJ. At this point, the eigenvalue associated with the highest-gain eigenmode becomes purely real, and the power spectrum associated with this mode broadens to form a localized pulse [Figs. 2(a, iii)–2(c, iii)]. The singular vectors undergo a similar transition, with $u_i \approx w_i$ for the gain-trapped eigenmodes, and $\Sigma_{ii} \approx \exp(\Lambda_{ii}L)$. We note here that the formation of an amplified eigenmode is always accompanied by the formation of a de-amplified mode, which is obtained by shifting the phase of the idler block of $\tilde{\mathbf{a}}$ relative to the signal block. With increasing pump power, the gain extracted by the continuum modes is suppressed, whereas the gain-trapped eigenmode exhibits a parametric gain that increases monotonically with increasing pump field. For pump pulse energies in excess of 5.5 pJ a second pair of gain-trapped eigenmodes forms. For the range of parameters considered here, the amplified continuum modes never extract more than 5 dB/cm of gain, whereas the first-order gain-trapped soliton may experience unsaturated gains far in excess of 100 dB/cm.

In a qualitative sense the eigenvalue structure of a gain-trapped OPA resembles that of the spatial modes found in a planar waveguide, with the time coordinate now playing the role of the transverse spatial coordinates. In the latter case, the waveguide has a continuum of unguided modes, each described largely by a single spatial k-vector, and a finite number of guided modes, each containing a superposition of many k-vectors. The number of guided modes is determined by the index contrast of the waveguide, with more modes confined to waveguides with greater index contrast. In the context of pulsed OPA, the parametric gain plays the role of index contrast, with large parametric gains corresponding to a greater number of gain-trapped eigenmodes. As with spatial modes, the gain trapped eigenmodes each contain many Fourier components, whereas the amplified continuum modes are well localized in frequency. This analogy between gain-trapped eigenmodes and waveguide modes will be made more explicit when we study the Green's function of the OPA in Section 3.

B. Design

To demonstrate parametric down-conversion by gain-trapped solitons, we use geometric dispersion engineering in a periodically poled thin-film lithium niobate on sapphire nanowaveguide. Here, the geometry is chosen to achieve symmetric walk-off between a set of pump, signal, and idler wavelengths that are easily accessed using turn-key sources. We choose a pump wavelength of 1045 nm and a signal wavelength of 1560 nm, since both of these wavelength ranges are readily addressed by both femtosecond and broadly tunable sources. The resulting idler wavelength is centered on 3200 nm. Figure 3(a) shows the nominal geometry of the waveguide, with the transverse magnetic field (H_y) plotted for the pump, signal, and idler. The waveguide has a top width of 2885 nm, an etch depth of 650 nm, and a film thickness of 1041 nm. This choice of waveguide geometry was determined by simulating the walk-off asymmetry, $\Delta k'_s + \Delta k'_i$, as a function of waveguide width, film thickness, and etch depth, and choosing a value of waveguide geometry around which $\Delta k'_s + \Delta k'_i = 0$ [Fig. 3(b), white region]. We find that symmetric walk-off occurs

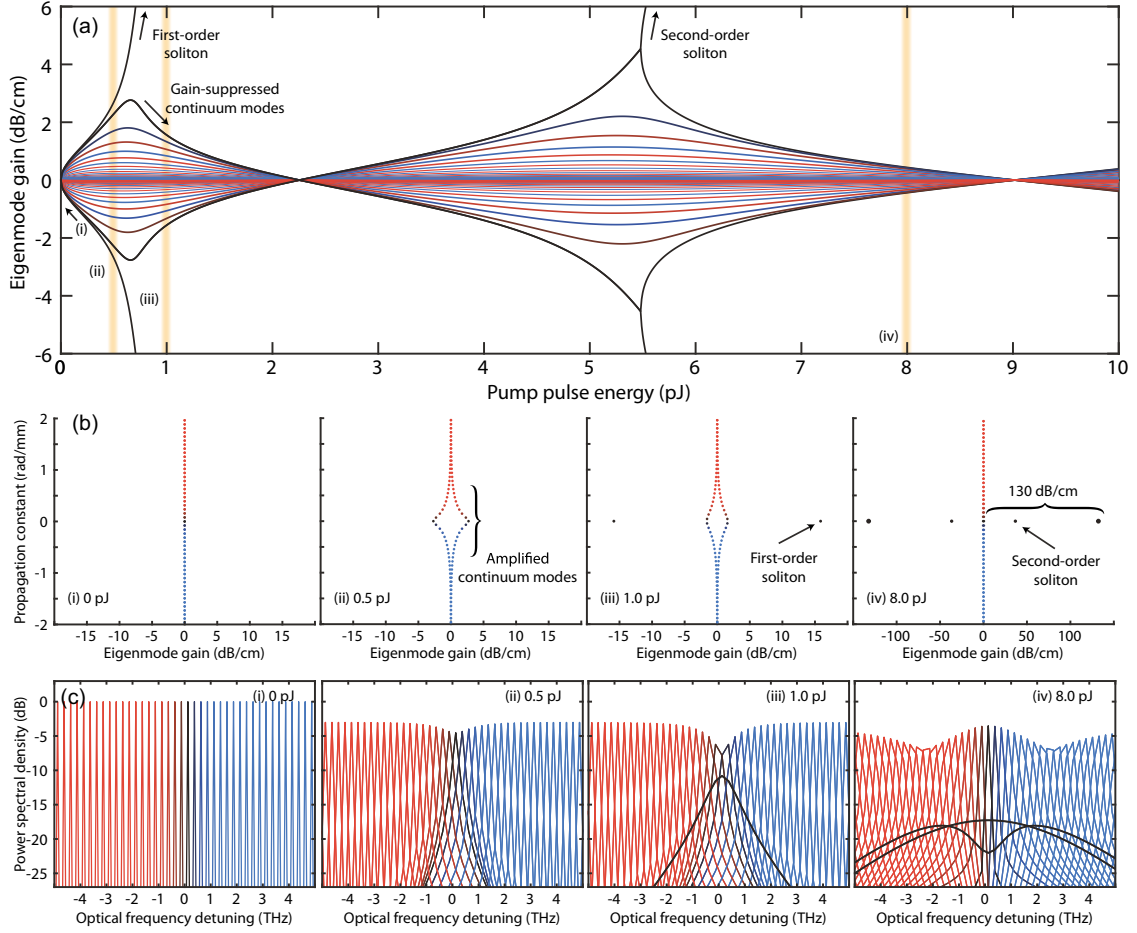


Fig. 2. (a) Real part of the eigenvalue associated with each eigenmode (quoted as a parametric gain in dB/cm) as a function of pump pulse energy. Each line is colored by the imaginary part of the eigenvalue, corresponding to the propagation constant of the eigenmode in the rotating frame. (b) Complex eigenvalues of each mode for select pulse energies. (c) Optical power spectra associated with each of the eigenvectors, here plotted for a band of frequencies centered on the signal wavelength. The threshold of gain-trapping is observed at a pump pulse energy of 0.8 pJ. Above threshold, the gain-trapped eigenmode is characterized by a broad spectrum, as evidenced by the black lines in (c, iii) and (c, iv). For a weaker drive field, the pump amplifies a continuum of modes, well approximated by Fourier modes. For pump pulse energies in excess of 0.8 pJ, we observe the formation of an amplified and de-amplified pair of gain-trapped modes. Second-order gain-trapped solitons form for pulse energies in excess of 5.5 pJ.

for the combination of relatively thick (1040-nm) films and deep (650-nm) etch depths. The devices fabricated for experimental study in the following sections [Fig. 3(b), black cross mark] had a simulated GVM of $\Delta k'_s = 40$ fs/mm and $\Delta k'_i = -30$ fs/mm. The simulated group-velocity dispersions of the pump, signal, and idler are $k''_p = 165$ fs²/mm, $k''_s = -75$ fs²/mm, and $k''_i = 320$ fs²/mm, respectively.

Given the small walk-off asymmetry and group-velocity dispersion present in any real device, a natural question is how robust gain-trapped solitons are with respect to deviations from the idealized dispersion relations considered in Section 2. To this end, Fig. 3(c) plots the gain coefficient of the dominant eigenmode as a function of $\Delta k'_s$ and $\Delta k'_i$, for a pump pulse energy of 1 pJ. A key characteristic of gain trapping is that the calculated gain coefficient of the dominant eigenmode, as given by the largest real part of any eigenvalue, is an extremely weak function of $\Delta k'_s$ and $\Delta k'_i$, provided that $\Delta k'_s$ and $\Delta k'_i$ have opposite signs. In this regime, the

gradient of the dominant eigenvalue with respect to $\Delta k'_s$ and $\Delta k'_i$ is close to zero [i.e., $\nabla \text{Re}(\Lambda_{\max}) \approx [0.05, 0.05]$ dB/fs for the values in Fig. 3(c)]. In contrast, for conventional OPA with $\Delta k'_s = \Delta k'_i$, the gain coefficient of the dominant eigenmode is extremely sensitive to small errors in waveguide geometry. In this region, the gradient of the gain coefficient can be as much as 30 times larger than in the gain-trapped regime ($\nabla \text{Re}(\Lambda_{\max}) \approx [1.5, 1.5]$ dB/fs). In addition to plotting the dominant eigenmode gain as a function of group-velocity mismatch, we also consider the gain contrast given by the difference between the real parts of the two largest eigenvalues in Fig. 3(d). This provides a measure of the extent to which the gain is still localized in one mode, rather than distributed across many modes. Here, we find that the gain contrast exceeds 10 dB/cm for all configurations with $|\Delta k'_s| > 5$ fs/mm and $|\Delta k'_i| > 5$ fs/mm, provided $\Delta k'_s$ and $\Delta k'_i$ have opposite signs. Finally, we verify that these figures are largely unchanged by the

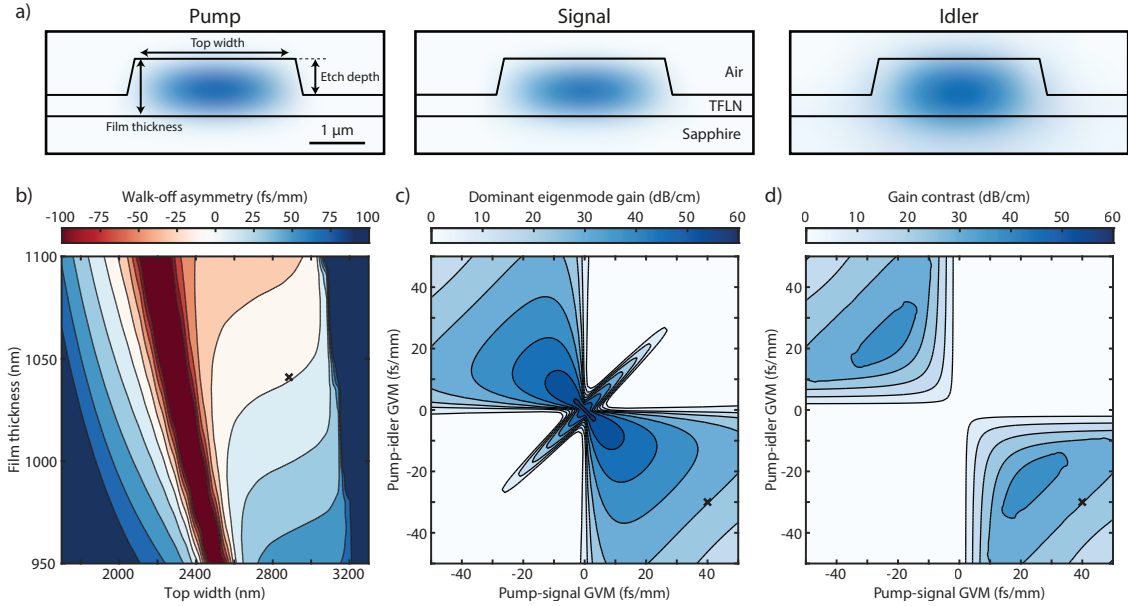


Fig. 3. (a) Transverse magnetic field (H_y) of the pump, signal, and idler waves, here for the waveguide geometry studied in the following sections. The top width is 2885 nm, the etch depth is 650 nm, and the film thickness is 1041 nm. (b) GVM asymmetry ($\Delta k'_s + \Delta k'_i$) as a function of the top width and film thickness, for a fixed etch depth of 650 nm. Here the contours correspond to steps of 20 fs/mm, with the white-colored region denoting designs that achieve near-symmetric walk-off ($|\Delta k'_s + \Delta k'_i| < 10$ fs/mm). (c) Dominant eigenmode gain (Λ_{\max}) and (d) gain contrast plotted as a function of the pump-signal and pump-idler GVM, $\Delta k'_s$ and $\Delta k'_i$, respectively. The dominant eigenmode is defined as the mode exhibiting the highest gain, and the gain contrast refers to the difference between the gain coefficients of the two most strongly amplified modes. Black cross: fabricated waveguide.

inclusion of realistic values of second- and third-order dispersion, such as the simulated GVD values above and TOD values in excess of 1000 fs³/mm. Together, these behaviors suggest that gain-trapped solitons form and propagate stably in the presence of a wide variety of dispersion relations, including waveguides with weakly asymmetric walk-off and both second- and third-order dispersion.

3. EXPERIMENTAL RESULTS

We fabricated 23 identical 5-mm-long waveguides with poling periods ranging from 7.883 to 8.323 μm in steps of 20 nm using the methods described in [33]. In all of these devices, the waveguide is tapered from 500 nm at the input facet to the nominal width of 2885 nm to ensure that the pump and signal inputs to the waveguide are all in the TE₀₀ mode. The output facet is left untapered to ensure that the pump power, signal power, and idler power at the end of the waveguide are collected with comparable efficiency. We note here that before studying gain-trapping, the dispersion relations of the waveguides are first verified using continuous-wave difference frequency generation between tunable 1045- and 1560-nm lasers, as described in Supplement 1. We observe phase-matching for poling periods in the vicinity of 8.243 μm , and the change of the phase-matched signal wavelength with tuning of the pump wavelength is consistent with symmetric walk-off.

A. Gain-Trapped Eigenfunctions

To verify the formation of gain-trapped solitons, we first measure the power spectral density generated around 1560 nm by OPA as a function of seed wavelength, as shown in Fig. 4(a). Here the pump consists of 80-fs-long pulses centered around 1045 nm delivered by a mode-locked fiber laser with a repetition rate of 100 MHz (Menlo Systems Orange A). The continuous-wave seed is provided by a pair of tunable C-band and L-band lasers (Newfocus Vidia-swept) with a combined spectral range spanning from 1520 to 1625 nm. The pump and signal lasers are separately collimated from fiber into free space, where each beam path can be separately attenuated using half-wave plates and polarizing beam-splitters. The two lasers are also passed through separate mode-matching telescopes before being combined on a dichroic beam-splitter. The combined beams are coupled into and out of the waveguide using a reflective objective (Thorlabs LMM-40x-P01), which avoids both chromatic aberration and excessive group-delay dispersion. We note here that the center obscuration associated with a reflective objective limits the throughput of any input Gaussian beam to $\sim 30\%$, and the weak overlap of the focused Gaussian beam limits the total launching efficiency to $\sim 1.6\%$. The collection efficiencies on the output are limited only by the finite (0.5) NA of the reflective objective and the center obscuration, which allows relatively large collection efficiencies of 20% for the pump, 33% for the signal, and 40% for the idler [34]. In all further discussions the power values, pulse energies, and conversion efficiencies are reported inside the waveguide using the above coupling and collection efficiencies. For measuring the generated power spectra, the three waves are collected into a 1-m-long multimode InF₃ fiber using the reflective objective, and sent to optical spectrum analyzers. We use both a

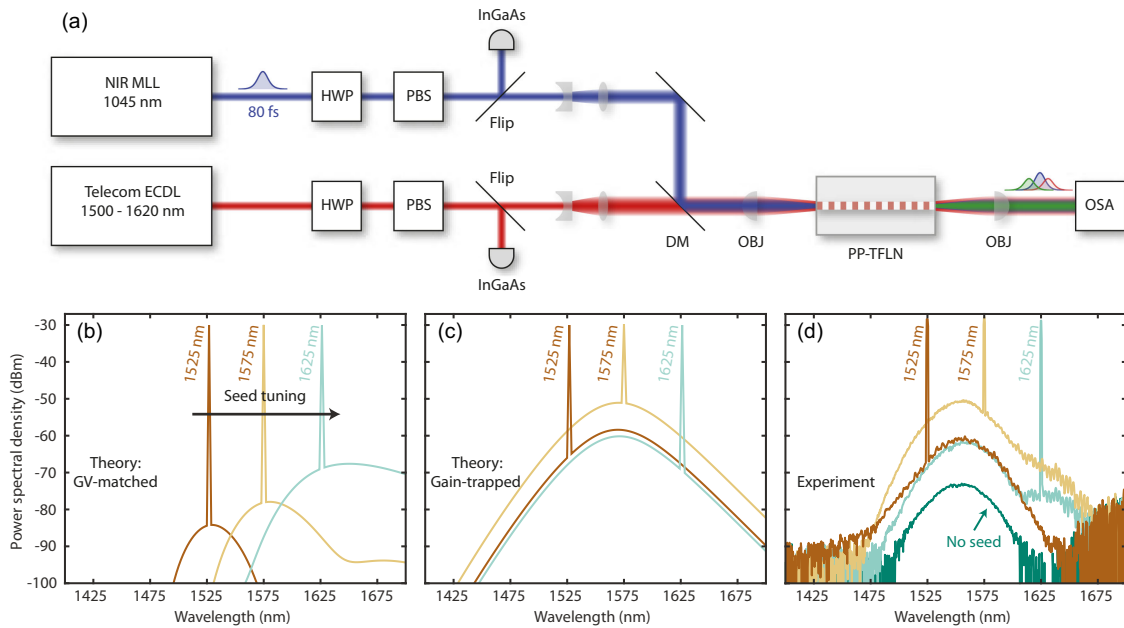


Fig. 4. Power spectral density of the generated signal as a function of seed wavelength. (a) Experimental setup. HWP: half-wave plate, PBS: polarizing beam-splitter, OBJ: metallic objective, DM: dichroic mirror, PP-TFLN: periodically poled thin-film lithium niobate waveguide, OSA: optical spectrum analyzer. (b) Theoretical power spectra as a function of seed wavelength for a co-propagating signal and idler ($\Delta k_s = \Delta k_i$). Here, the generated power spectra are expected to exhibit a strong dependence on the seed wavelength. (c) Theoretical power spectra generated by symmetric walk-off OPA. In this case, the shape of the power spectrum is invariant with respect to seeding conditions. The intensity of the generated power spectrum is determined by the overlap between the seed and the dominant OPA eigenfunction. (d) Experimental results for the fabricated waveguide, showing extremely weak dependence of the generated power spectrum on the seed wavelength. The shoulders present above 1625 nm and below 1525 nm are due to amplified spontaneous emission accompanying the input seed, and are present when the pump is turned off.

Yokagawa AQ6370D and a Yokagawa AQ6376E to fully cover the spectral range from 600 to 3400 nm.

We can distinguish the behaviors of gain-trapped OPA from conventional optical parametric amplifiers by considering the influence of the seed wavelength on the generated power spectral density. An example of the theoretical tuning behavior for conventional OPA with $\Delta k_s = \Delta k_i = 50$ fs/mm is shown in Fig. 4(b). Here, as one may intuitively expect, the wavelengths generated by OPA are localized around the seed laser with a bandwidth comparable to that of the pump laser. In contrast, in gain-trapped OPA the Green's function is well approximated by the dominant eigenmode, $\exp(Mz) \approx U \Sigma' U^T$, where $\Sigma' = \text{diag}(\Sigma_{11}, 0, 0, \dots)$ is the low-rank approximation of Σ retaining only the first principal component. In this limit, the shape of the power spectral density generated by OPA is invariant with respect to the seed wavelength, as shown in Fig. 4(c). Here, tuning the seed wavelength simply changes the overlap between the dominant eigenmode and the seed, thereby changing the intensity of the generated power spectrum without modifying its shape. We may extend our previous analogy of a planar waveguide to the observed behaviors of these two regimes of OPA: gain-trapped OPA behaves analogously to a single-mode waveguide where misalignment between an input beam and the waveguide mode only modifies the brightness of the transmitted light. Conventional OPA behaves like a highly multimode waveguide, where the shape of the light output from the waveguide is a strong function of the misalignment between the waveguide facet and the input beam. The experimentally measured

power spectrum generated by OPA as a function of seed wavelength is shown in Fig. 4(d) for a pump pulse energy of 4 pJ. Here we observe good agreement between experiment and the behavior expected of gain-trapped OPA; the shape of the power spectrum between 1525 and 1600 nm is unchanged by the wavelength of the seed laser, with a peak wavelength of 1555 nm and a 3-dB width of 38 nm. We only observe minor shifts in the tails of the generated power spectrum as the seed wavelength is shifted far away from the OPA peak. We note here that the power spectrum generated in the presence of a seed laser is 20–30 dB brighter than the spontaneous parametric fluorescence generated in the absence of any seed laser [Fig. 4(d), solid teal line], despite the weak overlap between the broadband eigenmode and the single-frequency laser.

B. OPA Characterization

Having verified the formation of gain-trapped signal and idler solitons, we now characterize the gain, bandwidth, and conversion efficiency attainable by gain-trapped OPA. The experimental setup, shown in Fig. 5(a), now has independent collection paths for the out-coupled pump, signal, and idler beams, which are separately measured by amplified silicon, InGaAs, and PbSe photoreceivers, respectively. For the InGaAs detector we use a long-pass filter (Thorlabs FELH1350) to prevent any 1- μ m light from reaching the detector. Similarly, a coated germanium window is used to prevent any pump and signal photons from reaching the PbSe detector. The pump laser is chopped to facilitate lock-in detection of the down-converted signal and idler photons. In

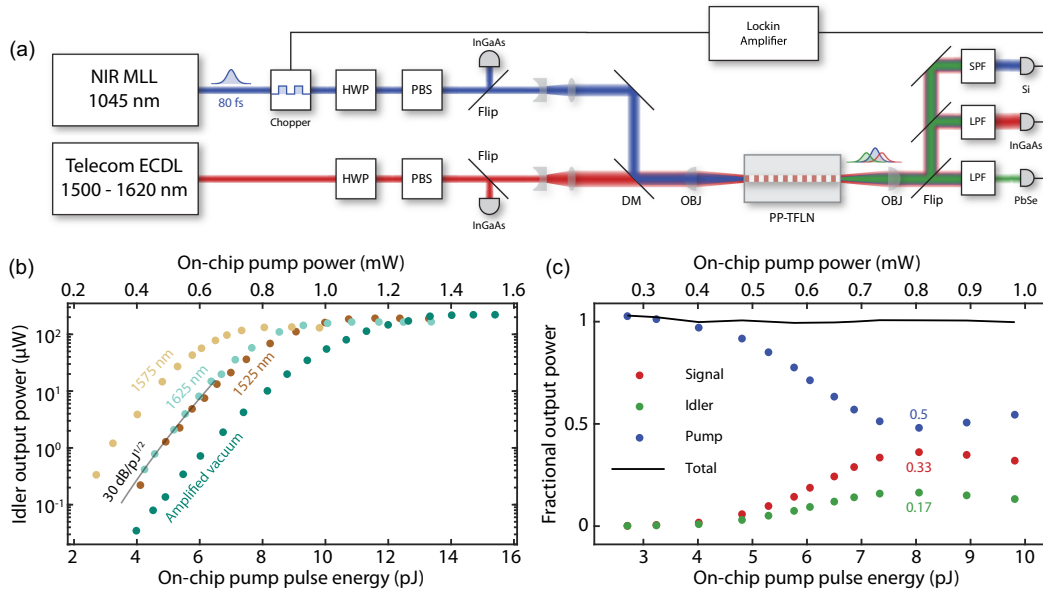


Fig. 5. Generated power. (a) Experimental setup. HWP: half-wave plate, PBS: polarizing beam-splitter, OBJ: metallic objective, PP-TFLN: periodically poled thin-film lithium niobate waveguide, LPF: long-pass filter. (b) Idler output power versus pump pulse energy obtained using seed wavelengths of 1525 nm (brown), 1575 nm (gold), 1625 nm (light blue), and without seed (green). In the unsaturated regime, the four lines are parallel, which indicates they display a similar gain coefficient found to be around $30 \text{ dB}/\sqrt{\text{pJ}}$ from the fit (gray). (c) Fractional on-chip pump (blue), signal (red), and idler (green) output power as a function of the pump pulse energy, obtained at the peak seed wavelength of 1575 nm.

addition to improving the detection sensitivity, this removes the background detected by the InGaAs detector due to the CW seed laser, which enables more accurate measurements of the OPA gain and efficiency.

Figure 5(b) shows the generated idler output power for the four seeding configurations used in Fig. 4(d). In the unsaturated regime, we observe the expected exponential growth of the output power generated by OPA with respect to the input pump pulse energy. Furthermore, the four configurations show identical fitted gain coefficients of $30 \text{ dB}/\sqrt{\text{pJ}}$. This again verifies the gain-trapping mechanism. In multimode OPA, changing the seed wavelength should excite different OPA eigenmodes with correspondingly different gain coefficients. Here, since the Green's function is dominated by one gain-trapped eigenmode, changing the seed wavelength only changes the overlap with this eigenmode, which manifests as an overall shift of the signal power without modifying the gain coefficient [Fig. 5(b)]. We observe the highest conversion efficiency with respect to the input pulse energy for a seed wavelength of 1575 nm. The origin of this offset between the observed peak of the eigenfunction and the seed wavelength is likely due to cross-phase modulation between the pump and signal pulse, which phase-shifts the generated pulse relative to the CW seed [44].

The conversion efficiency of the OPA, as determined by the fractional pump, signal, and idler output power obtained for a seed wavelength of 1575 nm, is shown in Fig. 5(c). Here, we observe saturated OPA with input pulse energies as low as 5 pJ. A maximum pump depletion of 50% is obtained with 8 pJ, which results in a pump, signal, and idler power ratio of 50%, 33%, and 17%, respectively. Above 8 pJ, the generated signal and idler are sufficiently bright to undergo sum-frequency generation (SFG) within a walk-off length, which back-converts signal and idler

photons to the pump. We record a maximum generated average power of 320 and 155 μW for the signal and idler, respectively, obtained with 1.0 mW of pump power. We note here that tuning the seed wavelength does not change the maximum pump conversion efficiency. Here, the role played by the seed wavelength on the OPA dynamics is to simply reduce the power of the generated signal light in the *undepleted* limit. This reduction of the generated signal power increases the pump pulse energy required to reach saturation, without changing the dynamics or overall conversion efficiency that occurs in the saturated regime. We note here that the generated signal and idler power obtained in the saturated limit can be increased either by offsetting the seed wavelength or reducing the seed power, which increases the pump energy required to reach 50% depletion.

In the saturated limit, the signal and idler pulses are no longer trapped by parametric gain and undergo temporal walk-off. As a result, the power spectrum of the signal and idler generated in this regime can differ from that of a gain-trapped soliton. Figure 6 shows the evolution of the signal and idler spectrum with respect to the in-coupled pump pulse energy for a seed wavelength of 1575 nm using the setup in Fig. 4(a). For a relatively low pump pulse energy of 5 pJ, the signal spectrum is undistorted by pump depletion and has a 3-dB bandwidth of 40 nm, which corresponds to transform-limited pulse duration of 65 fs. We note here that the low signal-to-noise ratio of the idler power spectrum does not allow a precise measurement of the 3-dB spectral bandwidth. Fitting the idler spectrum obtained for a pump pulse energy of 6 pJ with a Gaussian function, we estimate a 3-dB spectral bandwidth around 185 nm. For pump pulse energies in excess of 5 pJ, we observe the formation of fringes and side-lobes centered around the peak of the signal and idler envelopes, which become more finely patterned

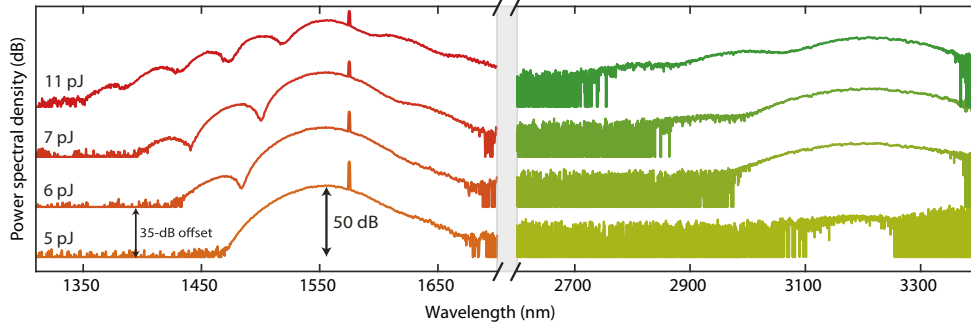


Fig. 6. Signal (red) and idler (green) power spectral densities obtained with different input pulse energies using the experimental setup shown in Fig. 4(a). The power spectral densities are offset by 35 dB for clarity. In the depleted limit, the power spectra form fringes that become more finely patterned with increasing pump power.

with increasing pump power. This process is well studied in the context of pulsed OPOs and occurs due to pump depletion in the saturated limit [35]. Here, the peaks of the signal and idler pulses back-convert to pump more rapidly than the tails, which causes the temporal envelope to flatten into a top-hat. This flattening of the pulse envelopes manifests as a sinc²-like function in the frequency domain. Increasing the pump pulse energy extends the window over which the pulse envelopes become flattened, thereby causing the zeros of the spectrum to move in towards to peak of the envelope. We note here that tuning the seed wavelength modifies this behavior by changing the degree of pump depletion; tuning the seed away from 1575 nm decreases the degree of pump depletion, thereby causing the fringes to become more coarse and move away from the peak. We close this section by noting that the idler bandwidth can become extremely broadband for large input pulse energies. At a maximum input pulse energy of 11 pJ and a seed wavelength of 1575 nm, we record an idler spectrum extending across 600 nm at the -20 -dB level.

C. Wavelength Tuning

Thus far, all of our studies of gain-trapped solitons have been carried out in a waveguide with an 8.243- μm poling period, which was chosen to phase-match OPA near 1560 nm. In this section, we briefly study the tunability of gain-trapped OPA by measuring the gain and bandwidth generated by OPA as a function of poling period. Changing the poling period tunes the phase-matching point to different wavelengths, and a natural question is how much

the bandwidth and gain may degrade as the phase-matched wavelengths are shifted. Figure 7(a) shows the power spectral density of the generated signal for three identical waveguides with poling periods of 8.203, 8.243, and 8.263 μm , which generate phase-matched OPA around 1495, 1555, and 1585 nm, respectively. The idler wavelength shifts accordingly to 3500, 3200, and 3100 nm, respectively, to maintain energy conservation between the pump, signal, and idler photons. The three power spectra display similar shapes, with 3-dB bandwidths ranging from 40 to 55 nm.

We separately verified that each of these waveguides exhibited gain-trapped OPA by verifying that the generated power-spectra were weak functions of the input seed wavelength. Then, having verified that each waveguide achieves gain-trapped OPA, we measure the gain coefficient of each waveguide by recording the power of the generated signal wave as a function of input pulse energy without any input seed. As before, the output power grows exponentially with the square-root of the input pulse energy in the unsaturated regime, and we find fitted gain coefficients of 23 dB/ $\sqrt{\text{pJ}}$, 30 dB/ $\sqrt{\text{pJ}}$, and 36 dB/ $\sqrt{\text{pJ}}$ for the three respective poling periods. This behavior can be intuited from our previous study of the OPA gain as a function of $\Delta k'_s$ and $\Delta k'_i$ in Fig. 3(d). Here, changing the poling period shifts the signal and idler wavelengths, which shifts $\Delta k'_s$ and $\Delta k'_i$ due to the presence of higher-order dispersion, $\Delta k'_s(\omega_s + \Delta\omega) \approx \Delta k'_s(\omega_s) + k''_s \Delta\omega$. Since $k''_s < 0$ and $k''_i > 0$, increasing the signal wavelength pushes both $\Delta k'_s$ and $\Delta k'_i$ towards 0 fs/mm, which increases the gain coefficient.

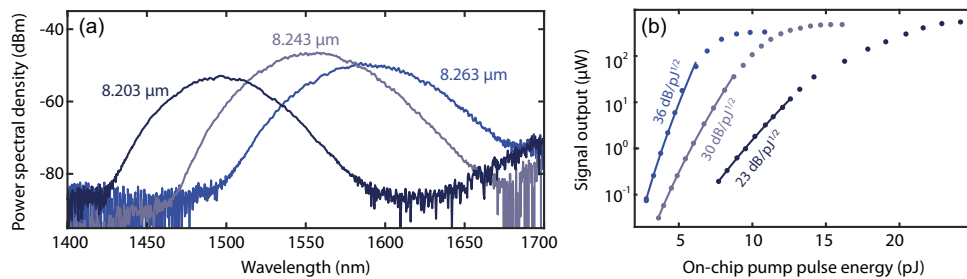


Fig. 7. (a) Power spectral density of the signal generated by optical parametric generation for waveguides with poling periods of 8.203 μm (dark blue), 8.243 μm (gray), and 8.263 μm (light blue). These power spectra were captured in the undepleted limit, using the setup shown in Fig. 4(a) with pump pulse energies of 13.5 pJ (dark blue), 8.5 pJ (gray), and 5.5 pJ (light blue). (b) Generated signal power as a function of input pump pulse energy for each poling period, as measured using the experimental setup shown in Fig. 5(a).

We note that for every poling period, we measured a maximum pump depletion of $\sim 50\%$, irrespective of the seeding condition. As a result, the high-gain configuration (light blue) leads to the lowest maximum generated signal power ($330 \mu\text{W}$), and conversely, the low-gain configuration (dark blue) reaches the largest output power ($550 \mu\text{W}$) since the low-gain configuration requires more pump power to achieve 50% depletion. Taken together, we find that gain-trapped OPA is robust with respect to tuning the phase-matched wavelength, and that all of the configurations studied here achieve both broad bandwidth and high conversion efficiency.

4. CONCLUSION

This work is the first experimental demonstration of parametric down-conversion by gain-trapped solitons in integrated photonics. This process is extremely robust to fabrication errors and higher-order dispersion, which enables efficient, high-gain, and broadband OPA at many different wavelengths simply by changing the poling period used for phase-matching. The devices demonstrated here achieve large parametric gains in excess of 70 dB (140 dB/cm) using only picoseconds of pump pulse energy, and we observe up to 50% pump depletion in the saturated regime. The mid-infrared idler formed by this process exhibits a broad spectrum extending over 600 nm at the -20 -dB level. Further engineering of the group velocities of the interacting modes should enable gain-trapped OPA at wavelengths beyond the ranges studied here. In principle, these devices represent a radically new approach to OPA that enables large parametric gains and broad gain bandwidths at arbitrary wavelengths, while utilizing exceptionally low pulse energies. The flexibility of this approach enables a host of new sources such as coherent mid-infrared frequency combs operating at multi-gigahertz repetition rates.

Funding. NTT Research Agreement (146395); National Science Foundation (GRFP-2146755); Schweizerischer Nationalfonds zur Förderung der Wissenschaftlichen Forschung (200021_188456, P400P2-194369); Defense Advanced Research Projects Agency (D19AP00040).

Acknowledgment. The authors wish to thank NTT Research for their financial and technical support. Part of this work was performed at the Stanford Nanofabrication Facility and the Stanford Nano Shared Facilities, supported by the National Science Foundation under award ECCS-2026822. Domain imaging and poling was performed in the Stanford Cell Sciences Imaging Facility, supported by the National Center for Research Resources under award S10RR02557401. A.Y.H. acknowledges the National Science Foundation for support under the Graduate Research Fellowship Program.

Disclosures. The authors declare no conflicts of interest.

Data availability. Data underlying the results presented in this paper are not publicly available at this time but may be obtained from the authors upon reasonable request.

Supplemental document. See Supplement 1 for supporting content.

REFERENCES

1. K. C. Burr, C. Tang, M. A. Arbore, *et al.*, "Broadly tunable mid-infrared femtosecond optical parametric oscillator using all-solid-state-pumped periodically poled lithium niobate," *Opt. Lett.* **22**, 1458–1460 (1997).
2. T. Südmeyer, E. Innerhofer, F. Brunner, *et al.*, "High-power femtosecond fiber-feedback optical parametric oscillator based on periodically poled stoichiometric LiTaO₃," *Opt. Lett.* **29**, 1111–1113 (2004).
3. S. Chaitanya Kumar, A. Esteban-Martin, T. Ideguchi, *et al.*, "Few-cycle, broadband, mid-infrared optical parametric oscillator pumped by a 20-fs Ti:sapphire laser," *Laser Photonics Rev.* **8**, L86–L91 (2014).
4. L. Maidment, P. G. Schunemann, and D. T. Reid, "Molecular fingerprint-region spectroscopy from 5 to 12 μm using an orientation-patterned gallium phosphide optical parametric oscillator," *Opt. Lett.* **41**, 4261–4264 (2016).
5. B. Luther-Davies and Y. Yu, "Efficient generation of ultra-short pulses in the infrared from a simple PPLN optical parametric amplifier," in *Nonlinear Optics* (Optica Publishing Group, 2017), paper NTu2A-4.
6. L. Lang, C. P. Bauer, C. R. Phillips, *et al.*, "51-W average power, 169-fs pulses from an ultrafast non-collinear optical parametric oscillator," *Opt. Express* **29**, 36321–36327 (2021).
7. C. P. Bauer, S. L. Camenzind, J. Pupeikis, *et al.*, "Dual-comb optical parametric oscillator in the mid-infrared based on a single free-running cavity," *Opt. Express* **30**, 19904–19921 (2022).
8. M. Vainio and L. Halonen, "Mid-infrared optical parametric oscillators and frequency combs for molecular spectroscopy," *Phys. Chem. Chem. Phys.* **18**, 4266–4294 (2016).
9. A. Muraviev, V. Smolski, Z. Loparo, *et al.*, "Massively parallel sensing of trace molecules and their isotopologues with broadband subharmonic mid-infrared frequency combs," *Nat. Photonics* **12**, 209–214 (2018).
10. C. Phillips, C. Langrock, D. Chang, *et al.*, "Apodization of chirped quasi-phase-matching devices," *J. Opt. Soc. Am. B* **30**, 1551–1568 (2013).
11. C. Phillips, B. Mayer, L. Gallmann, *et al.*, "Design constraints of optical parametric chirped pulse amplification based on chirped quasi-phase-matching gratings," *Opt. Express* **22**, 9627–9658 (2014).
12. C. Heese, C. Phillips, L. Gallmann, *et al.*, "Ultrabroadband, highly flexible amplifier for ultrashort mid-infrared laser pulses based on aperiodically poled Mg:LiNbO₃," *Opt. Lett.* **35**, 2340–2342 (2010).
13. C. Heese, C. Phillips, B. Mayer, *et al.*, "75 mw few-cycle mid-infrared pulses from a collinear apodized APPLN-based OPCPA," *Opt. Express* **20**, 26888–26894 (2012).
14. C. Heese, C. Phillips, L. Gallmann, *et al.*, "Role of apodization in optical parametric amplifiers based on aperiodic quasi-phase-matching gratings," *Opt. Express* **20**, 18066–18071 (2012).
15. A. Dubietis, G. Jonušauskas, and A. Piskarskas, "Powerful femtosecond pulse generation by chirped and stretched pulse parametric amplification in BBO crystal," *Opt. Commun.* **88**, 437–440 (1992).
16. S. Witte and K. S. Eikema, "Ultrafast optical parametric chirped-pulse amplification," *IEEE J. Sel. Top. Quantum Electron.* **18**, 296–307 (2011).
17. J. Moses, H. Suchowski, and F. X. Kärtner, "Fully efficient adiabatic frequency conversion of broadband Ti:sapphire oscillator pulses," *Opt. Lett.* **37**, 1589–1591 (2012).
18. H. Suchowski, G. Porat, and A. Arie, "Adiabatic processes in frequency conversion," *Laser Photonics Rev.* **8**, 333–367 (2014).
19. P. Margules, J. Moses, H. Suchowski, *et al.*, "Ultrafast adiabatic frequency conversion," *J. Phys.: Photonics* **3**, 022011 (2021).
20. H. Suchowski, P. R. Krogen, S.-W. Huang, *et al.*, "Octave-spanning coherent mid-IR generation via adiabatic difference frequency conversion," *Opt. Express* **21**, 28892–28901 (2013).
21. C. Wang, C. Langrock, A. Marandi, *et al.*, "Ultrahigh-efficiency wavelength conversion in nanophotonic periodically poled lithium niobate waveguides," *Optica* **5**, 1438–1441 (2018).
22. M. Jankowski, N. Jornod, C. Langrock, *et al.*, "Quasi-static optical parametric amplification," *Optica* **9**, 273–279 (2022).
23. L. Ledezma, R. Sekine, Q. Guo, *et al.*, "Intense optical parametric amplification in dispersion-engineered nanophotonic lithium niobate waveguides," *Optica* **9**, 303–308 (2022).
24. M. Jankowski, C. Langrock, B. Desiatov, *et al.*, "Ultrabroadband nonlinear optics in nanophotonic periodically poled lithium niobate waveguides," *Optica* **7**, 40–46 (2020).
25. D. D. Hickstein, D. R. Carlson, H. Mundoor, *et al.*, "Self-organized nonlinear gratings for ultrafast nanophotonics," *Nat. Photonics* **13**, 494–499 (2019).
26. N. Singh, M. Raval, A. Ruocco, *et al.*, "Broadband 200-nm second-harmonic generation in silicon in the telecom band," *Light Sci. Appl.* **9**, 17 (2020).
27. A. Sukhorukov and A. Shchednova, "Parametric amplification of light in the field of a modulated laser wave," *J. Exp. Theor. Phys.* **60**, 1251–1263 (1971).
28. R. Danielius, A. Piskarskas, A. Stabinis, *et al.*, "Traveling-wave parametric generation of widely tunable, highly coherent femtosecond light pulses," *J. Opt. Soc. Am. B* **10**, 2222–2232 (1993).
29. S. Marchese, E. Innerhofer, R. Paschotta, *et al.*, "Room temperature femtosecond optical parametric generation in MgO-doped stoichiometric LiTaO₃," *Appl. Phys. B* **81**, 1049–1052 (2005).

30. C. Manzoni and G. Cerullo, "Design criteria for ultrafast optical parametric amplifiers," *J. Opt.* **18**, 103501 (2016).
31. A. B. U'Ren, C. Silberhorn, R. Erdmann, *et al.*, "Generation of pure-state single-photon wavepackets by conditional preparation based on spontaneous parametric downconversion," *arXiv*, arXiv:quant-ph/0611019 (2006).
32. V. Roman-Rodriguez, B. Brecht, K. Srinivasan, *et al.*, "Continuous variable multimode quantum states via symmetric group velocity matching," *New J. Phys.* **23**, 043012 (2021).
33. J. Mishra, T. P. McKenna, E. Ng, *et al.*, "Mid-infrared nonlinear optics in thin-film lithium niobate on sapphire," *Optica* **8**, 921–924 (2021).
34. J. Mishra, M. Jankowski, A. Y. Hwang, *et al.*, "Ultra-broadband mid-infrared generation in dispersion-engineered thin-film lithium niobate," *Opt. Express* **30**, 32752–32760 (2022).
35. R. Hamerly, A. Marandi, M. Jankowski, *et al.*, "Reduced models and design principles for half-harmonic generation in synchronously pumped optical parametric oscillators," *Phys. Rev. A* **94**, 063809 (2016).
36. M. Charbonneau-Lefort, B. Afeyan, and M. Fejer, "Theory and simulation of gain-guided noncollinear modes in chirped quasi-phase-matched optical parametric amplifiers," *J. Opt. Soc. Am. B* **27**, 824–841 (2010).
37. A. Gorbach, M. Roiz, M. Vainio, *et al.*, "Trapping of ultrashort pulses in nondegenerate parametric conversion," *Phys. Rev. A* **107**, 063515 (2023).
38. W. Wasilewski, A. I. Lvovsky, K. Banaszek, *et al.*, "Pulsed squeezed light: simultaneous squeezing of multiple modes," *Phys. Rev. A* **73**, 063819 (2006).
39. A. Lvovsky, W. Wasilewski, and K. Banaszek, "Decomposing a pulsed optical parametric amplifier into independent squeezers," *J. Mod. Opt.* **54**, 721–733 (2007).
40. A. Christ, B. Brecht, W. Mauerer, *et al.*, "Theory of quantum frequency conversion and type-ii parametric down-conversion in the high-gain regime," *New J. Phys.* **15**, 053038 (2013).
41. M. Vasilyev, M. Annamalai, N. Stelmakh, *et al.*, "Quantum properties of a spatially-broadband traveling-wave phase-sensitive optical parametric amplifier," *J. Mod. Opt.* **57**, 1908–1915 (2010).
42. M. Annamalai, N. Stelmakh, M. Vasilyev, *et al.*, "Spatial modes of phase-sensitive parametric image amplifiers with circular and elliptical gaussian pumps," *Opt. Express* **19**, 26710–26724 (2011).
43. D. A. Miller, "All linear optical devices are mode converters," *Opt. Express* **20**, 23985–23993 (2012).
44. G. Triginer, M. D. Vidrighin, N. Quesada, *et al.*, "Understanding high-gain twin-beam sources using cascaded stimulated emission," *Phys. Rev. X* **10**, 031063 (2020).

3.3 Picojoule-level supercontinuum generation in thin-film lithium niobate on sapphire

In the previous chapter, we discussed the development of a broadband mode-locked laser operating at a high repetition rate of 1 GHz (Section 2.1). To turn this source into a low-noise OFC, subsequent self-referencing and stabilization were required. In our case, the remarkably high average power available and short pulse durations enabled the generation of the supercontinuum required for self-referencing using a commercially-available photonic crystal fiber (PCF), which typically consumes about ten kilowatts of peak power for this task. However, most commercially available laser oscillators operating at high repetition rates do not achieve sufficient power levels, thus requiring an amplification stage prior to SCG. Besides increasing the price and footprint of the overall system, the post amplification stage adds another layer of complexity and may introduce additional noise. The challenge of generating supercontinuum increases at higher repetition rates since higher average power or shorter pulses are required to reach similar peak power levels. For instance, at 10-GHz repetition rate, the average power and pulse duration delivered by the laser described in section 2.1 would no longer be sufficient for driving SCG inside conventional PCFs. Besides the fact that further power scaling is technologically challenging, the damage threshold of the fiber ultimately limits the input average power. In this context, developing nonlinear devices that allow SCG and f_{CEO} detection at much lower power and energy requirements is of high interest. Building upon the recent progress of TFLN-on-sapphire, we present an approach to picojoule-level SCG and on-chip f_{CEO} detection.

3.3.1 Article outline

Context

During the past decades, the development of integrated devices enabled reduction of the power required to drive SCG from hundreds or even thousands of picojoules inside traditional PCFs [44], to few picojoules using nanophotonic waveguides. Driven by the need of realizing compact and low-noise sources, numerous approaches to SCG have been focusing on simplifying the detection of f-to-2f beatnotes. For instance, when SCG is driven simultaneously with harmonic generation, the spectral contents containing the f_{CEO} can be generated directly inside the waveguide, thus replacing bulky multi-stage f-to-2f interferometers by a single compact device. Previously reported in conventional waveguides [45–47], this method has been successfully applied with nanopho-

3.3. Picojoule-level supercontinuum generation in thin-film lithium niobate on sapphire

tonic devices [48–50]. Among the existing platforms, TFLN, which features a large $\chi^{(2)}$ and supports periodic poling for efficient second harmonic generation (SHG), is becoming a standard solution for on-chip f-to-2f detection [50–53]. However, most TFLN-based experiments have relied on silica substrates, which exhibit high absorption losses beyond 2.5 μm and thus restrict the effective transparency window of the overall waveguides. Despite the potential of TFLN-on-sapphire for the generation of MIR light [34–36], this new-developed platform has not yet been applied to SCG. In this work, we demonstrate broadband SCG using TFLN on sapphire waveguides, and subsequently show the suitability of this platform for on-chip f_{CEO} detection.

Results

Our approach relies on group-velocity-matched second-harmonic generation, which uses an interplay between saturation and a small phase-mismatch to generate a spectrally broadened fundamental and second harmonic [54]. This technique is particularly suited for f-to-2f detection since the f_{CEO} beatnotes generated by the overlapping fundamental and second harmonic spectra remain in phase across very large frequency ranges. A critical requirement of this technique is that the effects of first- and second-order dispersion are negligible. To meet this condition, we dispersion engineer the periodically-poled TFLN waveguides through their cross-sectional geometry to minimize both the group velocity mismatch and group velocity dispersion (GVD) for a fundamental pulse centered around 2050 nm and its second harmonic.

When driven with 50-fs pulses, SHG starts saturating and broadening with pulse energies as small as few picojoules. As we increase the on-chip pulse energy to tens of picojoules, a cascade of $\chi^{(2)}$ -based mixing processes occurring simultaneously with SHG gives rise to several harmonics up to the fifth order. The five harmonics experience a strong spectral broadening and merge together around 20 pJ. The generated supercontinuum extends from the ultraviolet to the MIR spectral range, spanning between 360-2660 nm at a maximum input pulse energy of 45 pJ. We subsequently use the overlap between the first and second harmonic to detect the f-to-2f beatnotes directly at the waveguide output, with a signal-to-noise ratio of 13 dB, mainly limited by the detection setup. For comparison, f_{CEO} detection by quasi-static SHG has already yielded up to 35 dB [52]. The limitations and outlooks are discussed in the article.

Conclusion

This work establishes TFLN-on-sapphire as a viable platform for the generation of broadband and coherent light from the ultraviolet to the MIR. The devices achieved the f-to-2f detection of a 2- μm source with few tens of picojoules, which

is promising for self-referencing multi-GHz repetition rates MIR lasers such as the ones based on Thulium-doped materials.

3.3.2 Further discussion

Group velocity mismatch of the fabricated waveguides

The approach to SCG presented in this work relies on group-velocity-matched second-harmonic generation, which uses an interplay between saturation and a small phase-mismatch to generate a spectrally broadened fundamental and second harmonic. A detailed investigation of the nonlinear dynamics and properties of this technique can be found in [54]. To achieve group velocity matching between fundamental and second harmonic pulses centered around 2090 nm and 1045 nm, respectively, we dispersion engineer the TFLN waveguides via their cross-sectional geometry. Since fabrication errors are present in any real devices, it is important to verify the waveguide geometry of the fabricated waveguides and their dispersion properties. Accurate measurements of the dispersion coefficients can be achieved by driving CW second harmonic generation at different fundamental wavelengths, thus requiring a wavelength-tunable CW laser emitting around 2.1 μm . Unfortunately, such source was not available at the time of the submission. Another solution, however less precise, is to estimate the amount of GVM via the fundamental and second harmonic spectra generated in the unsaturated regime. When the group velocity dispersion of the fundamental is negligible, the second harmonic spectrum is determined by the fundamental envelope filtered, in the frequency domain, by the CW transfer function for second harmonic generation [55],

$$|A_{2\omega}(2\omega_0 + 2\Omega)|^2 = \kappa L^2 \text{sinc}(\Delta k(\Omega)L/2)^2 |A_{2\omega}^{\text{ND}}(2\omega_0 + 2\Omega)|^2 \quad (3.6)$$

where $A_{2\omega}(2\omega_0 + 2\Omega)$ is the second harmonic spectrum, $\omega_0 + \Omega$ the fundamental frequency detuned by Ω around the peak of the pump, $\Delta k(\omega_0 + \Omega)L/2$ the phase mismatch, L the waveguide length and κ the nonlinear coupling. $A_{2\omega}^{\text{ND}}(2\omega_0 + 2\Omega)$ represents the second harmonic envelope that would be obtained in absence of dispersion. It is determined by the convolution of the frequency-domain fundamental envelope with itself.

Equation 3.6 shows that the spectral bandwidth of the second harmonic is limited by the phase-mismatch Δk inside the sinc function. At the leading order in Ω , this phase-mismatch is given by

$$\Delta k(\Omega) = \Delta k_0 + 2\Delta k'\Omega \quad (3.7)$$

where Δk_0 is the phase mismatch at the peak of the pump. In our case, Δk_0 is canceled by the periodic poling. Introducing Eq. 3.7 in 3.6 shows that the first

3.3. Picojoule-level supercontinuum generation in thin-film lithium niobate on sapphire

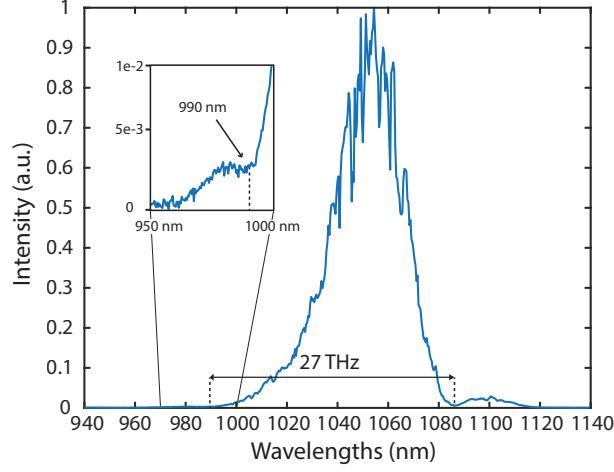


Figure 3.1: Spectrum of the second harmonic generated in the unsaturated regime. The inset shows a zoom of the spectrum between 950 -1000 nm. We use the distance between the first zeros of the spectrum to estimate the GVM.

zeros of the second harmonic spectrum are separated by

$$\Delta\Omega = 2\pi/(\Delta k' L) \quad (3.8)$$

This result is valid as long as the second- and higher-order dispersion coefficients are negligible compared to the GVM, which we can assume in this work.

We now use Eq. 3.8 to estimate the GVM of the fabricated TFLN waveguides. Figure 3.1 shows the second harmonic spectrum obtained in the unsaturated regime. To confirm the unsaturated regime, we verify that the shape of the generated spectrum does not change with the input power, which indicates a reasonably low amount of pump depletion. We note here that the location of the left-hand side zero is not clear. We estimate its position at the turning of the shoulder around 990 nm (see inset fig 3.1). In the worst case, this choice leads to a small overestimation of the GVM. Under these considerations, the zeros are separated by 27 THz, giving a GVM around 7.5 fs/mm, which is reasonably close to the design (<10 fs/mm).

Estimation of the coupled power

The power requirement is often used as a figure of merit in nonlinear optics. In nanophotonics the input power can either refer to the incident power (before coupling) or the power coupled inside the waveguide, namely on-chip power, or in-coupled power. While the incident power provides information about the efficiency of the overall system including the maturity of the platform, the on-chip power characterizes the nonlinear performances of the device. In our study,

we focus on the performances of the TFLN devices, and thus report on the on-chip (in-coupled) fundamental power.

Estimating the power coupled inside the waveguide with reasonable accuracy is challenging and requires careful attention, particularly at such low pulse energy. To determine the coupling efficiency, we couple a small amount of light inside the waveguides; sufficient for reliable output power measurements, and small enough so that nonlinear conversions can be neglected. In this case, provided negligible losses, the power at the output facet of the waveguide corresponds, after correction of the Fresnel coefficient, to the pump power coupled inside the waveguide.

To estimate the power at the output facet, the output beam is first collected with a reflective inverse-Cassegrain objective and subsequently focused onto a low-noise photodetector. An iris is placed in front of the detector to avoid potential scattered light from reaching the sensor. A lock-in detection is applied to facilitate the measurement of the output power.

To estimate the power at the waveguide facet, one needs to determine the collection efficiency of the output Cassegrain objective. This task is often challenging. For instance, one can place a photodetector with a large surface area directly in front of the output facet of the waveguide, close enough to collect all the strongly diverging output photons. The transmission coefficient is then determined by the ratio between the power at the waveguide output and the power after the objective. However, this method requires background-free measurements to avoid the uncoupled light that inevitably reaches the detector from affecting the detection. In this work, we used the transmission values reported in [35] where a background-free measurement of the Cassegrain objective collection efficiency was obtained driving OPA inside TFLN waveguides. We note here that the transmission of the Cassegrain objective is the value introducing the largest uncertainties, estimated to be around 10-15%.

Having determined the on-chip power at the output facet, we can estimate the overall coupling efficiency. Provided negligible nonlinear conversion efficiencies and negligible losses, the ratio between the on-chip output power and the power before the input objective gives the overall coupling efficiency, which we measure to be around 1.5%. This value is used in the rest of the experiments to estimate the fundamental power or energy that is coupled inside the chip. The uncertainties on the coupling efficiency, mainly due to the transmission of the output Cassegrain, are estimated around 15%, which is reasonable in the scope of this work.

We close this section with the following comments. (i) The poor 1.5% efficiency is explained by the transmission of the input objective (15%) and the mismatch between the shape of the input beam at the focus and the waveguide

mode (10% overlap). Alternative methods such as lensed fiber coupling should allow coupling efficiencies in excess of 30%. (ii) Since the coupling efficiency is estimated at low input power, the thermal effects are negligible. In contrast, when the waveguides are driven at high input power, the thermal load at the waveguide surface leads to noticeable changes in the waveguide cross-sectional geometry which may affect the coupling efficiency.

(iii) Significant improvement of the coupling efficiency is expected with the development of edge couplers compatible with the TFLN platform [56].

3.3.3 Acknowledgment

The experiments have been conducted in the laboratories of Martin Fejer and Amir Safavi Naeini, in close collaboration with Alex Hwang for the fabrication of the waveguides and Marc Jankowski. I particularly thank Marc Jankowski for his inspiring works and insightful discussions.



Picojoule-level supercontinuum generation in thin-film lithium niobate on sapphire

MARIN HAMROUNI,^{1,2,*}  MARC JANKOWSKI,^{2,3}  ALEXANDER Y. HWANG,²  NOAH FLEMENS,²  JATADHARI MISHRA,²  CARSTEN LANGROCK,²  AMIR H. SAFAVI-NAEINI,²  MARTIN M. FEJER,² AND THOMAS SÜDMEYER¹ 

¹Laboratoire Temps-Fréquence, Université de Neuchâtel, Avenue de Bellevaux 51, Neuchâtel, Switzerland

²E. L. Ginzton Laboratory, Stanford University, Stanford, California 94305, USA

³NTT Research, Inc. Physics & Informatics Laboratories, 940 Stewart Drive, Sunnyvale, California 94085, USA

*marin.hamrouni@unine.ch

Abstract: We demonstrate ultraviolet-to-mid-infrared supercontinuum generation (SCG) inside thin-film lithium niobate (TFLN) on sapphire nanowaveguides. This platform combines wavelength-scale confinement and quasi-phase-matched nonlinear interactions with a broad transparency window extending from 350 to 4500 nm. Our approach relies on group-velocity-matched second-harmonic generation, which uses an interplay between saturation and a small phase-mismatch to generate a spectrally broadened fundamental and second harmonic using only a few picojoules of in-coupled fundamental pulse energies. As the on-chip pulse energy is increased to tens of picojoules, these nanowaveguides generate harmonics up to the fifth order by a cascade of sum-frequency mixing processes. For in-coupled pulse energies in excess of 25 picojoules, these harmonics merge together to form a supercontinuum spanning 360–2660 nm. We use the overlap between the first two harmonic spectra to detect f - $2f$ beatnotes of the driving laser directly at the waveguide output, which verifies the coherence of the generated harmonics. These results establish TFLN-on-sapphire as a viable platform for generating ultra-broadband coherent light spanning from the ultraviolet to mid-infrared spectral regions.

© 2024 Optica Publishing Group under the terms of the [Optica Open Access Publishing Agreement](#)

1. Introduction

In recent years, the generation of coherent supercontinuum from ultrafast mode-locked lasers has been attracting considerable attention due to its large variety of applications. In many cases, the generated supercontinuum is used for the self-referencing and stabilization of optical frequency combs (OFCs), where octave-spanning spectra are required to detect the carrier-envelope offset frequency (f_{CEO}) via f - $2f$ interferometry [1–3]. Once stabilized, the resulting low-noise OFCs constitute a crucial tool in spectroscopy, for which a broad spectral bandwidth extending into the mid-infrared is desirable [4–6].

For most applications, increasing the generated spectral bandwidth while decreasing the input power requirement at the same time is of high interest. In this context, the recent progress of nanophotonic technologies has played a major role [7,8]. These platforms have led to the development of highly efficient nonlinear devices reducing the power required for supercontinuum generation (SCG) from hundreds of picojoules inside traditional photonic crystal fibers [9], to few picojoules using nanophotonic waveguides [10,11], and recently hundreds of femtojoule in resonant devices [12]. Besides radically reducing power requirements, the emergence of this new class of nanophotonic devices adds further prospects in the development of fully integrated spectroscopic measurement devices.

Initially, nearly all demonstrations of SCG in integrated devices were relying on third-order nonlinearities, driven inside materials such as silicon nitride [13,14], silicon [15–17], and more recent ones such as germanium-based platforms [18–20]. While $\chi^{(3)}$ -based SCG enables broad bandwidth spanning across several spectral regions, these devices typically operate with hundreds of picojoules and often require a separate second-harmonic generation (SHG) stage when used for f-2f self-referencing. In practice, this SHG stage is challenging to achieve at the typically low generated power levels and represents an added source of experimental complexity.

An alternative approach consists in driving SCG in platforms that exhibit both a $\chi^{(2)}$ and $\chi^{(3)}$ nonlinear response. In these devices, the combination of efficient harmonic generation and spectral broadening leads to the formation of supercontinua composed of multiple overlapping combs. This regime offers the possibility to detect the f_{CEO} beatnotes directly at the waveguide output, which simplifies f-2f detection by eliminating the discrete SHG stage. Previously reported in weakly confining waveguides [21–23], this technique was recently achieved in integrated devices [24–26]. There, the thin-film lithium niobate (TFLN) platform emerged as one of the leading solutions [10,26–28]. However, nearly all works based on TFLN utilize a silica bottom-cladding, which results in high absorption loss beyond 2500 nm and hinders further spectral extension into the mid-infrared region. In contrast, sapphire substrate features high transparency up to 4.5 μm , and thus stands out as a promising alternative to silica for realizing compact and efficient MIR sources [29–31].

In this work, we demonstrate for the first time ultraviolet-to-mid-infrared SCG using TFLN-on-sapphire waveguides, and subsequently show the suitability of this platform for on-chip f_{CEO} detection. We periodically pole TFLN waveguides to achieve quasi-phase-matched SHG at a fundamental wavelength of 2100 nm, and use geometric dispersion engineering to eliminate leading-order dispersive effects for efficient and broadband nonlinear conversion. We note here that this approach is inspired from previous demonstrations that have used quasi-static nonlinear interactions to achieve efficient SCG [10,11,27]. We further discuss the dispersion engineering design of the waveguides in the next section. As a result, driving the TFLN waveguides with only few picojoules of on-chip pump-pulse energy, we observe saturated SHG that manifests by the onset of spectral broadening for both harmonics. The spectrum of the two combs further broaden as we increase the driving power and merge around 22 pJ of on-chip pulse energy. Using the overlap between these two combs, we detect f_{CEO} beatnotes directly at the output of the waveguide, showing the spectral broadening mechanism maintains a high degree of coherence across large spectral bandwidths. Furthermore, the high nonlinearities featured by the nanophotonic waveguides enable the generation of multiple higher-order harmonics occurring simultaneously with SHG. Remarkably, with only 10 pJ of input pulse energy, we detect harmonics up to the fifth order. These harmonics exhibit strong spectral broadening with increased pump-pulse energies and finally merge at the -45-dB level for in-coupled pulse energies between 20-25 pJ. To the best of our knowledge, this is the first time that such a high number of harmonics is reported in integrated devices. When pumped at a maximum pulse energy of 45 pJ, these devices achieve a broad supercontinuum extending from 360 nm to 2660 nm. These results have multiple prospective impacts. Besides demonstrating the suitability of the TFLN-on-sapphire platform for self-referencing MIR sources such as Tm-based laser oscillators, this work will open new opportunities to further investigate the underlying physics of broadband high harmonic generation inside nonlinear nanophotonic devices.

2. Design of the waveguides

We first discuss the design criteria of the TFLN waveguides. Recently, a novel approach for efficient and broadband SCG based on saturated second-order nonlinear interactions was presented [27,32]. This work showed that driving phase-matched SHG in nanophotonic waveguides in a regime where leading-order dispersive effects are negligible enables SCG at an unprecedented low pulse

energy. Furthermore, they demonstrate that SCG by saturated quasi-static SHG is advantageous for f - $2f$ detection, since the f_{CEO} beatnotes generated by the overlapping spectra remain in phase across very large spectral ranges. This technique requires the first- and second-order dispersion effects to be negligible. In this perspective, we dispersion engineer the TFLN waveguides through their cross-sectional geometry to minimize both the group velocity mismatch (GVM) and group velocity dispersion (GVD) for a fundamental pulse centered around 2050 nm and its second harmonic. The devices consist of 5-mm long TFLN ridge waveguides with a top width of 1520 nm, a film thickness of 931 nm and an etch depth of 608 nm (Fig. 1(a)). The nominal poling period for quasi-phase-matching (QPM) is 6.30 μm . Figure 1(b) shows the GVM and GVDs as a function of the wavelengths for the waveguide geometry considered here. We observe a zero-crossing of the GVM around 2000 nm and 2250 nm, with the magnitude remaining below 15 fs/mm over more than 360 nm of fundamental bandwidth, between 1910-2275 nm. At the nominal fundamental wavelength of 2050 nm, this waveguide geometry leads to a low simulated GVM of 6 fs/mm, a fundamental GVD of 20 fs^2/mm , and second harmonic GVD of $<5 \text{ fs}^2/\text{mm}$. We note here the presence of discontinuities in the dispersion curves around a fundamental and corresponding second harmonic wavelength of 2500 nm and 1250 nm, respectively. This effect is due to an avoided crossing between second harmonic modes at 1250 nm. The periodic poling and subsequent fabrication procedures are similar to the one described in [29]. We fabricate a total of 27 pairs of waveguides with a 10-nm poling period step between each adjacent pair. This way, we cover a total poling period range of $6.30 \pm 0.135 \mu\text{m}$ to compensate for potential fabrication errors. We use temperature for fine tuning of the phase-matching. Each poling region accommodates two adjacent waveguides with similar dimensions, separated by an 8- μm gap that is wide enough to avoid cross talk. While the fabrication yield of the waveguide is close to 100%, we observe significant differences in the quality of the facets, which affects the maximum achievable coupling efficiency. The waveguide used throughout the article achieves 1.5% of coupling efficiency.

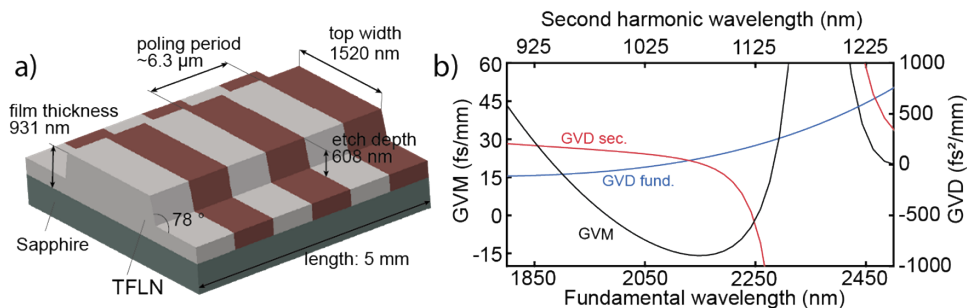


Fig. 1. (a) Schematic of the waveguide design. (b) Simulated GVM (black, left y-axis) and GVD of the fundamental (blue, right axis) and second harmonic (red, right axis) as a function of the fundamental (bottom axis) and second harmonic (top axis) wavelengths. The presence of an avoided crossing between second harmonic modes at 1250 nm causes discontinuities in the GVM (black) and second harmonic GVD (red).

3. Experimental setup

The experimental setup is shown in Fig. 2. The fundamental driving pulses are delivered by a synchronously pumped degenerate optical parametric oscillator (OPO), similar to that described in [33]. The spectrum of the driving pulses displays a full-width at half-maximum spectral bandwidth of 130 nm centered around 2090 nm. Assuming transform limited pulses, we estimate the pulse duration from the spectrum to be around 40 fs. We note here that while these waveguides

were originally designed to be pumped by a 2050-nm Tm:KYW mode-locked laser, we ultimately used a 2090-nm OPO. This wavelength offset is well covered by the range of available poling periods, and only has minor effects on the SCG dynamics by having a slightly larger GVM than originally designed. The OPO delivers a p-polarized beam with a fixed output power of 300 mW at 100 MHz repetition rate. Reflective filters are used to control the power at the input of the waveguides. The input beam is coupled into the waveguides using a reflective inverse-Cassegrain objective (Thorlabs LMM-40X-P01). While the obscuration of the reflective objective greatly limits the transmission of a Gaussian beam, it offers the advantage of avoiding achromatic and temporal dispersion. The objective transmission ($\sim 15\%$) and the mismatch between the input beam at the focus and the waveguide mode ($\sim 10\%$ overlap) result in an overall coupling efficiency of $\sim 1.5\%$, which limits the maximum on-chip input pulse energy to 45 pJ. A similar objective is used to collect the beam at the waveguides output. In this case, the collection efficiency is only limited by the Cassegrain transmission, and was previously estimated to be around 35% in the 2.0- μm region [30]. For the rest of the paper, the input and output pulse energies are reported directly inside the waveguide. The waveguide chip is mounted on an aluminum holder that is temperature stabilized. The aluminum holder is placed on an XY-axis translation stage controlled by piezo actuators. The longitudinal position of the focus at the input facet of the chip is adjusted by moving the reflective objective along the optical axis of the input beam. During the waveguide alignment procedure, the output modes of the fundamental and second harmonic were imaged on a camera to confirm the excitation of the TE_{00} mode. To characterize the generated spectrum, we use two different optical spectrum analyzers sensitive between 350-1750 nm (Yokogawa AQ6374) and 1500-3400 nm (Yokogawa AQ6376E), respectively. We verify that the fibers used to couple the light into the spectrum analyzers are transparent over the entire spectral ranges.

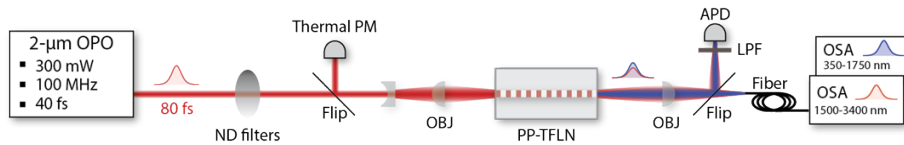


Fig. 2. Experimental setup.; ND filters, variable neutral density filter; Obj., reflective objective; PP-TFLN., Periodically-poled thin-film lithium niobate waveguide; Flip, flip mirror; LPF, long-pass filter; APD, avalanche photodetector; OSA, fiber-coupled optical spectrum analyzers.

In the last section, we discuss the carrier-envelope-offset frequency detection. To detect the f_{CEO} beatnotes, the output of the waveguide is directly focused using the reflective objective onto an avalanche photoreceiver (APD310), which features a sensitivity range between 850-1650 nm. A long pass filter with a cut-off wavelength of 1350 nm is used to limit the detected wavelength range to the overlap region between the first two harmonics, which suppresses saturation due to shorter wavelengths that do not contribute to the f_{CEO} beatnote.

4. Supercontinuum generation

Figure 3 shows the power spectral density as a function of the input pulse energy. Below 1 pJ, the waveguides are driven in the unsaturated regime, and we observe the formation of a broadband second harmonic centered around 1045 nm. In this unsaturated regime, we measure a distance between the zeros of the second harmonic spectrum of 27 THz, which gives a GVM of nearly 7.5 fs/mm, assuming negligible higher-order dispersion coefficients [34]. Above 3 pJ, we observe the formation of fringes and side lobes centered around the peak of the pump and signal spectra (Fig. 3, spectrum 5 pJ). These features become asymmetric and more finely patterned as we increase the pulse energy. For pump pulse energies in excess of ~ 12 pJ, the fundamental spectrum

experiences strong broadening towards shorter wavelengths, accompanied with the formation of larger side-lobes (Fig. 3, spectrum 15 pJ). This behavior is characteristic of spectral broadening driven by saturated SHG in presence of negligible group velocity mismatch and group velocity dispersion [32], which is consistent with the waveguides design. The fundamental and second harmonic spectra continue broadening as we increase the pump power, and overlap above the spectrometer noise floor at -55 dB for pulse energies in excess of 22 pJ. At higher input pulse energies, the second harmonic spectrum is notably flat over a large bandwidth and displays a distinctive oscillatory pattern, which is again consistent with spectral broadening based on saturated quasi-static SHG. We note here that while the spectral broadening of the first two harmonics exhibits reasonable agreement with what we expect from our heuristic model [32], we observe an overall factor of two between experiment and theory for the on-chip pulse energy required to achieve SCG. We attribute this discrepancy to a combination between finite poling depth and a deviation of the mean duty cycle from 50%. In these latter cases the effective nonlinear coupling is reduced due to a weaker overlap between the interacting modes, which increases the pulse energy needed to achieve supercontinuum generation by a constant factor.

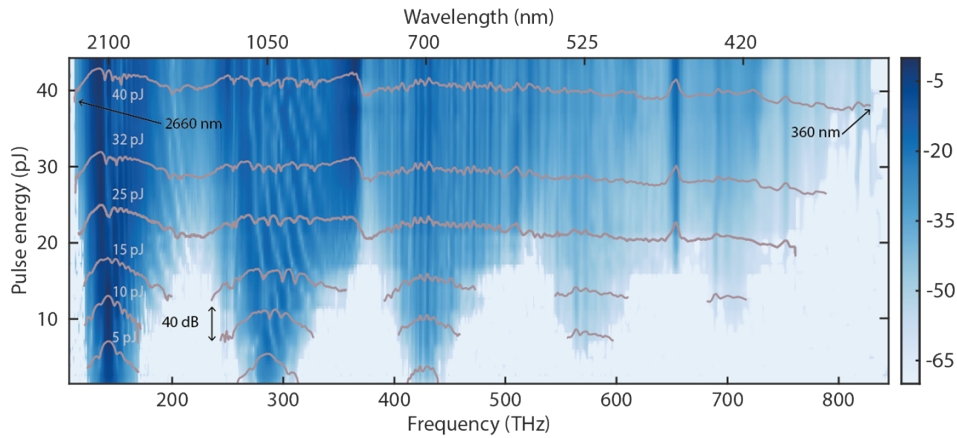


Fig. 3. Generated power spectral density as a function of the on-chip pulse energy. A selection of power spectral densities is plotted in one dimension on top of the graphic to highlight the main features described in the text. The color scale is in dB.

In addition to the fundamental and second harmonic, we observe the onset of the third, fourth and fifth harmonics with pulse energies as low as 2, 7, and 12 pJ, respectively. These three higher-order harmonics experience a strong spectral broadening and merge with the fundamental and first harmonics between 20-25 pJ of input pulse energy. For pulse energies in excess of 25 pJ, the supercontinuum composed of the five first harmonics continue broadening at a reduced rate. When the pump-pulse energy reaches a maximum of 45 pJ, the generated supercontinuum spans nearly three octaves above the spectrometer noise floor, extending from 360 nm to 2660 nm within a -55-dB dynamic range. It is worth noting that the third and higher harmonics do not feature the oscillatory pattern observed on the first two harmonic spectra, which is expected since the frequency mixings responsible for the presence of higher order harmonics do not achieve quasi-static interactions. A detailed investigation of the physics underlying the nonlinear dynamics is beyond the scope of this paper; it requires consideration of all the possible nonlinear paths, as well as a large set of parameters such as higher-order QPM grating coefficients, the phase-matching of higher-order waveguide modes, or linear coupling between waveguide modes [35]. A theoretical analysis of broadband nonlinear interactions such as SCG and harmonic generation in TFLN

waveguides has recently been discussed in [36], using the experimental configuration described here as a case study.

We close this section by commenting on the limit of the generated supercontinuum. While we expect the fundamental harmonic spectrum to broaden symmetrically around the carrier frequency, we observe much greater broadening on its blue tail. As a consequence, the extension of the supercontinuum is restricted on the long-wavelength side below 2700 nm. The effective refractive indices of the fundamental TE and TM modes indicate the presence of a crossing between those two modes. Preliminary investigations show that this crossing may result in a coupling from TE to TM mode that would ultimately restrict the spectral broadening below 2700 nm. We note here that this TE-TM mode crossing is different from the avoided crossing between second harmonic modes previously mentioned (Fig. 1(b)). Another possible reason is the presence of strong variations of the nonlinearity dispersion at large wavelengths. Further investigations will be carried out to confirm these assumptions. Finally, the short-wavelength tail of the supercontinuum nearly reaches the lower bound of the TFLN transparency window.

5. Carrier-envelope offset frequency detection

We use the generated supercontinuum to measure the f_{CEO} of the driving source. As described in section 3, the fundamental and second harmonic spectra overlap for input pulse energy in excess of 22 pJ. Provided coherent harmonic generation and spectral broadening, the overlapping combs give rise to f-2f beatnotes. Thus, when the overlap between the two combs becomes sufficient, the generated beatnotes can be detected directly at the output of the waveguide. In this experiment, we detect the beatnotes between the fundamental and second harmonic by focusing the waveguide output onto an InGaAs avalanche photodetector (experimental setup Fig. 2). Since we only want to measure the spectral contents contained within the fundamental and second harmonic, we suppress the rest of the supercontinuum using a long-pass filter with a cutoff wavelength of 1350 nm. The InGaAs sensor of the avalanche photodetector filters out wavelengths above 1800 nm. It is worth noting that conventional approaches often require much narrower spectral filtering of few tens of nanometers to obtain sufficiently large f_{CEO} beatnotes with respect to the f_{rep} peak [21].

Figure 4 shows the radio-frequency spectrum corresponding to the f-2f beatnotes obtained driving the waveguides with 45 pJ. We observe the presence of four peaks. The highest peak (peak 3) located at 100 MHz corresponds to the repetition frequency of the driving source.

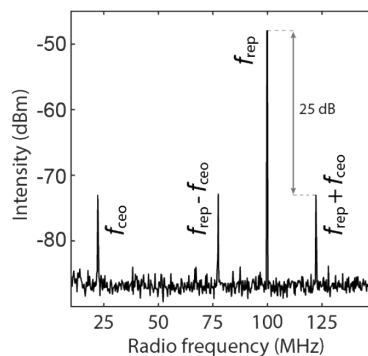


Fig. 4. Radio-frequency spectrum measured with 10-kHz resolution bandwidth and acquired using 45 pJ of input pulse energy. From left to right, the frequency of the peaks corresponds to f_{CEO} , $f_{\text{rep}} - f_{\text{CEO}}$, f_{rep} and $f_{\text{rep}} + f_{\text{CEO}}$, where f_{rep} and f_{CEO} are the repetition rate and carrier-envelope offset frequencies, respectively.

The three remaining peaks are f-2f beatnotes. From left to right, these three peaks feature a frequency of 22 MHz, 78 MHz and 122 MHz, which correspond to f_{CEO} , $f_{\text{rep}} - f_{\text{CEO}}$ and $f_{\text{rep}} + f_{\text{CEO}}$, respectively. Remarkably, the intensity of the f-2f beatnotes is only 25 dB below the repetition frequency, which indicates they remain coherent and in-phase across a large overlapping region. This result aligns well with the properties of supercontinuum generation driven by saturated quasi-static SHG [32]. In the current configuration, the f_{CEO} beatnotes features a signal-to-noise ratio (SNR) of 13 dB in a 10-kHz resolution bandwidth, limited by the noise floor of the avalanche detector. While 13 dB of SNR remains too low for subsequent f_{CEO} stabilization, the fact they are only 25 dB below the f_{rep} peak, which also presents a relatively low SNR, indicates further improvement of the detection setup should allow a substantial increase of the beatnotes SNR.

6. Conclusion

In this paper, we have demonstrated SCG inside TFLN-on-sapphire nanophotonic waveguides. When driven with picojoules of pulse energies, these devices achieve broadband and efficient SHG. At higher input power, a cascade of mixing processes occurs in the waveguide, giving rise to the generation of higher harmonics which merge together and form a broad supercontinuum spanning from ultraviolet to MIR frequency range. This is the first time TFLN-on-sapphire waveguides are used for SCG, and the performances are comparable to state-of-the-art results achieved in conventional TFLN-on-silica devices. Therefore, this work establishes this MIR-compatible platform as a promising solution for efficient and broadband nonlinear interactions with picojoule-level pulse energies. Furthermore, using the broad and coherent overlap between the fundamental and second harmonic combs, we could detect f_{CEO} beatnotes of the driving source directly at the waveguide output. Thus, we believe this work will open new solutions for self-referencing high repetition rate MIR ultrafast lasers such as Tm-based oscillators, which is of topical interest for applications in research and industry.

Funding. Schweizerischer Nationalfonds zur Förderung der Wissenschaftlichen Forschung (200021_188456); Defense Advanced Research Projects Agency (D19AP00040).

Acknowledgments. The authors wish to thank NTT Research for their financial and technical support. Fabrication was performed at the Stanford Nanofabrication Facility, the Stanford Nano Shared Facilities (NSF award ECCS-2026822), and the Cell Sciences Imaging Facility (NCRR award S10RR02557401). A.Y.H. acknowledges NSF GRFP, Grant. No. 2146755.

Disclosures. The authors declare no conflicts of interest.

Data availability. Data underlying the results presented in Fig. 1(b), Fig. 3 and Fig. 4 are available in [37].

References

1. H. R. Telle, G. Steinmeyer, A. E. Dunlop, *et al.*, "Carrier-envelope offset phase control: A novel concept for absolute optical frequency measurement and ultrashort pulse generation," *Appl. Phys. B* **69**(4), 327–332 (1999).
2. S. A. Diddams, D. J. Jones, J. Ye, *et al.*, "Direct link between microwave and optical frequencies with a 300 THz femtosecond laser comb," *Phys. Rev. Lett.* **84**(22), 5102–5105 (2000).
3. T. Udem, R. Holzwarth, and T. W. Hänsch, "Optical frequency metrology," *Nature* **416**(6877), 233–237 (2002).
4. S. A. Diddams, "The evolving optical frequency comb [Invited]," *J. Opt. Soc. Am. B* **27**(11), B51–B62 (2010).
5. N. Picqué and T. W. Hänsch, "Frequency comb spectroscopy," *Nat. Photonics* **13**(3), 146–157 (2019).
6. I. Zorin, P. Gattinger, A. Ebner, *et al.*, "Advances in mid-infrared spectroscopy enabled by supercontinuum laser sources," *Opt. Express* **30**(4), 5222–5254 (2022).
7. C.-S. Brès, A. D. Torre, D. Grassani, *et al.*, "Supercontinuum in integrated photonics: generation, applications, challenges, and perspectives," *Nanophotonics* **12**(7), 1199–1244 (2023).
8. Y. Fang, C. Bao, S.-A. Li, *et al.*, "Recent Progress of Supercontinuum Generation in Nanophotonic Waveguides," *Laser Photonics Rev.* **17**(1), 2200205 (2023).
9. J. M. Dudley, G. Genty, and S. Coen, "Supercontinuum generation in photonic crystal fiber," *Rev. Mod. Phys.* **78**(4), 1135–1184 (2006).
10. M. Jankowski, N. Jornod, C. Langrock, *et al.*, "Quasi-static optical parametric amplification," *Optica* **9**(3), 273 (2022).
11. L. Ledezma, R. Sekine, Q. Guo, *et al.*, "Intense optical parametric amplification in dispersion-engineered nanophotonic lithium niobate waveguides," *Optica* **9**(3), 303–308 (2022).

12. R. Sekine, R. Gray, L. Ledezma, *et al.*, “Two-Octave Frequency Comb from a Nanophotonic Parametric Oscillator,” in *CLEO* (Optica Publishing Group, 2023), paper SW4 G.2.
13. R. Halir, Y. Okawachi, J. S. Levy, *et al.*, “Ultrabroadband supercontinuum generation in a CMOS-compatible platform,” *Opt. Lett.* **37**(10), 1685–1687 (2012).
14. D. Grassani, E. Tagkoudi, H. Guo, *et al.*, “Mid infrared gas spectroscopy using efficient fiber laser driven photonic chip-based supercontinuum,” *Nat. Commun.* **10**(1), 1553 (2019).
15. B. Kuyken, X. Liu, R. M. Osgood, *et al.*, “Mid-infrared to telecom-band supercontinuum generation in highly nonlinear silicon-on-insulator wire waveguides,” *Opt. Express* **19**(21), 20172–20181 (2011).
16. N. Singh, D. D. Hudson, Y. Yu, *et al.*, “Midinfrared supercontinuum generation from 2 to 6 μm in a silicon nanowire,” *Optica* **2**(9), 797–802 (2015).
17. N. Nader, D. L. Maser, F. C. Cruz, *et al.*, “Versatile silicon-waveguide supercontinuum for coherent mid-infrared spectroscopy,” *APL Photonics* **3**(3), 036102 (2018).
18. M. A. Ettabib, L. Xu, A. Bogris, *et al.*, “Broadband telecom to mid-infrared supercontinuum generation in a dispersion-engineered silicon germanium waveguide,” *Opt. Lett.* **40**(17), 4118–4121 (2015).
19. M. Sinobad, C. Monat, B. Luther-davies, *et al.*, “Mid-infrared octave spanning supercontinuum generation to 8.5 μm in silicon-germanium waveguides,” *Optica* **5**(4), 360–366 (2018).
20. M. Montesinos-Ballester, C. Lafforgue, J. Frigerio, *et al.*, “On-Chip Mid-Infrared Supercontinuum Generation from 3 to 13 μm Wavelength,” *ACS Photonics* **7**(12), 3423–3429 (2020).
21. C. Langrock, M. M. Fejer, I. Hartl, *et al.*, “Generation of octave-spanning spectra inside reverse-proton-exchanged periodically poled lithium niobate waveguides,” *Opt. Lett.* **32**(17), 2478–2480 (2007).
22. C. R. Phillips, C. Langrock, J. S. Pelc, *et al.*, “Supercontinuum generation in quasi-phase-matched LiNbO₃ waveguide pumped by a Tm-doped fiber laser system,” *Opt. Lett.* **36**(19), 3912–3914 (2011).
23. K. Iwakuni, S. Okubo, O. Tadanaga, *et al.*, “Generation of a frequency comb spanning more than 3.6 octaves from ultraviolet to mid infrared,” *Opt. Lett.* **41**(17), 3980–3983 (2016).
24. D. D. Hickstein, H. Jung, D. R. Carlson, *et al.*, “Ultrabroadband Supercontinuum Generation and Frequency-Comb Stabilization Using On-Chip Waveguides with Both Cubic and Quadratic Nonlinearities,” *Phys. Rev. Appl.* **8**(1), 014025 (2017).
25. Y. Okawachi, M. Yu, J. Cardenas, *et al.*, “Carrier envelope offset detection via simultaneous supercontinuum and second-harmonic generation in a silicon nitride waveguide,” *Opt. Lett.* **43**(19), 4627–4630 (2018).
26. M. Yu, B. Desiatov, Y. Okawachi, *et al.*, “Coherent two-octave-spanning supercontinuum generation in lithium-niobate waveguides,” *Opt. Lett.* **44**(5), 1222–1225 (2019).
27. M. Jankowski, C. Langrock, B. Desiatov, *et al.*, “Ultrabroadband nonlinear optics in nanophotonic periodically poled lithium niobate waveguides,” *Optica* **7**(1), 40 (2020).
28. Y. Okawachi, M. Yu, B. Desiatov, *et al.*, “Chip-based self-referencing using integrated lithium niobate waveguides,” *Optica* **7**(6), 702–707 (2020).
29. J. Mishra, T. P. McKenna, E. Ng, *et al.*, “Mid-infrared nonlinear optics in thin-film lithium niobate on sapphire,” *Optica* **8**(6), 921–924 (2021).
30. J. Mishra, M. Jankowski, A. Y. Hwang, *et al.*, “Ultra-broadband mid-infrared generation in dispersion-engineered thin-film lithium niobate,” *Opt. Express* **30**(18), 32752 (2022).
31. A. Y. Hwang, H. S. Stokowski, T. Park, *et al.*, “Mid-infrared spectroscopy with a broadly tunable thin-film lithium niobate optical parametric oscillator,” *Optica* **10**(11), 1535–1542 (2023).
32. M. Jankowski, C. Langrock, B. Desiatov, *et al.*, “Supercontinuum generation by saturated second-order nonlinear interactions,” *APL Photonics* **8**(11), 116104 (2023).
33. M. Jankowski, A. Marandi, C. R. Phillips, *et al.*, “Temporal Simultons in Optical Parametric Oscillators,” *Phys. Rev. Lett.* **120**(5), 053904 (2018).
34. M. Jankowski, J. Mishra, and M. M. Fejer, “Dispersion-engineered $\chi(2)$ nanophotonics: a flexible tool for nonclassical light,” *JPhys Photonics* **3**(4), 042005 (2021).
35. J. Rutledge, A. Catanese, D. D. Hickstein, *et al.*, “Broadband ultraviolet-visible frequency combs from cascaded high-harmonic generation in quasi-phase-matched waveguides,” *J. Opt. Soc. Am. B* **38**(8), 2252–2260 (2021).
36. C. Phillips, M. Jankowski, N. Flemens, *et al.*, “General framework for ultrafast nonlinear photonics: unifying single and multi-envelope treatments,” *Opt. Express* (2024) (to be published).
37. M. Hamrouni, M. Jankowski, A. Y. Hwang, *et al.*, Data for “Picojoule-level supercontinuum generation in thin-film lithium niobate on sapphire,” EUDAT B2SHARE repository (2024), <https://b2share.eudat.eu/records/0504eba6664e40a09ab745a768cc0f2b>.

3.4 Chapter conclusion

In this chapter we have revisited different techniques for nonlinear frequency conversion. The three studies focus on achieving broadband frequency conversion with reduced power requirements. In the first section, we present a novel approach to terahertz generation based on optical rectification. By driving the GaP nonlinear crystal directly inside the cavity of an ultrafast Yb-based bulk laser oscillator, we demonstrate similar performance as conventional approaches, yet with a much simpler, cheaper, and smaller driving source. The success of the approach largely relies on the development of the Yb-based driving source, which besides achieving state-of-the-art peak power levels, requires high efficiencies to support the nonlinear losses.

In section 3.2 and 3.3, we utilize dispersion-engineered TFLN nanophotonic waveguides to achieve picojoule-level broadband frequency conversion. In a first work we drive OPA with commercially available sources to generate broadband MIR light in the 3-4 μm band. In the second study, we demonstrate ultraviolet-to-mid-infrared SCG and use the generated spectrum to detect the f_{CEO} of the pump directly at the output of the waveguide. Finally, the three articles presented in this chapter may open new paths for nonlinear frequency conversion at high repetition rates, which has always been a challenge in the field.

References

- [1] S. Vasilyev, I. Moskalev, V. Smolski, J. Peppers, M. Mirov, Y. Barnakov, V. Fedorov, D. Martyshkin, S. Mirov, and V. Gapontsev, “Kerr-lens mode-locked Cr: ZnS oscillator reaches the spectral span of an optical octave”, *Optics Express* **29**, 2458 (2021).
- [2] D. Burghoff, T.-Y. Kao, N. Han, C. W. I. Chan, X. Cai, Y. Yang, D. J. Hayton, J.-R. Gao, J. L. Reno, and Q. Hu, “Terahertz laser frequency combs”, *Nature Photonics* **8**, 462 (2014).
- [3] M. Rösch, M. Beck, M. J. Süess, D. Bachmann, K. Unterrainer, J. Faist, and G. Scalari, “Heterogeneous terahertz quantum cascade lasers exceeding 1.9 THz spectral bandwidth and featuring dual comb operation”, *Nanophotonics* **7**, 237 (2018).
- [4] K. Fujita, S. Jung, Y. Jiang, J. H. Kim, A. Nakanishi, A. Ito, M. Hitaka, T. Edamura, and M. A. Belkin, “Recent progress in terahertz difference-frequency quantum cascade laser sources”, *Nanophotonics* **7**, 1795 (2018).

- [5] K. Yang, P. Richards, and Y. Shen, “Generation of far-infrared radiation by picosecond light pulses in LiNbO₃”, *Applied Physics Letters* **19**, 320 (1971).
- [6] A. Bonvalet, M. Joffre, J. Martin, and A. Migus, “Generation of ultra-broadband femtosecond pulses in the mid-infrared by optical rectification of 15 fs light pulses at 100 MHz repetition rate”, *Applied Physics Letters* **67**, 2907 (1995).
- [7] F. Zernike Jr and P. R. Berman, “Generation of far infrared as a difference frequency”, *Physical Review Letters* **15**, 999 (1965).
- [8] W. Shi, Y. J. Ding, N. Fernelius, and K. Vodopyanov, “Efficient, tunable, and coherent 0.18–5.27-THz source based on GaSe crystal”, *Optics letters* **27**, 1454 (2002).
- [9] D. Cook and R. Hochstrasser, “Intense terahertz pulses by four-wave rectification in air”, *Optics letters* **25**, 1210 (2000).
- [10] J. Buldt, M. Mueller, H. Stark, C. Jauregui, and J. Limpert, “Fiber laser-driven gas plasma-based generation of THz radiation with 50-mW average power”, *Applied Physics B* **126**, 1 (2020).
- [11] J. Buldt, H. Stark, M. Müller, C. Grebing, C. Jauregui, and J. Limpert, “Gas-plasma-based generation of broadband terahertz radiation with 640 mW average power”, *Optics Letters* **46**, 5256 (2021).
- [12] F. Blanchard, L. Razzari, H.-C. Bandulet, G. Sharma, R. Morandotti, J.-C. Kieffer, T. Ozaki, M. Reid, H. Tiedje, H. Haugen, et al., “Generation of 1.5 μ J single-cycle terahertz pulses by optical rectification from a large aperture ZnTe crystal”, *Optics Express* **15**, 13212 (2007).
- [13] P. Weightman, “Prospects for the study of biological systems with high power sources of terahertz radiation”, *Physical biology* **9**, 053001 (2012).
- [14] C. Yu, S. Fan, Y. Sun, and E. Pickwell-MacPherson, “The potential of terahertz imaging for cancer diagnosis: A review of investigations to date”, *Quantitative imaging in medicine and surgery* **2**, 33 (2012).
- [15] J. Drs, J. Fischer, N. Modsching, F. Labaye, M. Müller, V. J. Wittwer, and T. Südmeyer, “A Decade of Sub-100-fs Thin-Disk Laser Oscillators”, *Laser & Photonics Reviews* **17**, 2200258 (2023).
- [16] C. J. Saraceno, “Mode-locked thin-disk lasers and their potential application for high-power terahertz generation”, *Journal of Optics* **20**, 044010 (2018).

- [17] J. Fischer, J. Drs, N. Modsching, F. Labaye, V. J. Wittwer, and T. Südmeyer, “Efficient 100-MW, 100-W, 50-fs-class Yb: YAG thin-disk laser oscillator”, *Optics Express* **29**, 42075 (2021).
- [18] F. Meyer, N. Hekmat, T. Vogel, A. Omar, S. Mansourzadeh, F. Fobbe, M. Hoffmann, Y. Wang, and C. Saraceno, “Milliwatt-class broadband THz source driven by a 112 W, sub-100 fs thin-disk laser”, *Optics Express* **27**, 30340 (2019).
- [19] F. Meyer, T. Vogel, S. Ahmed, and C. J. Saraceno, “Single-cycle, MHz repetition rate THz source with 66 mW of average power”, *Optics letters* **45**, 2494 (2020).
- [20] N. T. Yardimci, S.-H. Yang, C. W. Berry, and M. Jarrahi, “High-power terahertz generation using large-area plasmonic photoconductive emitters”, *IEEE Transactions on Terahertz Science and Technology* **5**, 223 (2015).
- [21] N. T. Yardimci, S. Cakmakyapan, S. Hemmati, and M. Jarrahi, “A high-power broadband terahertz source enabled by three-dimensional light confinement in a plasmonic nanocavity”, *Scientific reports* **7**, 4166 (2017).
- [22] T. O. Buchmann, E. J. Railton Kelleher, M. Jazbinsek, B. Zhou, J.-H. Seok, O.-P. Kwon, F. Rotermund, and P. U. Jepsen, “High-power few-cycle THz generation at MHz repetition rates in an organic crystal”, *APL Photonics* **5** (2020).
- [23] C. Vicario, M. Jazbinsek, A. Ovchinnikov, O. Chefonov, S. Ashitkov, M. Agranat, and C. Hauri, “High efficiency THz generation in DSTMS, DAST and OH1 pumped by Cr: forsterite laser”, *Optics express* **23**, 4573 (2015).
- [24] J. Drs, N. Modsching, C. Paradis, C. Kränkel, V. J. Wittwer, O. Razskazovskaya, and T. Südmeyer, “Optical rectification of ultrafast Yb lasers: pushing power and bandwidth of terahertz generation in GaP”, *JOSA B* **36**, 3039 (2019).
- [25] M. Theuer, D. Molter, K. Maki, C. Otani, J. L’huillier, and R. Beigang, “Terahertz generation in an actively controlled femtosecond enhancement cavity”, *Applied Physics Letters* **93** (2008).
- [26] J. Darmo, T. Müller, G. Strasser, K. Unterrainer, T. Le, A. Stingl, and G. Tempea, “Voltage-controlled intracavity terahertz generator for self-starting Ti: sapphire lasers”, *Optics letters* **27**, 1941 (2002).
- [27] G. Matthäus, B. Ortaç, J. Limpert, S. Nolte, R. Hohmuth, M. Voitsch, W. Richter, B. Pradarutti, and A. Tünnermann, “Intracavity terahertz generation inside a high-energy ultrafast soliton fiber laser”, *Applied Physics Letters* **93** (2008).

- [28] S. Xu, J. Liu, G. Zheng, and J. Li, “Broadband terahertz generation through intracavity nonlinear optical rectification”, *Optics Express* **18**, 22625 (2010).
- [29] Y. Wang, T. Vogel, M. Khalili, S. Mansourzadeh, K. Hasse, S. Sunstov, D. Kip, and C. J. Saraceno, “High-power intracavity single-cycle THz pulse generation using thin lithium niobate”, *Optica* **10**, 1719 (2023).
- [30] T. Schibli, E. Thoen, F. Kärtner, and E. Ippen, “Suppression of Q-switched mode locking and break-up into multiple pulses by inverse saturable absorption”, *Applied Physics B* **70**, S41 (2000).
- [31] R. Grange, M. Haiml, R. Paschotta, G. Spühler, L. Krainer, M. Golling, O. Ostinelli, and U. Keller, “New regime of inverse saturable absorption for self-stabilizing passively mode-locked lasers”, *Applied Physics B* **80**, 151 (2005).
- [32] D. Zhu, L. Shao, M. Yu, R. Cheng, B. Desiatov, C. Xin, Y. Hu, J. Holzgrafe, S. Ghosh, A. Shams-Ansari, et al., “Integrated photonics on thin-film lithium niobate”, *Advances in Optics and Photonics* **13**, 242 (2021).
- [33] A. Boes, L. Chang, C. Langrock, M. Yu, M. Zhang, Q. Lin, M. Lončar, M. Fejer, J. Bowers, and A. Mitchell, “Lithium niobate photonics: Unlocking the electromagnetic spectrum”, *Science* **379**, eabj4396 (2023).
- [34] J. Mishra, T. P. McKenna, E. Ng, H. S. Stokowski, M. Jankowski, C. Langrock, D. Heydari, H. Mabuchi, M. Fejer, and A. H. Safavi-Naeini, “Mid-infrared nonlinear optics in thin-film lithium niobate on sapphire”, *Optica* **8**, 921 (2021).
- [35] J. Mishra, M. Jankowski, A. Y. Hwang, H. S. Stokowski, T. P. McKenna, C. Langrock, E. Ng, D. Heydari, H. Mabuchi, A. H. Safavi-Naeini, et al., “Ultra-broadband mid-infrared generation in dispersion-engineered thin-film lithium niobate”, *Optics Express* **30**, 32752 (2022).
- [36] A. Y. Hwang, H. S. Stokowski, T. Park, M. Jankowski, T. P. McKenna, C. Langrock, J. Mishra, V. Ansari, M. M. Fejer, and A. H. Safavi-Naeini, “Mid-infrared spectroscopy with a broadly tunable thin-film lithium niobate optical parametric oscillator”, *Optica* **10**, 1535 (2023).
- [37] C. Manzoni and G. Cerullo, “Design criteria for ultrafast optical parametric amplifiers”, *Journal of Optics* **18**, 103501 (2016).
- [38] B. Luther-Davies and Y. Yu, “Efficient generation of ultra-short pulses in the infrared from a simple PPLN optical parametric amplifier”, in *Nonlinear Optics* (Optica Publishing Group, 2017), NTu2A–4.

- [39] A. Sukhorukov and A. Shchednova, “Parametric amplification of light in the field of a modulated laser wave”, *Journal of Experimental and Theoretical Physics* **60**, 1251 (1971).
- [40] R. Danielius, A. Piskarskas, A. Stabinis, G. Banfi, P. Di Trapani, and R. Righini, “Traveling-wave parametric generation of widely tunable, highly coherent femtosecond light pulses”, *JOSA B* **10**, 2222 (1993).
- [41] S. Marchese, E. Innerhofer, R. Paschotta, S. Kurimura, K. Kitamura, G. Arisholm, and U. Keller, “Room temperature femtosecond optical parametric generation in MgO-doped stoichiometric LiTaO₃”, *Applied Physics B* **81**, 1049 (2005).
- [42] M. Charbonneau-Lefort, B. Afeyan, and M. Fejer, “Theory and simulation of gain-guided noncollinear modes in chirped quasi-phase-matched optical parametric amplifiers”, *JOSA B* **27**, 824 (2010).
- [43] A. Gorbach, M. Roiz, M. Vainio, and D. Skryabin, “Trapping of ultrashort pulses in nondegenerate parametric conversion”, *Physical Review A* **107**, 063515 (2023).
- [44] J. M. Dudley, G. Genty, and S. Coen, “Supercontinuum generation in photonic crystal fiber”, *Reviews of modern physics* **78**, 1135 (2006).
- [45] C. Langrock, M. Fejer, I. Hartl, and M. E. Fermann, “Generation of octave-spanning spectra inside reverse-proton-exchanged periodically poled lithium niobate waveguides”, *Optics letters* **32**, 2478 (2007).
- [46] C. Phillips, C. Langrock, J. Pelc, M. Fejer, J. Jiang, M. E. Fermann, and I. Hartl, “Supercontinuum generation in quasi-phase-matched LiNbO₃ waveguide pumped by a Tm-doped fiber laser system”, *Optics letters* **36**, 3912 (2011).
- [47] K. Iwakuni, S. Okubo, O. Tadanaga, H. Inaba, A. Onae, F.-L. Hong, and H. Sasada, “Generation of a frequency comb spanning more than 3.6 octaves from ultraviolet to mid infrared”, *Optics Letters* **41**, 3980 (2016).
- [48] D. D. Hickstein, H. Jung, D. R. Carlson, A. Lind, I. Coddington, K. Srinivasan, G. G. Ycas, D. C. Cole, A. Kowligy, C. Fredrick, et al., “Ultra-broadband supercontinuum generation and frequency-comb stabilization using on-chip waveguides with both cubic and quadratic nonlinearities”, *Physical Review Applied* **8**, 014025 (2017).
- [49] Y. Okawachi, M. Yu, J. Cardenas, X. Ji, A. Klenner, M. Lipson, and A. L. Gaeta, “Carrier envelope offset detection via simultaneous supercontinuum and second-harmonic generation in a silicon nitride waveguide”, *Optics letters* **43**, 4627 (2018).

- [50] M. Yu, B. Desiatov, Y. Okawachi, A. L. Gaeta, and M. Lončar, “Coherent two-octave-spanning supercontinuum generation in lithium-niobate waveguides”, *Optics letters* **44**, 1222 (2019).
- [51] M. Jankowski, N. Jornod, C. Langrock, B. Desiatov, A. Marandi, M. Lončar, and M. M. Fejer, “Quasi-static optical parametric amplification”, *Optica* **9**, 273 (2022).
- [52] M. Jankowski, C. Langrock, B. Desiatov, A. Marandi, C. Wang, M. Zhang, C. R. Phillips, M. Lončar, and M. Fejer, “Ultrabroadband nonlinear optics in nanophotonic periodically poled lithium niobate waveguides”, *Optica* **7**, 40 (2020).
- [53] Y. Okawachi, M. Yu, B. Desiatov, B. Y. Kim, T. Hansson, M. Lončar, and A. L. Gaeta, “Chip-based self-referencing using integrated lithium niobate waveguides”, *Optica* **7**, 702 (2020).
- [54] M. Jankowski and M. M. Fejer, “Supercontinuum Generation by Saturated Second-Order Nonlinear Interactions: Scaling Laws and Design Principles”, in *Nonlinear Optics* (Optica Publishing Group, 2023), Th3A–3.
- [55] M. Jankowski, J. Mishra, and M. Fejer, “Dispersion-engineered nanophotonics: a flexible tool for nonclassical light”, *Journal of Physics: Photonics* **3**, 042005 (2021).
- [56] C. Hu, A. Pan, T. Li, X. Wang, Y. Liu, S. Tao, C. Zeng, and J. Xia, “High-efficient coupler for thin-film lithium niobate waveguide devices”, *Optics Express* **29**, 5397 (2021).

Chapter 4

Conclusion

4.1 Summary of this dissertation

The two main topics addressed in this dissertation are the development of ultrafast Yb-based bulk laser oscillators, and frequency conversion of femtosecond pulses. We started with the development of a Kerr-lens mode-locked Yb:CALGO laser oscillator operating at 1-GHz repetition rate. By delivering sub-50-fs pulses and several watts of average power, this source demonstrates the highest peak power reported by any GHz-class Yb-based bulk laser oscillator. In a subsequent work, we turned this source into a functional OFC by achieving its full stabilization. The resulting OFC reaches noise levels comparable to state-of-the-art sources and delivers remarkably-high power levels. The good stabilization performance were facilitated by constructing the laser inside a thick monolithic aluminum box for improving the stability and robustness of the free-running source.

In the last section of this chapter, we discussed a novel pumping concept for delivering few-cycles pulses at high optical-to-optical efficiencies with Yb-based laser oscillators. We designed and fabricated a pump mirror with different properties depending on the polarization of the light. More specifically, the mirrors were designed to be highly transmissive at the pump wavelength for a p-polarized beam, and highly reflective and broadband at laser wavelengths for an s-polarized beam. These mirrors enable us to use a collinear pumping scheme while circumventing the limitations imposed by the low quantum defect of Yb:CALGO. This way, we achieved the highest average power and optical-to-optical efficiency compared to any previously reported Yb-based oscillator operating below 40 fs. These achievements not only extend the performance

boundaries of Yb-class lasers but also highlight their potential as powerful, cost-efficient and compact alternatives to traditional Ti:sapphire sources, essential for applications beyond laboratory settings.

In the second chapter, we explored new avenues for efficient and broadband frequency conversion. In a first work, we discuss the development of a simple and cost-efficient terahertz source delivering hundreds of microwatts of average power and several terahertz of spectral bandwidth. This source relies on driving optical rectification directly inside an Yb:CALGO KLM laser oscillator, offering megawatt peak power levels for frequency converting the near-infrared femtosecond pulses into the terahertz domain. This approach demonstrates performance comparable to state-of-the-art terahertz sources based on expensive thin-disk laser oscillators [1, 2].

The results shown in the remaining sections build on recent progress in TFLN technologies and have been obtained in close collaboration with the groups of Martin Fejer and Amir Safavi-Naeini. By exploiting the high nonlinearities and dispersion engineering offered by the TFLN platform, we revisited nonlinear processes to demonstrate efficient and broadband frequency conversion at much lower power requirements compared to traditional approaches. Also, these works explore the potential of TFLN-on-sapphire that stands as a promising alternative to the commonly used TFLN platform based on silica cladding, which suffers from substantial losses in the MIR. In the first work, we utilized dispersion-engineered TFLN nanowaveguides for broadband MIR generation via gain-trapped parametric down conversion. There, we first studied the formation of gain-trapped solitons arising from an interplay between the nonlinear gain and group velocities of the pulses. We were able to show strong agreement between the numerical and experimental results. This regime of OPA enabled up to 50% NIR-to-MIR conversion efficiency using a few picojoules of in-coupled pulse energies. Remarkably, using a maximum pump-pulse energy of 12 pJ, we generate hundreds of microwatts of idler within 600 nm of bandwidth extending between 2800-3300 nm. Only a few of comparable results can be found in the literature. For instance, [3, 4] report on picojoule degenerate OPA demonstrating similar power levels with ultra-broadband spectra. However, their approaches did not allow reaching the 3-4 μm band, which is limiting for many applications in spectroscopy.

In the final section, we utilized dispersion-engineered TFLN nanowaveguides to demonstrate SCG spanning from the UV to the MIR region. Our approach relies on SCG by saturated $\chi^{(2)}$ nonlinear interactions, which has been recently introduced in [4–6]. More specifically, the approach is based on GVM-matched second harmonic generation where the interplay between saturation and small phase-mismatch leads to strong spectral broadening. The supercontinuum gen-

erated by the spectrally broadened fundamental and second harmonics enables simple and direct f-to-2f detection. Also, driving the waveguides with tens of picojoules of in-coupled energy, we were able to generate harmonics up to the fifth order.

Compared to traditional nonlinear approaches based on bulk nonlinear media, the TFLN waveguides operate at picojoules, rather than nanojoules, of on-chip driving pulse energy. The radical reduction of the power requirements allowed by those nanodevices open promising paths for nonlinear conversions at high repetition rates.

4.2 Outlook

The development of the near-infrared OFC source presented in the first chapter is an important step toward the realization of functional spectroscopic devices at high repetition rate. Nevertheless, since the MIR region is much more attractive for molecular spectroscopy, it would be interesting to frequency convert the near-infrared pulses above 3 μm , 4 μm or even higher. Given the high peak power levels demonstrated by this source, frequency conversion into the 3-4 μm band would be readily possible via conventional nonlinear methods such as optical parametric amplification or difference frequency generation. Another realistic approach would be to pump the TFLN nanowaveguides presented in section 3.2 with a fraction of the available power. If we directly extrapolate the results reported in this section, using 10 pJ of in-coupled pulse energies, we could obtain 2 pJ of idler, corresponding to 2 mW of average power around 3.2 μm at 1-GHz repetition rate (provided better management of the in/out coupling efficiency). Such power levels are enough for many applications in spectroscopy, even using conventional MIR detectors. During the experiments, the waveguides were found remarkably resistant to high average pump power. Typically, we were able to launch more than 500 mW of incident uncoupled average power without causing any visible damage on the waveguide facet. Providing future improvement of the coupling efficiency, this gives rather large power scalability. A possibility to generate higher MIR average power is using shorter waveguides. Indeed, reducing the interaction length requires increasing the pump-pulse energy to reach the typical 50% pump depletion, leading to higher generated power.

Another direction is scaling the OFC repetition rate to 10-20 GHz, which would unlock new possibilities for applications in microwave generation and telecommunications. So far, only few mode-locked lasers operating in this regime have been reported [7–9]. For instance, in [8] the authors demonstrate a 10-GHz SESAM mode-locked laser oscillator achieving up to 1.44 W average power and

172 fs pulse duration in a first configuration and 0.81 W, 108 fs in a second configuration. Another example is [9], which reports on a 20-GHz KLM Yb:Y2O3 laser oscillator demonstrating >100 -fs pulses and only 20 mW of average power. Although these lasers are pioneers in this field, I believe substantial improvements can be achieved. In fact, combining the advantage of KLM and multimode pumping is promising to reach multiwatt average power levels and sub-50-fs pulses at 10 GHz repetition rate.

Another natural extension of the work presented in this chapter is the realization of broadband OFCs emitting in the 2.0 μm region, which could directly benefit from the stabilization method presented in section 3.3. Furthermore, this spectral region features several advantages for nonlinear down-conversion. Besides facilitating MIR generation deep into the LN transparency window via SCG, the nano-fabrication accuracy required for dispersion engineering is less stringent at longer wavelengths. Today, the maturity of Tm-based lasers is still low and tremendous efforts will be required to catch up the advance of Yb-based sources. However, sub-100-fs pulses at MHz levels of repetition rate have been demonstrated multiple times with KLM lasers based on Tm,Ho:CaYAlO₄, Tm:Lu₂O₃, Tm:Sc₂O₃ or Tm,Ho:CLNGG crystals [10–14]. For efficient and broadband nonlinear conversion, sub-100-fs pulse duration is a relevant starting point. However, decreasing the pulse duration toward few optical cycles would be interesting to further explore the capabilities of the TFLN devices and revisit nonlinear processes with broader bandwidths.

There is also an extraordinary amount of work to be done regarding the future designs and realizations of nanophotonic devices. For instance, current geometric dispersion-engineering has limited degrees of freedom, making the elimination of multiple dispersion orders at multiple wavelengths difficult. An intriguing solution consists in using claddings composed of multiple thin layers. While similar solution has already been proposed in TFLN [15], the benefits of the approach is still to be explored and exploited. Increasing the degrees of freedom for dispersion engineering could allow extension of quasi-static degenerate parametric amplification (discussed in [3, 4]) to three-wave interactions. Matching the group velocity of a pump, signal and idler pulse centered at three different wavelengths is a promising path for broadband generation of light across the entire LN transparency window.

Driving intra-pulse difference frequency generation is another possibility to further harnessing the LN transparency window. This technique has already been demonstrated successfully inside weakly confining waveguides [16]. There, they drive intra-pulse difference frequency generation inside PPLN waveguides to produce broadband light in the 4–5 μm band. Extending this technique to tightly confining devices should naturally decrease the power requirements, in

addition to potentially benefit from dispersion engineering.

In parallel to pushing the boundaries of MIR generation, it is also interesting to explore frequency conversion toward the ultraviolet boundary of the LN window, with important applications in atomic clocks [17]. Today, UV devices based of TFLN nanowaveguides remain rare [18–20] and necessitate to overcome several challenges. The quasi-phasematching and dispersion engineering sensitivity as well as material scattering impose stringent requirements on the fabrication process [20]. Here again, the multilayer cladding technique could be employed to find waveguides design where the dispersion is not critical with respect to the geometry.

Another important challenge to overcome is the low coupling efficiency. While fiber-to-nanowaveguide coupling efficiencies can reach 30%, typical free-space couplings are limited to only few percents. For instance, in the work discussed in sections 3.3, we reported free-space-to-waveguide coupling efficiencies around 1.5%. Besides reducing the pump power requirements, a better coupling is important to avoid facet damages and detrimental thermal effects due to the uncoupled light. A typical solution is to first couple the light from an optical fiber into a large, low-index waveguide with high efficiency. The coupled mode is subsequently adiabatically transferred to a sub-wavelength-scale TFLN waveguide mode. This approach has been proposed in [21] where they achieve up to 60% of coupling efficiency in the near-infrared, and expect up to 90% is possible. Extending this technique to the mid-infrared is another promising, yet challenging path to explore.

We note here that many of these future directions rely or benefit on the realization of the multilayer-cladding platform. Of course, successful developments and implementations will require a tremendous amount of work to overcome the different challenges, which includes the realization of top and bottom cladding coatings with low extinction coefficients. Finally, while it is not possible to predict a clear time-scale for the outlooks to be realized, I expect the work achieved in this thesis will stimulate interesting studies these upcoming years. Should I envisage the future trajectory of progress in this field, my forecast points towards the realization of fully integrated optical systems. Such a development promises not merely an evolution, but a fundamental paradigm shift in the realm of optics, undoubtedly leading to profound and direct impacts on society.

References

- [1] J. Drs, N. Modsching, C. Paradis, C. Kränkel, V. J. Wittwer, O. Razskazovskaya, and T. Südmeyer, “Optical rectification of ultrafast Yb lasers:

- pushing power and bandwidth of terahertz generation in GaP”, *JOSA B* **36**, 3039 (2019).
- [2] F. Meyer, N. Hekmat, T. Vogel, A. Omar, S. Mansourzadeh, F. Fobbe, M. Hoffmann, Y. Wang, and C. Saraceno, “Milliwatt-class broadband THz source driven by a 112 W, sub-100 fs thin-disk laser”, *Optics Express* **27**, 30340 (2019).
- [3] L. Ledezma, R. Sekine, Q. Guo, R. Nehra, S. Jahani, and A. Marandi, “Intense optical parametric amplification in dispersion-engineered nanophotonic lithium niobate waveguides”, *Optica* **9**, 303 (2022).
- [4] M. Jankowski, N. Jornod, C. Langrock, B. Desiatov, A. Marandi, M. Lončar, and M. M. Fejer, “Quasi-static optical parametric amplification”, *Optica* **9**, 273 (2022).
- [5] M. Jankowski, C. Langrock, B. Desiatov, A. Marandi, C. Wang, M. Zhang, C. R. Phillips, M. Lončar, and M. Fejer, “Ultrabroadband nonlinear optics in nanophotonic periodically poled lithium niobate waveguides”, *Optica* **7**, 40 (2020).
- [6] M. Jankowski and M. M. Fejer, “Supercontinuum Generation by Saturated Second-Order Nonlinear Interactions: Scaling Laws and Design Principles”, in *Nonlinear Optics* (Optica Publishing Group, 2023), Th3A–3.
- [7] A. Bartels, D. Heinecke, and S. A. Diddams, “10-GHz self-referenced optical frequency comb”, *Science* **326**, 681 (2009).
- [8] L. M. Krüger, A. S. Mayer, Y. Okawachi, X. Ji, A. Klenner, A. R. Johnson, C. Langrock, M. M. Fejer, M. Lipson, A. L. Gaeta, et al., “Performance scaling of a 10-GHz solid-state laser enabling self-referenced CEO frequency detection without amplification”, *Optics Express* **28**, 12755 (2020).
- [9] S. Kimura, S. Tani, and Y. Kobayashi, “Kerr-lens mode locking above a 20 GHz repetition rate”, *Optica* **6**, 532 (2019).
- [10] H. Zhao and A. Major, “Powerful 67 fs Kerr-lens mode-locked prismless Yb: KGW oscillator”, *Optics express* **21**, 31846 (2013).
- [11] Y. Wang, Y. Zhao, P. Loiko, Z. Pan, W. Chen, M. Mero, X. Xu, J. Xu, X. Mateos, A. Major, et al., “52-fs SESAM mode-locked Tm, Ho: CALGO laser”, in *Advanced Solid State Lasers* (Optica Publishing Group, 2019), AM3A–7.
- [12] Y. Zhao, Y. Wang, W. Chen, Z. Pan, L. Wang, X. Dai, H. Yuan, Y. Zhang, H. Cai, J. E. Bae, et al., “67-fs pulse generation from a mode-locked Tm, Ho: CLNGG laser at 2083 nm”, *Optics express* **27**, 1922 (2019).

- [13] A. Suzuki, C. Kränkel, and M. Tokurakawa, “Sub-6 optical-cycle Kerr-lens mode-locked Tm: Lu 2 O 3 and Tm: Sc 2 O 3 combined gain media laser at 2.1 μm ”, *Optics Express* **29**, 19465 (2021).
- [14] W. Yao, Y. Wang, S. Tomilov, M. Hoffmann, S. Ahmed, C. Liebald, D. Rytz, M. Peltz, V. Wesemann, and C. J. Saraceno, “8.7-W average power, in-band pumped femtosecond Ho: CALGO laser at 2.1 μm ”, *Optics Express* **30**, 41075 (2022).
- [15] H. Liang, Y. He, R. Luo, and Q. Lin, “Ultra-broadband dispersion engineering of nanophotonic waveguides”, *Optics express* **24**, 29444 (2016).
- [16] A. S. Kowligy, D. R. Carlson, D. D. Hickstein, H. Timmers, A. J. Lind, P. G. Schunemann, S. B. Papp, and S. A. Diddams, “Mid-infrared frequency combs at 10 GHz”, *Optics Letters* **45**, 3677 (2020).
- [17] A. D. Ludlow, M. M. Boyd, J. Ye, E. Peik, and P. O. Schmidt, “Optical atomic clocks”, *Reviews of Modern Physics* **87**, 637 (2015).
- [18] A. A. Sayem, Y. Wang, J. Lu, X. Liu, A. W. Bruch, and H. X. Tang, “Efficient and tunable blue light generation using lithium niobate nonlinear photonics”, *Applied Physics Letters* **119** (2021).
- [19] T. Park, H. S. Stokowski, V. Ansari, T. P. McKenna, A. Y. Hwang, M. Fejer, and A. H. Safavi-Naeini, “High-efficiency second harmonic generation of blue light on thin-film lithium niobate”, *Optics Letters* **47**, 2706 (2022).
- [20] E. Hwang, N. Harper, R. Sekine, L. Ledezma, A. Marandi, and S. K. Cushing, “Tunable and efficient ultraviolet generation in nanophotonic lithium niobate”, *arXiv preprint arXiv:2303.10234* (2023).
- [21] C. Hu, A. Pan, T. Li, X. Wang, Y. Liu, S. Tao, C. Zeng, and J. Xia, “High-efficient coupler for thin-film lithium niobate waveguide devices”, *Optics Express* **29**, 5397 (2021).

Acknowledgments - Remerciements

Je tiens à exprimer ma profonde gratitude à toutes les personnes qui m'ont soutenu, encouragé, motivé et guidé tout au long de mon parcours académique, dont l'aboutissement prend sa forme dans cette présente thèse. Bien qu'il me soit impossible d'énumérer chacun individuellement, je voudrais mentionner ceux qui ont joué un rôle crucial jusqu'à présent.

Dans la sphère professionnelle, je souhaite commencer par remercier Thomas de m'avoir accueilli dans son équipe, pour sa confiance et son enthousiasme. Je suis également reconnaissant envers Martin pour les six mois enrichissants passés dans son groupe, une expérience qui a grandement contribué à mon épanouissement scientifique. Merci à tous mes collègues, à commencer par François qui m'a permis de prendre un excellent départ au LTF; Norbert pour son support scientifique; Michael pour sa joie communicative et son optimisme inépuisable; Jakub pour son soutien technique ainsi que pour nos sorties sportives dont je garde de merveilleux souvenirs. Mes remerciements s'étendent à tous les autres membres du LTF, notamment Firas, Patricia, Julian, Kenichi, Alex, Nayara et Valentin pour leur précieuse assistance au travail ainsi que pour les moments agréables que nous avons partagés en dehors du cadre professionnel. Je souhaite aussi mentionner mes collègues de Stanford. Je remercie particulièrement Marc pour sa supervision et son soutien. Marc a été une source d'inspiration scientifique exceptionnelle et a largement contribué à la réussite de cette thèse. Merci à Alex pour sa disponibilité, spécifiquement pour son support technique, rapide et de grande qualité. Merci également à Jata et Carsten pour leur aide. Par ailleurs, je souhaite mentionner Johan B. qui m'a fait connaître le LTF.

Mes amis ont également été une source d'épanouissement essentielle. Plus spécifiquement, je souhaiterais citer Léa et la remercier pour sa présence, qu'elle soit proche ou lointaine. Je remercie également Alexis sur qui je peux toujours compter, et constitue un partenaire de choix pour des séjours sports et nature. Mention particulière pour Victor, un grand coéquipier tant dans la sphère privée que professionnelle. Je remercie également Adrian, Gabriel, Lucas, Paul et Sam qui m'ont permis de découvrir, en parallèle de mon doctorat, les délices de la montagne, contribuant ainsi grandement à mon bien-être durant ces quatre dernières années. Également, je souhaite saluer Gaspard, Clément, Alex et Klara qui ont rendu mon arrivée à Neuchâtel bien plus agréable. Merci à Amy dont la rencontre me laisse, de mes aventures aux États-Unis, un souvenir impérissable. Sans oublier mes amis d'enfance, de prépa et de supoptique avec une mention spécifique pour Paul et Mathieu.

Je souhaite également remercier Luana avec qui j'ai partagé de nombreux moments de joie. En plus de participer activement à mon épanouissement quo-

tidien, Luana m'apporte une ouverture d'esprit sous bien des aspects. Pour terminer, je remercie ma famille, particulièrement mes parents et mon frère. Leur soutien indéfectible, notamment dans les moments cruciaux, a été fondamental pour la réussite de mon doctorat, et plus largement de mon parcours académique.

- Rue des Brévards 9,
2000 Neuchâtel,
Switzerland
- Tel: +33 6 77 56 69 72
E-mail: marin.hamrouni@gmail.com

Marin Hamrouni



Professional Experiences

- 11/2019 - 11/2023**
Switzerland
United-States
(4 years)
 - University of Stanford**
Research - Nonlinear nanophotonic
 Simulation, conception and characterization of nanophotonic devices:
 - Numerical simulations in linear and non-linear optics
 - Design and characterization of nanophotonic waveguides
 - University of Neuchâtel**
Research - Laser development
 Development of ultrafast optical sources and their applications:
 - Advanced simulations of laser cavity design
 - Construction and characterization of high-power femtosecond laser oscillators
 - Frequency comb stabilization and terahertz generation
- 03/2019 - 09/2019:**
Singapore
(6 months)
 - Lemnis Technologies**
R&D Computational Optics Intern
 Development of an optimized optical ray-tracing simulation software
 - Initial conception and test of algorithms in Matlab
 - Final implementation and optimization in C++/CUDA
- 06/2018 - 09/2018:**
France
(3 months)
 - Commissariat à L'Energie Atomique (CEA)**
R&D Engineer Intern
 Development of a multi-wavelength photonic Doppler velocimeter
 - Fiber-based system implementation
 - Numerical simulations in Python

Education

- 2019 - 2024:**
(4 years)
 - Time and Frequency Laboratory - Université de Neuchâtel**
PhD in physics
- 2016 - 2019:**
(3 years)
 - Institut d'Optique Graduate School - Université Paris Saclay**
Master of Engineering (specialization in Photonics)
- 2014 - 2016:**
(2 years)
 - Preparatory Classes - Pierre de Fermat**
Preparation for national competitive entrance exam to Engineering School

Aptitudes

Languages		Soft skills	
French	Native	Personal	Learning agility, adaptability, communication, sense of initiative.
English	Proficient (C1)	Experimental	Free-space and fiber optics, high-power optics, electronics.
Spanish	Basic (B1)	Management	Long-term project development, planning and grant writing. Project coordination between collaborating research groups.
Softwares		Interests	Sports (soccer and running), outdoor activities (alpinism), cooking, cinema.
Python	Illustrator		
Matlab	MS-office		
C++	LaTeX		

Déclaration sur l'honneur*

Par la présente, j'affirme avoir pris connaissance des documents d'information et de prévention du plagiat émis par l'Université de Neuchâtel et m'être renseigné-e correctement sur les techniques de citation.

J'atteste par ailleurs que le travail rendu est le fruit de ma réflexion personnelle et a été rédigé de manière autonome.

Je certifie que toute formulation, idée, recherche, raisonnement, analyse ou autre création empruntée à un tiers est correctement et consciencieusement mentionnée comme telle, de manière claire et transparente, de sorte que la source en soit immédiatement reconnaissable, dans le respect des droits d'auteur et des techniques de citations.

Je suis conscient-e que le fait de ne pas citer une source ou de ne pas la citer clairement, correctement et complètement est constitutif de plagiat.

Je prends note que le plagiat est considéré comme une faute grave au sein de l'Université. J'ai pris connaissance des risques de sanctions administratives et disciplinaires encourues en cas de plagiat (pouvant aller jusqu'au renvoi de l'université).

Je suis informé-e qu'en cas de plagiat, le dossier sera automatiquement transmis au rectorat.

Au vu de ce qui précède, **je déclare sur l'honneur ne pas avoir eu recours au plagiat ou à toute autre forme de fraude.**

Nom : Hamrouni

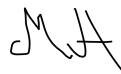
Prénom : Marin

Cursus : Doctorat en Physique

Faculté d'inscription : Faculté des sciences

Lieu et date : Neuchâtel, Mars 2024

Signature :



Ce formulaire doit être dûment rempli par tout étudiant ou toute étudiante rédigeant un travail substantiel (notamment un mémoire de bachelor ou de master) ou une thèse de doctorat. Il doit accompagner chaque travail remis au professeur ou à la professeure.

* Formulaire largement inspiré de la Directive de la direction 0.3 bis, intitulée Formulaire Code de déontologie en matière d'emprunts, de citations et d'exploitation de sources diverses, de l'Université de Lausanne, du 23 avril 2007 et adapté aux besoins de l'Université de Neuchâtel.

Rectorat. Fbg de l'Hôpital 41, 2000 Neuchâtel, tél. +41 32 718 10 20, messagerie.rectorat@unine.ch